国際化推進共同研究概要

No. 1

タイトル: Numerical calculations for the PDP using PdCu membrane

研究代表者: SHARMA, SANJEEV, KUMAR

所内世話人: 図子 秀樹

実施期間: 2016 年 月 日～ 月 日

研究概要:

プラズマ対向壁への水素イオン、水素原子の堆積束の実測のために水素透過束の研究を行ってきた。パラジウム・銅合金の水素透過曲線の解析では、物性値が乏しいために、Pd の拡散係数を用いて、表面及び裏面再結合係数を算出する計算コードを開発し、透過曲線を良く再現できる事を確認した。さらにこれを用いてプラズマ中の入射束の時間発展を解析した。結果は査読付き雑誌、1 編の共著論文者論文、また3編の共著論文は投稿中である。共著者として、2件の国際会議で口頭・ポスター発表に貢献した。

Numerical calculations for the PDP using PdCu membrane

S.K. Sharma

In order to investigate the retention flux consisting of both ions and neutrals the probe must be set near the PFCs. Under this situation surface contamination will limit the stable operation of the probe. The surface covering stainless steel mesh with transparency of 45-50 % is set in front of the membrane and steady high temperature (300 °C) operation of the membrane is maintained during the week experiment. In the present experiments $Pd_{60}Cu_{40}$ (weight %) alloy membrane is used.

1) Permeation probe system

Membrane material choice is dictated by the diffusion properties $\left(L\sqrt{\bar{k}\Gamma_{inc}}/D\right)$ of the material with the thickness of L, averaged recombination $\bar{k}$ and diffusivity D. It is crucial for the PDP probe to have the faster response time ($\propto L^2/D$) and to decrease the minimum detectable permeation flux Γ_{pdp}. Highest known diffusivity at the low temperatures of any metal-hydrogen systems has the β phase of the $Pd_{60}Cu_{40}$ alloy, and the β phase is stable in the wide temperature region (<450°C). A schematic view of a probe system is shown in Fig. 1. Cylindrical PdCu membrane (32 ϕ × 82 mm, L = 20 μ; red), is supported by a stainless steel mesh (dotted line) from both sides. The detection area A_{pdp} is ~ $7.5\times10^{-3} m^2$.Transparency of the SS mesh whose hole is 1.5 mm ϕ is 49%. A built-in cylindrical heater with a thermocouple (TC) is used to keep the membrane temperature T_{pdp} at 300 °C with a feedback controlled power supply. All probes have its own pumping system and QMA, and one common H_2 standard leak (H_2-STD). The pumping system consists of a turbo-molecular pump (TMP), rough pump and gauges. The base pressure is ~ $1 - 3 \times10^{-5}$ *Pa*. Γ_{pdp} is registered at every 0.3 s with the QMA which is absolutely calibrated with the H_2-STD. With a help of numerical calculation the net retention flux Γ_{inc} can be derived, as described in the following section.

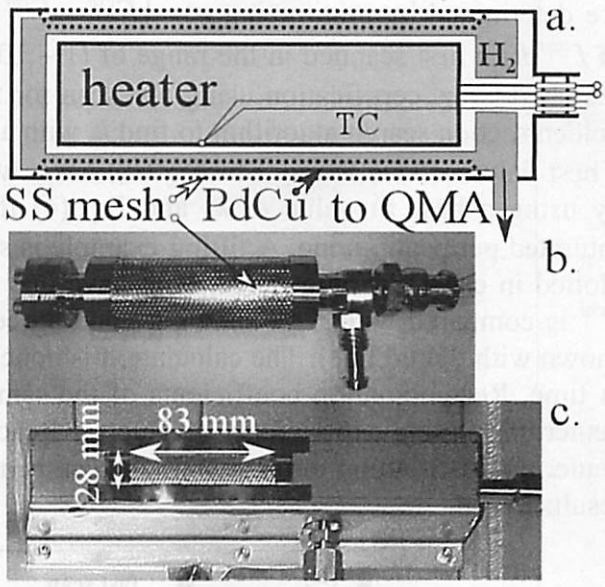

Fig.2. a. PDP probe scheme: TC - thermocouple, SS mesh supports PdCu cylinder membrane. b. Photo of the probe. c. photo of the PDP6, installed in QUEST (rotated by 90°) with the protection box.

2. Numerical calculation of Γ_{inc}

The permeation of H in the membrane can be described by the diffusion equation. Under the following nonlinear boundary and initial conditions Γ_{pdp}, measured with PDP probes, and Γ_{inc}, required in gas balance, are coupled, as described by the following equations:

$$\Gamma_{inc} = k_u c^2(0,t) - D[\partial c(x,t)/\partial x]_{x=0} , \qquad (1)$$

$$0 = k_d c^2(L,t) - D[\partial c(x,t)/\partial x]_{x=L} , \qquad (2)$$

$$\Gamma_{pdp} = k_d c^2(L,t) \qquad (3)$$

In the x - coordinate, $x = 0$ corresponds to the upstream surface, and $x = L$ to the downstream. $c(x, t)$ is the H concentration in the membrane as functions of x and t. A numerical diffusion code was used to decide Γ_{inc}. In case of PdCu the permeation process is in the surface limited regime (SLR). For steady state permeation in the SLR we can write the relation between Γ_{inc} and saturated permeated flux Γ^{sat}:

$$\Gamma_{inc} = \frac{k_d}{k_u + k_d}\Gamma^{sat}. \qquad (4)$$

A flat profile of $c(x)$ is assumed, because of the fast diffusion and weak D-dependence of permeation. We used a literature value of D : $D = (2.9 \pm 0.2) \times 10^{-9} m^2 s^{-1}$. Parameters k_u and k_d, and an incident flux amplitude k_s ($\Gamma_{inc} = k_s \Gamma^{guess}$) are scanned and the best fit values are determined by minimizing $\chi^2 = \left(\Gamma^{exp} - \Gamma^{cal}\right)^2 / \left(\Gamma^{exp}\right)^2$. For fitting an experimental curve of Γ^{exp} k_d is first scanned in the range of $(1 - 100) \times 10^{-34}$ $m^4 s^{-1}$ and for each value of k_d, k_s is searched by χ^2 certification using fast scan for finding approximate minimum position and a golden section search algorithm to find k_s with a given precision. Then using selected k_d and k_s a best value of k_u is found. Since $\chi^2(k_d)$ has a wide minimum region, k_d is iteratively decided by using a best fit value of k_u and Eq. (4) if the permeation curve shows a steady-state saturated permeation one. A fitting example is shown in Fig.2.a. and b. χ^2 (k_s) and χ^2 (k_u) are plotted in each scanning range, both have one global minimum. In Fig.2.c calculated curve Γ^{cal} is compared with Γ^{exp}, showing good agreement on the whole time scale (residuals are shown with dotted line). The calculation is done with an assumption that k_d and k_u are constant in time. Recombination coefficients of the same PdCu alloy are also determined in the RF deuterium plasma experiments by Nuclear Reaction Analysis (NRA), with which the precise deuterium distribution in the membrane can be measured. They are consistent with our fitting results [1,2].

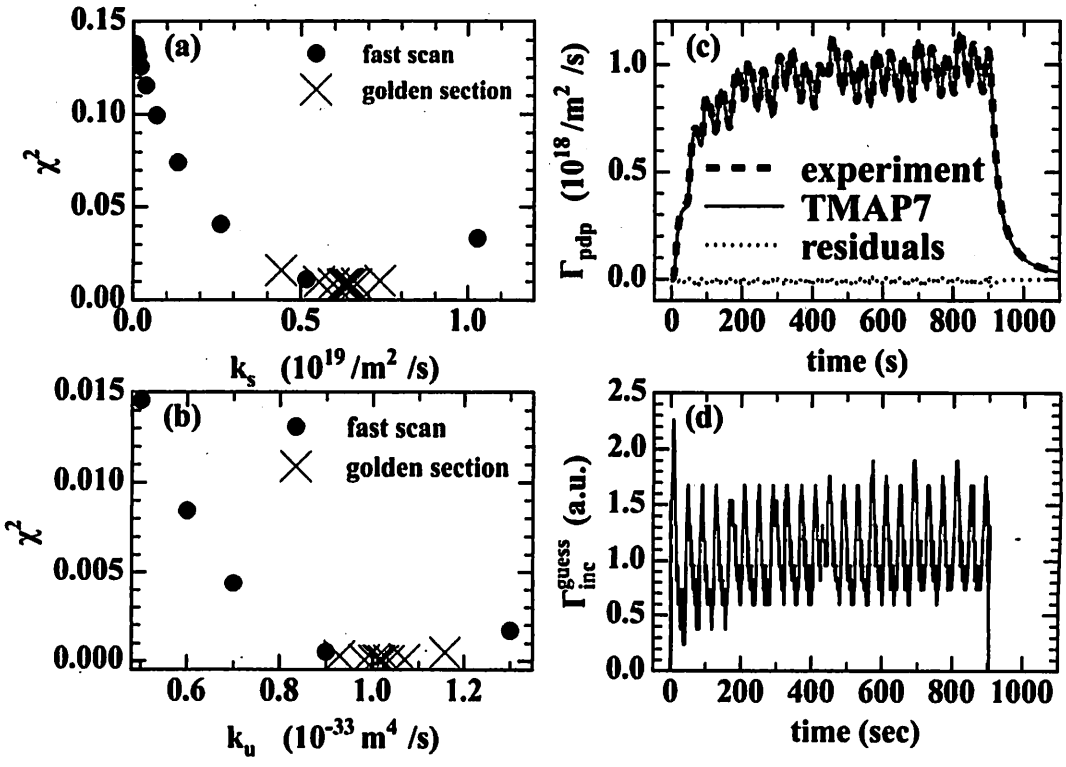

Fig.2. Fitting procedure. (a),(b) Selecting k_s and k_d by the minimum value of χ^2. Circles – fast scan for the minimum, crosses – golden section search of the precise minimum location. (c)

国際化推進共同研究概要

No. 2

タ イ ト ル: Measurement of plasma flow and edge turbulence and their effect on plasma equilibrium in QUEST
〔クエストにおけるプラズマ流れ及び周辺乱流の観測〕

研究代表者: BANERJEE, SANTANU

所内世話人: 図子 秀樹

実 施 期 間: 2016 年 1 月 16 日 ～ 1 月 31 日

研究概要:
スクレープオフ層における周辺乱流とプラズマの流れについて異なるプラズマ配位やコンパクトトーラスプラズマの入射直後のプラズマにおいて、高速カメラおよび SOL ラングミュアー探針を用いて研究を行った。結果は査読付き雑誌 1 編の第 1 著者論文、2 編の共著論文で公表し、1 件の国際会議で口頭発表した。

Measurement of plasma flow and edge turbulence in QUEST

Santanu Banerjee

Edge turbulence and plasma flow at the SOL are measured in different plasma configurations and with compact toroid (CT) injection in QUEST. We used the fast visible imaging system and SOL probe for this study. The diagnostic system and the experimental findings are discussed in brief in the following sub-sections.

Fast visible imaging system on QUEST

The fast visible imaging system is now equipped with a new fiber bundle. Also, the fixtures and front end lens holder assemblies are modified. This give more maneuverability to the optics and it is now easier setting it up. Fig. 1(a) shows the back end of the fiber bundle connected to the fast camera though the image intensifier. Also, the front end can be seen in Fig. 1(b). The front end unit enables us to rotate the fiber view in alt-azimuth directions.

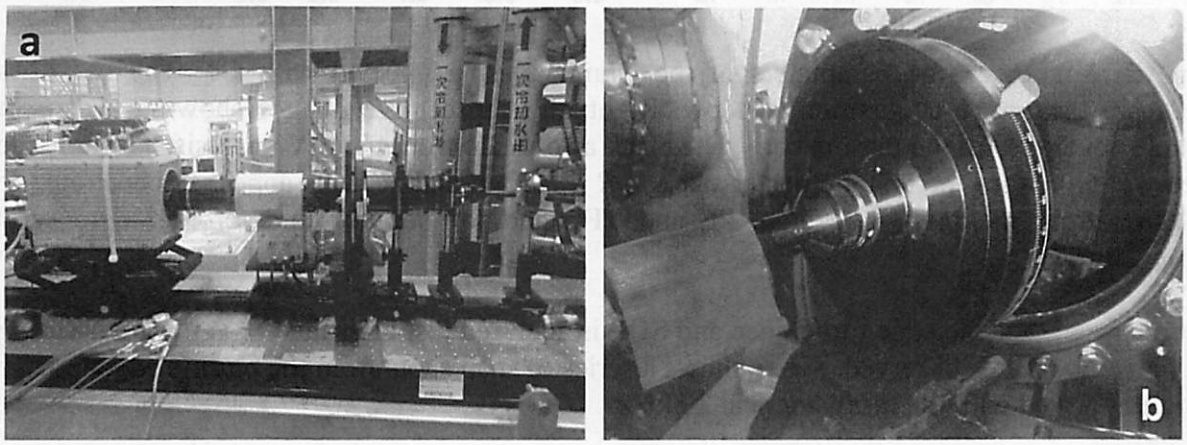

Fig. 1: (a)-(b), Back and front end of the fiber bundle on the fast visible imaging system.

Edge turbulence and SOL flow following the CT injection in QUEST

Data acquired using the fast visible imaging system and SOL probes during the compact toroid (CT) injection in the Ohmic target plasma. Edge and SOL turbulence and flow was the main target right after the CT injection when the visible emission is enhanced considerably due to large amount of neutral injection into the plasma from the CT injector following the CT itself. Plasma current is maintained initially for about 300 ms and thereafter a steady fall is observed. Strong edge turbulence and enhanced poloidal rotation was observed during the 200 ms data acquisition window. I developed an orthogonal dynamic programming based particle image velocimetry (PIV) code for analyzing the image sequence and thereby determining the poloidal and radial velocities (in 2D). This code has been employed successfully on these images and fruitful inferences can be drawn about the plasma behavior. Fig. 2 shows the discharge parameters and two consecutive images denoting the development of a distinct mode with high poloidal mode (m) number at the plasma core.

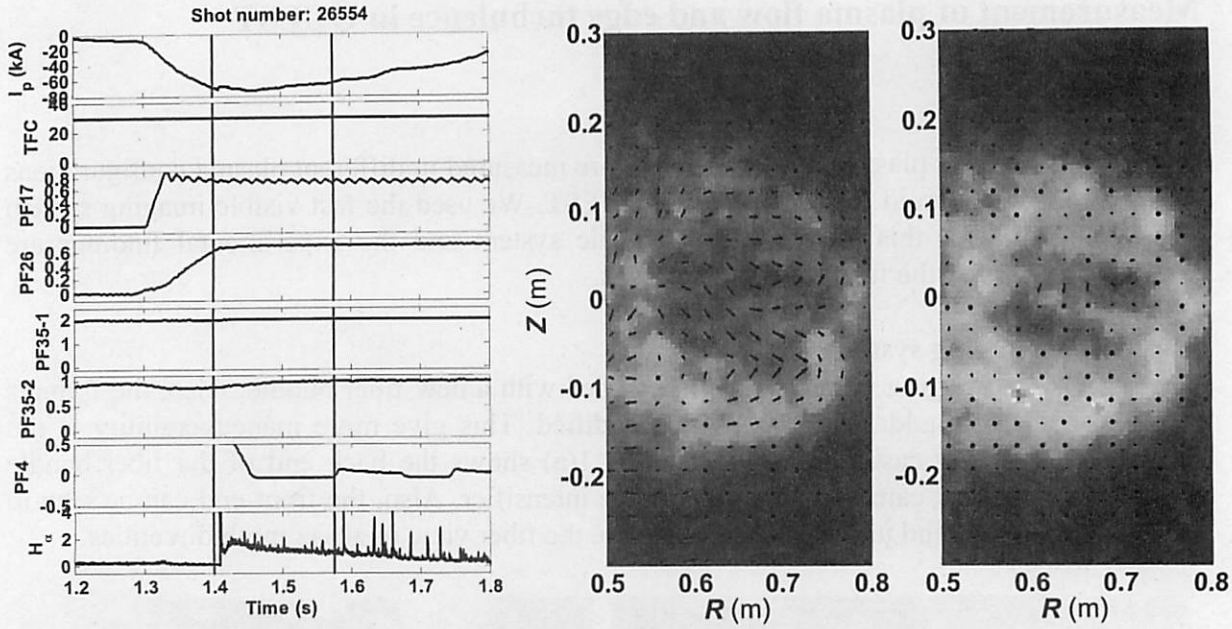

Fig. 2: left: discharge parameters of the Ohmic plasma injected with CT. The red lines indicate the image acquisition window. Right: the consecutive images showing a distinct mode developed in the plasma core. The black arrows are from the PIV analysis. Towards the left of the images there is the center stack at R = 0.22 m and neutrals appear to penetrate the plasma from the high field side. PF and TF stand for poloidal and toroidal field coils respectively.

Further, data for the edge turbulence and SOL is acquired just after the CT is injected. Strong flow at the SOL is observed. Fig. 3 shows a series of snap shots from the plasma edge in false color acquired with the fast camera at 20 kHz.

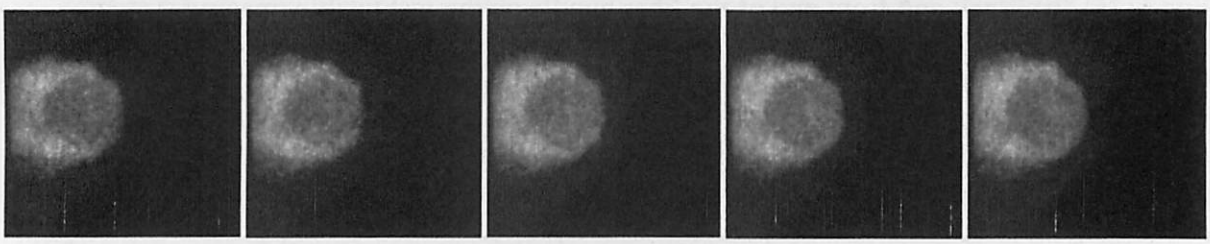

Fig.2: Shot #31114: Image sequence of CT injected plasma. From left to right the images are 50 μs apart.

Measurement of plasma poloidal flow at the edge in two different plasma configurations is also attempted. The first one is inboard limiter (IL) bound, while the second one is an inboard poloidal null (IPN) natural divertor configuration. Both the IL and IPN configuration can be achieved by suitably adjusting the poloidal field coil configuration and non-inductively driving the plasma current. 8.2 GHz ECRH system has been used for pre-ionization and thereby driving the plasma current in these plasmas. Here, three different diagnostics are used viz. the fast visible imaging system, Mach probes and the 1 m focal length Czerny-Turner spectrometer to measure the toroidal and poloidal velocities from Doppler shifted C III (464.7 nm) line. PIV technique is again employed in these image sequences and yields interesting results. Efforts are on to calculate the toroidal and poloidal velocities from the line integrated optical emission signals from the Doppler spectroscopy. Finally, the flow speed at the SOL

will be determined from the Mach probe signals. These three measurements will give us comprehensive information about the intrinsic plasma rotation, its profile and behavior of the SOL and how this changes with the plasma configuration. The final goal is to study the effect of intrinsic rotation on the plasma equilibrium and vice versa.

Fig. 4 shows a series of snap shots from the plasma edge in false color acquired with the fast camera at 20 kHz. Turbulent edge fluctuations in the images are superimposed with the velocimetry estimations. The black arrows show the direction of velocity at that time instant. The arrow size denotes the velocity magnitude.

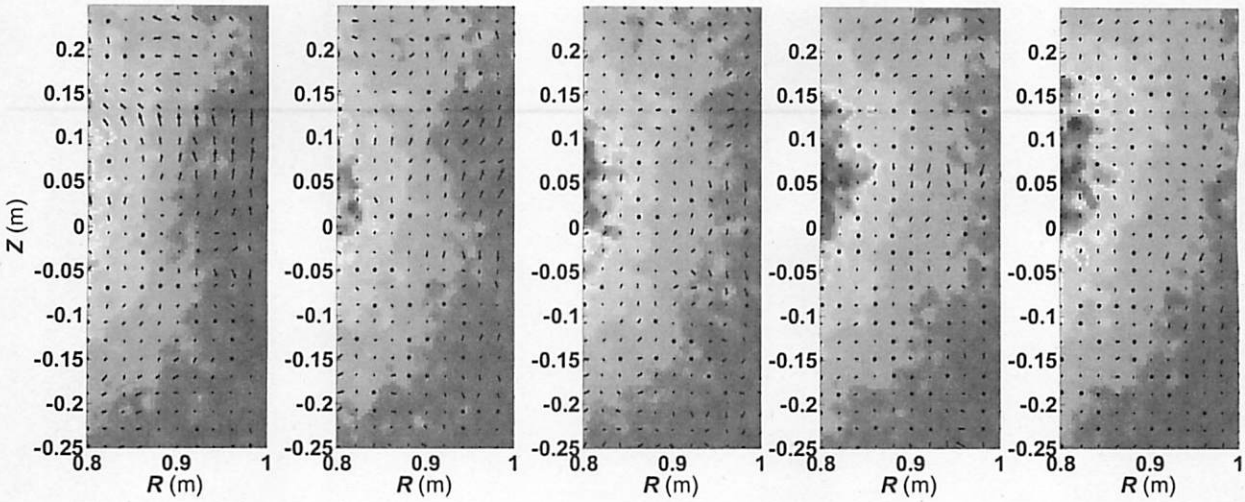

Fig. 3: Image sequence of IPN configured plasma superimposed with turbulent velocity maps from the PIV analysis. From left to right the images are 50 μs apart.

Acknowledgements
I gratefully acknowledge the support of my PhD supervisor Prof. H. Zushi, my collaborator Dr. T. Onchi and all other AFRC staff during the tenure of this collaborative effort. This work was supported in part by the International Joint Research Program of Research Institute for Applied Mechanics, Kyushu University.

Publications:

1. **Santanu Banerjee**, H. Zushi, N. Nishino, K. Mishra, T. Onchi, A. Kuzmin, Y. Nagashima, K. Hanada, K. Nakamura, H. Idei, M. Hasegawa, and A. Fujisawa, "*Dynamical programming based turbulence velocimetry for fast visible imaging of tokamak plasma*", Rev. Sci. Instrum., **86**, 033505 (2015).

2. T. Onchi, H. Zushi, K. Mishra, Y. Mahira, K. Nagaoka, K. Hanada, H. Idei, M. Hasegawa, K. Nakamura, A. Fujisawa, Y. Nagashima, K. Matsuoka, S. Tashima, **S. Banerjee**, A. Kuzmin, S. Kawasaki, H. Nakashima, A. Higashijima, and O. Watanabe, "Heat flux and plasma flow in the far scrape-off layer of the inboard poloidal field null configuration in QUEST", Phys. Plasmas 22, 082513 (2015).

3. Kishore Mishra, H. Zushi, H. Idei, M. Hasegawa, T. Onchi, S. Tashima, **S. Banerjee**, H. Hanada, H. Togashi, T. Yamaguchi, A. Ejiri, Y. Takase, K. Nakamura, A. Fujisawa, Y.

Nagashima, A. Kuzmin and QUEST team, "Self organization of high βp plasma equilibrium with an inboard poloidal magnetic field null in QUEST", Nucl. Fusion **55** 083009 (2015).

Oral presentation:

1. **Santanu Banerjee**, H. Zushi, N. Nishino, K. Mishra, T. Onchi, A. Kuzmin, K. Hanada, Y. Nagashima, K. Nakamura, H. Idei, M. Hasegawa, A. Fujisawa and the QUEST Team, "Edge turbulence and SOL flow in the electron cyclotron waves overdriven Ohmic plasmas in QUEST" at the 5th Asia Pacific Transport Working Group International Conference (APTWG 2015), June 09-12, 2015, Dalian, CHINA

国際化推進共同研究概要

No. 3

タ イ ト ル: Towards high mode purity in ECRH transmission lines for ITER

研究代表者: KASPAREK, Walter, Hermann

所内世話人: 出射 浩

実 施 期 間: 2016 年 3 月 21 日 ～3 月 26 日

研 究 概 要:

ITER における高効率大電力伝送には、主伝送モードから高次不要モードの励起が問題となる。高次不要モードはアーキング、過熱といった問題を引き起こす。高次モード励起を実験的に精査するため、高純度主モード励起が必要となる。共振器を用いたモード発生器が提案されたが97%励起に留まっている。共振器でのモード選択性の確認を進めた。伝送モードを解析するために、モード分析器を開発し、ドイツ ASDEX 装置にて高電力試験を行い、良好な動作を確認した。ITER での MHD 不安定性の安定化に用いられる高速ミリ波切替器を2周波数で動作させる方式の低電力試験を九州大学で行った。2周波数動作で必要とされる運転領域で良好な動作を確認した。

Towards high mode purity in ECRH transmission lines for ITER

Applicant: Walter Kasparek

Institute of Interfacial Process Engineering and Plasma Technology (IGVP)

Electron Cyclotron Heating (ECH) using high power millimeter waves is an attractive method for plasma production, auxiliary heating, and current drive in a nuclear fusion research. Accordingly, the ECH system at the International Thermonuclear Experimental Reactor (ITER), will have a total injected power of 20 MW at an operating frequency of 170 GHz. For 20 MW injection to the plasma, 24 high-power gyrotron oscillators of 14 MW each will be used. The output beam from each gyrotron oscillator is led to a Circular Corrugated (CC) waveguide line, and transmitted as an HE_{11} mode of a main eigen-mode in the waveguide. 24 CC waveguide lines will be prepared to transmit the total 20 MW power. Excitation of unwanted higher-order modes in the oversized waveguide causes many problems such as excessive transmission loss, arcing, thermal overload of components due to stray radiation, and finally deviations of the launched beams from the nominal direction. In earlier works, transmission losses in the ITER ECH system due to higher-order mode excitation in misaligned components have been estimated, and the impact on the launched beams was studied.

This collaboration has been established to excite and transmit the high-purity main HE_{11} mode under monitoring and controlling of the transmitted wrong modes for the CW high power application.

The International Joint Research team consisted (besides the applicant) of Hiroshi Idei (RIAM, Kyushu), Keishi Sakamoto (JAEA Naka), Takashi Shimozuma (NIFS, Toki), Richard Temkin (MIT PSFC Cambridge), Michael Shapiro (MIT PSFC Cambridge), Alexander Zach (IGVP Stuttgart), Carsten Lechte (IGVP Stuttgart), and Burkhard Plaum (IGVP Stuttgart).

HE_{11} Mode Generator

The high purity HE_{11} mode exciter is required for comprehensive studies on mode excitation and effects of misalignment in the Circular Corrugated (CC) waveguide transmission. It has been developed for studies in various millimeter-wave applications with the CC waveguide, as well as in the ITER ECH system.

In the past year, some work has continued aiming at the generation of a pure HE11 mode on one hand and the generation of pure high-order modes in a folded 170 GHz resonator system. Still, the HE_{11} (LP_{01}) mode purity is only 0.97; however, experiments are prepared, where the resonator will be operated in a dual polarization mode for higher performance. In the experiments on higher-order modes, LP_{11}^{even} and LP_{11}^{odd} modes could be excited with good purity. Figure 1 shows HE11 and LP11 modes patterns excited in the 170 GHz folded resonator by injection of a gaussian beam at appropriate angle and resonant tuning. The production

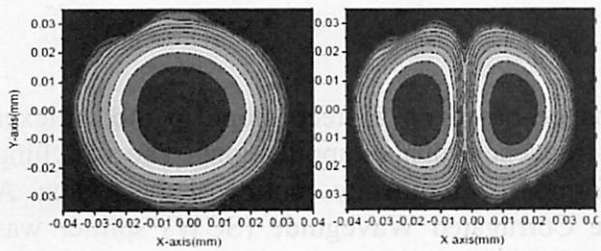

Fig.1 HE11 and LP11 modes excited in the 170 GHz folded resonator by injection of a gaussian beam at appropriate angle and resonant tuning.

of modes like LP_{02} was not successful, probably owing to the astigmatic design of folded resonators. Further investigations on this issue are planned.

In-situ mode analyzer

For reliable operation of high-power cw transmission systems, detection and mitigation of higher-order modes is of major importance. Therefore, the development of in-situ mode analyzers continued. An advanced 6-mode analyzer was built at RIAM, confirming the detectability of various wrong modes in HE11 waveguides.

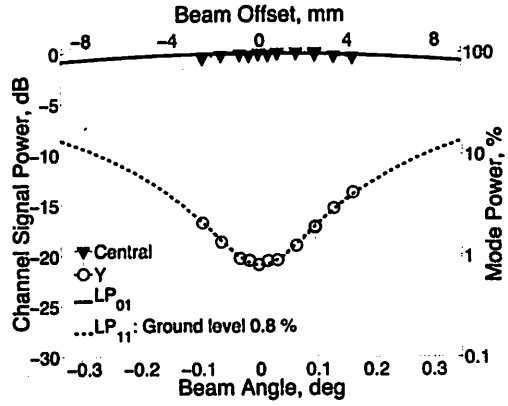

Fig. 2: Coupler signals of LP01 (main mode) and LP11 (tracer mode for misalignment) as function of the misalignment of the gyrotron beam with respect to the waveguide axis.

High-power tests with a prototype 5-port coupler from IGVP were performed at the ECH system of the tokamak ASDEX Upgrade. Here, the gyrotron beam – after having passed the matching optics unit – was scanned with a mirror over the input aperture of the corrugated waveguide, and the generation of the tracer modes for angular misalignment as well as beam displacement (LP11, even/odd), were measured as function of the input angle as shown in Fig.2. It could be clearly demonstrated that alignment of the gyrotron beam coupled into the waveguide could be performed on the basis of the coupler signals only, as – within the errors of the various methods of typ 0.1 degree – good agreement with geometrical and laser beam alignment was found. The result (example see Fig. 1) opens the possibility to get a continuous control of the gyrotron input beam such that the wrong mode content in the transmission line is minimized.

These results were obtained by summation of two coupler signals each. However, an individual measurement of amplitude and phase of the coupler signals gives more options for evaluation of the coupler signals. Usually, heterodyne techniques are used for this, taking a power signal as local oscillator. However, owing to the different power levels of gyrotron and detection electronics, such systems are complicated, expensive, and prone to errors. Therefore, it was started to develop compact and robust single-sideband modulators on the basis of rotating gratings. First test have shown sufficiently stable signals at the intermediate frequency even for fast variation of the input (generator) frequency.

In parallel, a 7-port coupler is under design, where 2 coupler signals are generated from a single waveguide by using 0th and 1st-order interference in the coupling waveguides. Calculations on the suppression of wrong modes other than the modes to be detected are going on. All developments are made in view of application in cooled (mitrebend-) mirrors which can tolerate heat loads and thermal stress typical for high-power CW operation. In addition, attempts are made to extend the developments on 2-frequency operation, and on mode control of gyrotrons by integrating these couplers into the first mirror of the matching optics unit.

Dual frequency FADIS

A FAst DIrectional Switch (FADIS) performance based on a steep slope in the diplexer transmission function was considered for dual-frequency (dual-*f*) applications. The switching between the output transmission lines is performed by frequency control of the source. A diplexer for a FADIS system using a Square Corrugated Waveguide (SCW) splitter was designed as one of the most attractive candidates for the dual-*f* operation.

The splitter performance is a key issue for the dual-*f* operation, and extended operation regions in splitter operations have been considered and surveyed using mode contents analysis

based on matching coefficient evaluation. Some operational branches with high matching coefficients (> 0.9) were found, and new operating parameters were proposed for the dual-*f* operation in the JT-60SA ECHCD system. For the the JT-60SA ECHCD system, a normal branch operation and a 3rd new branch operation were proposed for the 110 and 138 GHz. Calculated radiation pattern distributions from the SCW splitter were defined very well with no serious side lobes in the dual-*f* operation. In this year, a new (3rd) branch operation was experimentally confirmed using 170 GHz SCW components in Kyushu University. Figure 3 shows measured split symmetric and anti-symmetric beam patterns at the 3rd branch operation in 170 GHz. There were no serious side-lobes , and the fine two split beams were obtained along the design.

In support to this work, the properties of high-power SCWs (designed for use as remote steering launchers at 140 GHz) have been investigated with respect to conservation of the polarization during transit through SCW splitters, and the concomitant transmission loss.

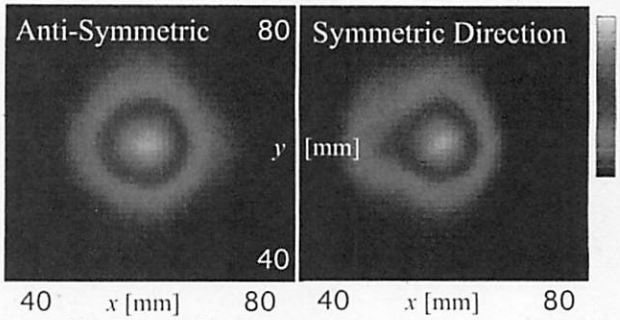

Fig. 3: Measured split symmetric and anti-symmetric beam patterns at the 3rd branch operation in 170 GHz.

It is found that corrugation profiles can be designed and machined with sufficient precision, such that for the nominal frequency and propagation angle, practically no cross-polarisation occurs. For deviations from the main frequency, cross-polarisation increases. However, revival of pure polarization is expected at a series of other (lower) frequencies. Therefore, dual-frequency operation (138 / 110 GHz) under arbitrary polarization should be possible, if the propagation angle of the SCW and the corrugation profile is chosen properly. More detailed investigations on this subject are planned.

The part of the transmission losses of a resonator ring, which is produced by the corrugated waveguide only, was measured in a resonator set up, which was formed by a splitter waveguide, a plane mirror at its one end, and a focusing mirror at the other. The round-trip loss of the resonator is derived from the Q-factor; the value obtained gives an estimate of the efficiency of a resonant ring for the case of perfect matching of the external feed-back reflectors.

国際化推進共同研究概要

No. 4

タイトル: Plasma start-up and sustainment in spherical tokamak configuration by RF

研究代表者: SHEVCHENKO, Vladimir

所内世話人: 出射 浩

実施期間: 2016 年 3 月 24 日 ～ 3 月 25 日

概要:

平成28年3月24−25日の2日間に国際WSを開催した。欧州から2名、国内の学外者が5名と応研関係者の参加があった。QUESTの電子バーンシュタイン波加熱・電流駆動及びプラズマ・壁相互作用に関する議論を実施した。QUEST 実験の最近の進展に加え、国内外実験の進展、新たな運動論的理論・シミュレーション解析などが議論された。

RF-only ST plasma confinement, sustainment, and interactions with wall materials

Vladimir Shevchenko

A program of the Workshop which was held on March 24-25th is the followings.

24-March

AM

9:00-

Vladimir Shevchenko / Hanada

WS purpose and agenda

9:10-10:10

Alf Köhn

Microwave-plasma interactions in a low-temperature stellarator

10:20-11:20

Vladimir Shevchenko

Present status of ST25 and progress with ST40

11:20-12:20

Roger Raman

CHI System Design and Plans on NSTX-U and QUEST

PM

13:45-14:25

Yuichi Takase

LH Ip Ramp-up Experiments on TST-2

14:25-15:05

Naoto Tsuji

Measurement of lower- hybrid waves with microwave scattering on TST-2

15:15-15:45

Kazuaki Hanada

Progress and Plans of QUEST Experiments (Tentative)

15:45-16:15

Hiroshi Idei

New 28 GHz and 8.5 GHz systems and its application to QUEST experiments (tentative)

16:15-16:45

Ryota Yoneda

2nd Harmonic Electron Cyclotron Break Down in QUEST (Tentative)

16:45-17:25

Masaaki Uchida

EBW start-up experiment in LATE

25-March

9:00-9:40

Atsushi Fukuyama

Modeling of EC heating and current drive in QUEST plasmas

9:40-10:30

Shabbir Khan:

Kinetic full wave modeling in inhomogeneous plasmas

10:30-11:00

Md Mahbub Alam

Current Density Profile Estimation from High Energetic Electron Orbits (Tentative)

11:00-11:30

Alexander Kuzmin

Plasma Permeation Diagnostics in QUEST (Tentative)

11:30-12:30

Naoaki Yoshida

Study on Plasma-Wall Interaction in QUEST equipped with High Temperature Tungsten Wall Aiming for Active Particle Control

PM (Drafting of proposals for experiments, diagnosis, and analysis)

13:30- All Suggested focus and output for this joint drafting session

15:30- Summary

The presentation abstracts are the followings.

Naoto Tsuji: Measurement of lower- hybrid waves with microwave scattering on TST-2

The experimentally measured current drive efficiency on TST-2 is lower than the predictions by numerical simulations. In order to resolve this discrepancy, a microwave scattering diagnostics at 12-40 GHz was designed and is being fabricated. Synthetic diagnostic was developed to estimate the scattered power theoretically. The LH fluctuation amplitude simulated with a full-wave code was found to be within the detectable range.

Hiroshi Idei: New 28 GHz and 8.5 GHz systems and its application to QUEST experiments (tentative)

A hybrid launcher system was developed to conduct the 28 GHz and 8.5 GHz ECH/ECCD experiments. Highly focused beams were obtained using the developed launcher system. The 20 kA plasma was startup using the new 28 GHz launcher system.

Md Mahbub Alam:Current Density Profile Estimation from High Energetic Electron Orbits (Tentative)

The current density distributions in electron cyclotron heated plasmas were estimated from the orbit analyses at Doppler-shifted EC resonances for the 8.2 GHz ECRH/ECCD. Because the incident 8.2 GHz beam was not focused, the uniform distribution of the electrons in real space and the uniform electron velocity distribution were also assumed here. The parallel refractive indexes ($N_{||}$) from -1 to +1 were taken into account, being similar to that for the 28 GHz injection when one path absorption was not expected and multiple wall-absorption should be dominant due to improper incident electric polarization [2]. The electrons with the initial parallel and perpendicular velocities $v_{||}$ and $v_{\perp}$ were considered for the orbits and current density analyses with nonrelativistic resonance condition and collision-less approximation. From this calculation, the current density distributions were obtained separately for the fundamental and the second harmonic resonant electrons. The current density distribution profiles on the equatorial plane were obtained for the electrons with

initially positive and negative parallel velocities to the magnetic field direction as well as trapped electrons. The surface averaged current density profiles of the closed flux surfaces were also evaluated. A small amount of the positive current density distributions were partially appeared in the outside region from the last closed flux surface, while all the negative current density distributions were evaluated in the inside of the last closed flux surface. The trapped electrons being the second harmonic electron cyclotron resonant contributed the negative current in the inside of the last closed flux surface as well as partially contributed the positive current both in the inside and the outside region of the last closed flux surface.

Alexander Kuzmin: Plasma Permeation Diagnostics in QUEST (Tentative)

Real-time in-situ measurements of the the hydrogen retention is studied to reveal essential retention areas in the spherical tokamak QUEST with all tungsten and stainless steel plasma facing components. High hydrogen retention, 70-80% of injected particles was previously reported. Hydrogen permeation is measured with four fixed PdCu permeation probes (PP) at the top, bottom (TB) plates and at the upper and lower positions on the side vessel wall. Incident retention flux was numerically calculated. A movable PP is used for a radial profile measurements of the hydrogen retention along the major radius (R) outside and behind the plasma facing components (PFCs). At the same time contribution of the hydrogen to the retention is evaluated using ion saturation current (I_s), measured by the movable Langmuir probe at the same port. An array of Langmuir probes is also used for TB plates. Two types of discharges are studied: annular slab plasma, produced by 2.45 GHz or 8.2 GHz ECWs (<20 kW) and non-inductive IPN steady-state tokamak plasma (SST) produced by 8.2GHz ECWs [3] (<100 kW), plasma duration is in range 300-900 s. In the slab annular plasma with well controlled gas balance and plasma performance response of the probes is studied to external perturbations. Permeation flux decays from ~1.5×10^{18} $H\cdot m^{-2}s^{-1}$ at maximum insertion (R~1.1m) to ~5×10^{17} $H\cdot m^{-2}s^{-1}$ at the wall radiation shield. Inside the port permeation raises to ~7×10^{17} $H\cdot m^{-2}s^{-1}$. In the SST plasma retention, flux to the side wall normally exceed retention flux to the TB plates by 2-10 times. Langmuir probes show that maximum of the I_s radial distribution on the TB plates is located at R ~ 0.4-0.5 m, close to the PDP. The contribution of atomic hydrogen flux to the retention was larger than that of the ion flux. Retention flux on the upper side wall (ion drift side) was larger than on the bottom one. Hence maximum of the atomic flux poloidal distribution is at the upper side wall. New measurements are required for the main PWI area at the center stack, which are planned for the future work.

Alf Köhn::Microwave-plasma interactions in a low-temperature stellarator

Microwave heating is a widespread method to transfer energy to the plasma. While standard electron cyclotron resonance heating (ECRH) is a well-established and understood technique, it can only be applied if the plasma density does not exceed the cut-off density. If the latter is the case, the plasma is referred to as over-dense and other microwave heating scenarios have to be considered. This talk gives an overview about these scenarios with the emphasis on experiments carried out at the stellarator TJ-K. The experiments are accompanied by full-wave simulations. They serve on one hand to optimize the coupling to the plasma and on the other hand to understand some general aspects of the plasma-microwave interactions. One of the heating scenarios, coupling to electron Bernstein waves, is of special interest to the spherical tokamak and will therefore be discussed in detail.

Roger Raman: CHI System Design and Plans on NSTX-U and QUEST

Transient CHI is the primary method to be used for solenoid-less plasma start-up on NSTX-U in a planned scenario for full solenoid-free plasma start-up and non-inductive current ramp-up. This is an important objective of the NSTX-U research program. The encouraging transient CHI physics demonstration results from NSTX motivated us to proceed with the next step – that of examining alternate, simpler, CHI configurations that may be much easier for implementation in reactors. These exciting studies in a new CHI electrode configuration will be conducted on the QUEST ST.. For implementation of CHI, one of the important requirements is that two coaxial electrodes must be electrically separated from each other, and magnetic flux must connect these electrodes. Reference [1] describes a possible installation concept on a ST-FNSF (Fusion Nuclear Science Facility). The CHI electrode configuration on QUEST has many similarities to the second electrode configuration described in Ref. [1]. A successful demonstration of transient CHI start-up on QUEST has the potential to considerably simplify the implementation of CHI in future tokamak/ST-based devices. In addition to testing the alternate electrode configuration, transient CHI studies on QUEST would contribute to a number of near-term important physics studies, before these could be conducted on NSTX. First, and the most important, is an assessment of the capability of the ECH system on QUEST to increase the electron temperature of CHI initiated plasmas. This is a necessary and important step to enable neutral beam current drive in CHI initiated targets. The second important study is an assessment of the capability of an all-metal system to reduce radiative losses from low-z impurities during the plasma start-up process. The QUEST device, which is equipped with reactor-relevant technologies, is an ideal device for these important studies, which can lead to a simplification of the ST and AT concepts [2]. The transient CHI seed plasmas may also provide an alternate plasma target for RF studies. These are: (a) Low and high density plasma targets with density profiles different from those generated in conventional RF discharges, and (2) biasing capability to alter edge density conditions in conventional RF discharges. Finally, the development of steady-state CHI discharges remains a long-sought goal of the helicity injection program, which requires metal electrodes and ECH heating capability – both of which are part of QUEST capabilities. The QUEST device is now configured with the CHI electrodes to support these experiments. The pulsed gas injection system that is necessary to minimize the injected gas while ensuring reliable discharge initiation has been built by the Univ. of Washington, and will be installed on QUEST during the upcoming outage. A 40kJ, 2kV capacitor based power system, and a voltage snubber system, similar to the ones used on NSTX, has also been built by the University of Washington, and is at present being commissioned at the QUEST facility. We anticipate initiating transient CHI experiments during the next QUEST run campaign. The CHI system differences and similarities of the configurations on QUEST, NSTX-U and the proposed ST-FNSF design will be discussed. The status of CHI hardware required for physics studies and a description of the plans for the first CHI experiments to be conducted on QUEST and NSTX-U will be described.

[1] R. Raman, et al., Fusion Science and Technology **68**, 674 (2015)

[2] R. Raman, et al., Journal of Fusion Energy **35**, 34 (2016)

国際化推進共同研究概要

No. 5

タ イ ト ル: CHI experiment and the related research on plasma physics in QUEST

研究代表者: NELSON, Brian, A

所内世話人: 花田 和明

実 施 期 間: 2016 年 3 月 25 日 ～ 3 月 26 日

研 究 概 要:

平成 28 年 3 月 25－26 日の 2 日間に国際 WS を開催した。欧州から 2 名、TV 会議システムで米国から 2 名、国内の学外者が 4 名と応研関係者の参加があった。

今回は MAST の Shevchenko 氏の共同研究との共催として実施した。残念ながら Peng 氏は参加できなかったが、第1回、第2回ともにワークショップに参加した Shevchenko 氏が中心となって QUEST の電子バーンシュタイン波加熱・電流駆動及びプラズマ・壁相互作用に関する議論を実施した。議論の内容は 26 日に Shevchenko 氏によってまとめられた。

Schedule for CHI systems commissioning (March 22 – April 1)
Work completed is shown in grey color

March 22-23:

1. Install capacitor and ignitrons in capacitor bank, and prepare it for power testing. Do not energize the high-voltage components.
2. Configure as follows:
    a. Ignitron 1 – connected to 2 capacitors
    b. Ignitron 2 – connected to 3 capacitors

March 24:

1. Morning – Go over the procedure to conduct initial hi-voltage tests into a dummy load (do not energize high-voltage components)
2. Prepare all components needed for high-voltage testing
3. Inform Rogers-san on procedure to access Labview control signal (only a ON/OFF signal is needed)

March 25:

1. Go over the high-voltage operating procedure, and test fire the capacitor bank at low voltage (Manually at V < 1kV)
2. Test all control relays in the capacitor bank and the gas injection system using the Labview ON/OFF signal. Rogers-san and Nagata-san to do this
3. Nagata-san (and Responsible person on QUEST) to make good notes, and take photos of all internal components of the capacitor bank, and understand role of different wires and relays inside the capacitor bank. Nagata-san to check the tightness of all screws and bolts and nuts in the capacitor bank.
4. Discuss the safety issues and how to protect personnel

March 26: (Saturday)
If we are behind with the above schedule, work on Saturday to catch-up.

March 28:

1. Go over the high-voltage operating procedure one more time, and test fire the capacitor bank into a dummy load at higher power (Manually, at up to 2kV)
2. **Go over the details of the snubber hardware components, and work out the procedure for installation on QUEST.**
3. **Go over the procedure for hi-potting the CHI hardware on QUEST**

March 29:

1. Test parts of the gas injection system using the Labview controller
2. Test fire the gas injection valves using the Labview controller
3. **Update the control logic**
4. **Discuss building larger gas injection plenum**

March 30:

1. Test fire the capacitor bank using the Labview controller
2. **Update the control logic**

March 31 and April 1:

1. **Contingency days and for QUEST personnel to become familiar with capacitor bank and gas injection system operating and maintenance details.**

2. Continue to operate the gas injection system and the capacitor bank (at low power) using the Labview interface and update the control logic

Remaining Tasks before CHI Operations on QUEST:

General
Discuss safety issues for cap bank.

QUEST side

Gas System:
Gas lines need to have insulating breaks. Could be fabricated out of PEEK insulator and good for 4kV.

Does the TIV on the machine need remote control capability?

Snubbers and Voltage Monitors:
Housing is needed for the three snubbers. Put the snubber inside a plastic box, and put the plastic box inside a metal box.

An adapter flanges is needed to connect the snubber to the current feed rods.
4 coax cables from each snubber (each about 1 m long) to be connected to this adapter plate.

The adapter plate should also have a place to connect the fast voltage monitor.

A voltage monitor is needed at each current feed location. The signals from these voltage monitors need to be archived by the QUEST data acquisition system. Required frequency is >1MHz

It may de desirable to connect the current feed cables from the capacitor to this same adapter plate.

The Analog output FOT channels C and D be adjusted, and their stability for drift over a long period should be checked - to give 0.10V output at 0.10 input

U-Washington side

UW will build and ship 6 capacitor shorting resistors and install, it during next trip.

UW will build and ship 3 fast voltage monitors to be installed on the current feed rods

Figures attached in the next 2 pages

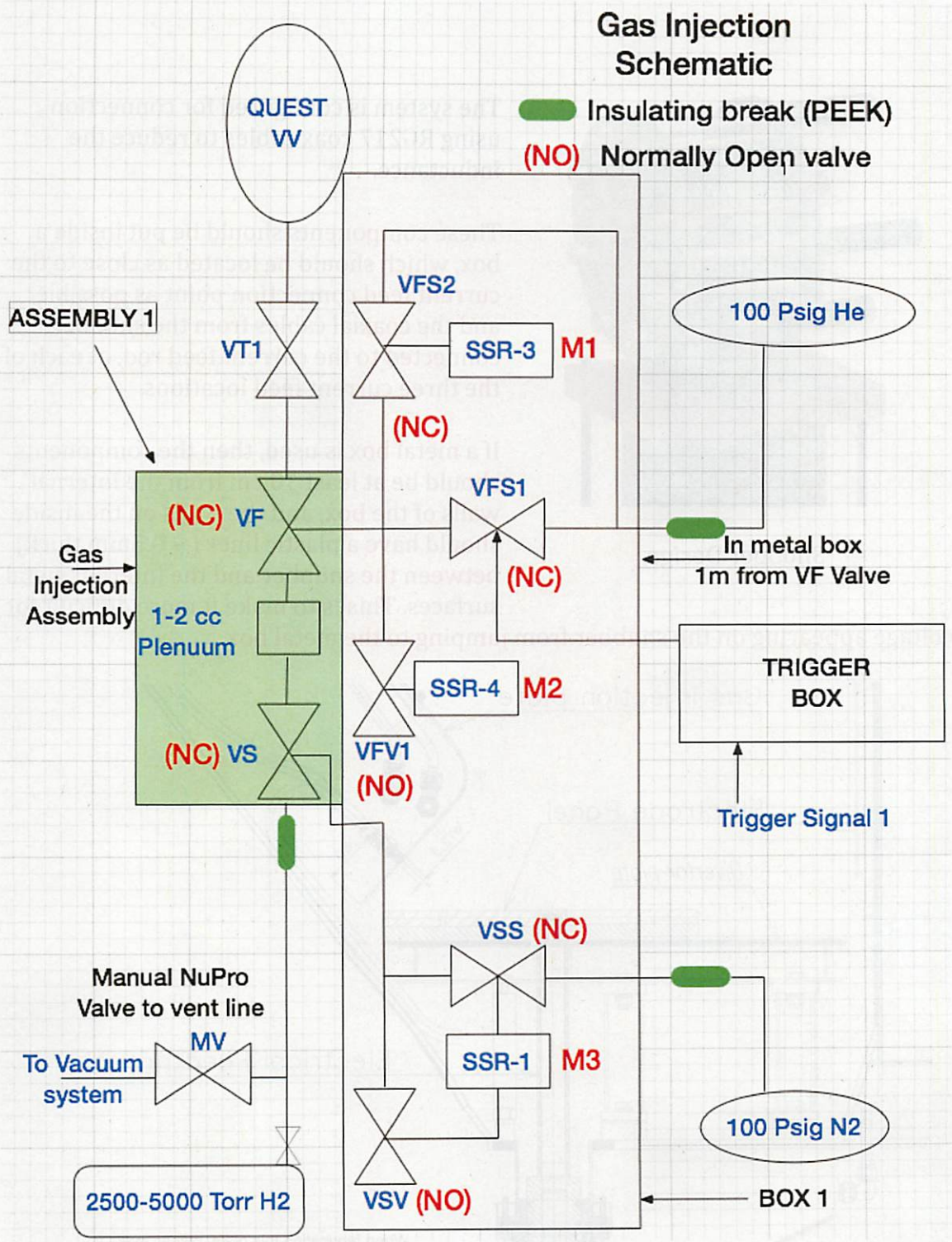
Gas Injection Schematic
Insulating break (PEEK)
(NO) Normally Open valve
QUEST VV
ASSEMBLY 1
VT1
VFS2
SSR-3
M1
(NC)
100 Psig He
(NC) VF
VFS1
(NC)
In metal box
1m from VF Valve
Gas Injection Assembly
1-2 cc Plenuum
TRIGGER BOX
SSR-4
M2
(NC) VS
VFV1
(NO)
Trigger Signal 1
VSS (NC)
Manual NuPro Valve to vent line
MV
To Vacuum system
SSR-1
M3
100 Psig N2
2500-5000 Torr H2
VSV (NO)
BOX 1

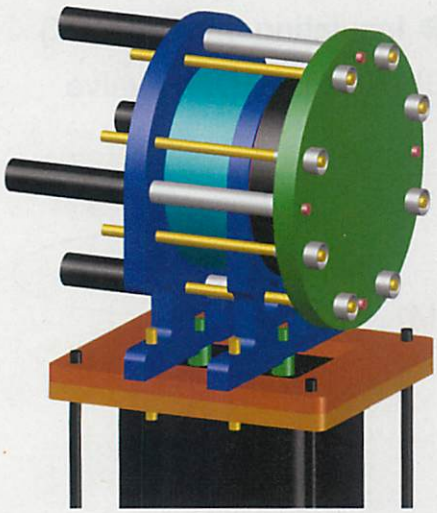

Snubber Design

The system is configured for connection using RG217 coax cables to reduce the inductance.

These components should be put inside a box, which should be located as close to the current feed connection point as possible, and the coaxial cables from the snubber connected to the current feed rod, at each of the three current feed locations.

If a metal box is used, then the components should be at least 10 cm from the internal walls of the box, and the walls on the inside should have a plastic liner (~ 0.5mm thick) between the snubber and the internal metal surfaces. This is to make it more difficult for the voltage appearing on the snubber from jumping to the metal box.

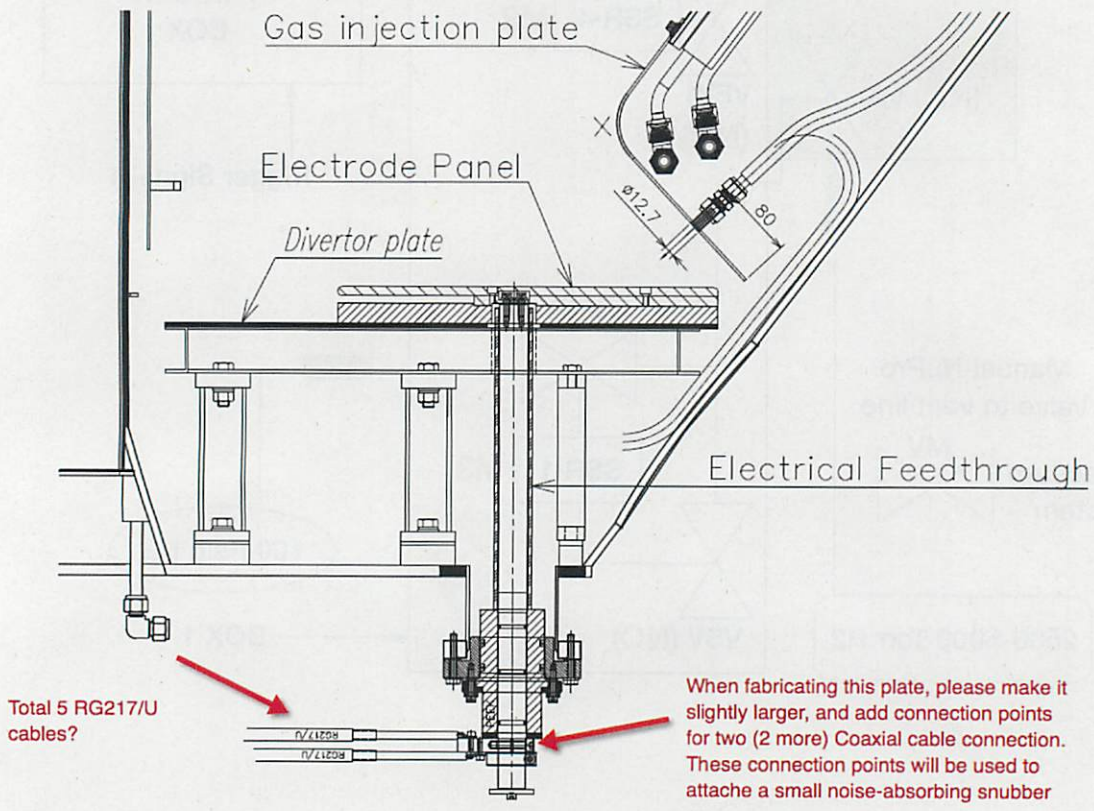

国際化推進共同研究概要

No. 6

タ イ ト ル: Joint study of long pulse high beta discharges and related egde turbulence transport in steady state operation (SSO) plasmas on QUEST and EAST

研究代表者: GAO, Xiang

所内世話人: 花田 和明

実 施 期 間: 2015 年 11 月 5 日 ～ 11 月 11 日

概要:

トカマクの長時間運転に関する包括的共同研究であり、今年度大きな進展があったのはTRIAM、QUESTで開発されたパワーバランスの計測法をEASTに適応してパワーバランスを計測する研究である。

実験装置の設置は中国側資金(the National Magnetic Confinement Fusion Program of China with Contract No. 2014GB106000 (Prof. Gao))によって支援され、実験を開始する準備が整った。大学院生博士後期課程学生の濱田君(濱田君の派遣費は日本側(GA経費)、滞在費は中国側負担)を 1 か月半派遣し、データを取得した。中国側でも大学院生 1 名がこの研究を担当している。実験結果は 3 月に韓国で行われる国際WSにて発表予定である。

RESEARCH REPORT

Date: Nov. 19, 2015

Visiting scientists: (name) Xiang Gao

(position) Professor

(university / institute) Institute of Plasma Physics,
Chinese Academy of Sciences

(name) Yinxian Jie

(position) Professor

(university / institute) Institute of Plasma Physics,
Chinese Academy of Sciences

(name) Haiqing Liu

(position) Associate Professor

(university / institute) Institute of Plasma Physics,
Chinese Academy of Sciences

(name) Yukai Liu

(position) Ph. D student

(university / institute) Institute of Plasma Physics,
Chinese Academy of Sciences

Host scientist: (name) Kazuaki Hanada

(position) Professor

(university / institute) Kyushu University

Research period: (from) Nov. 5, 2015 (to) Nov.11, 2015

Research subject: **Joint study of long pulse high beta discharges and related egde turbulence transport in steady state operation (SSO) plasmas on QUEST and EAST**

Introduction

Steady state operation (SSO) of tokamak plasma is one of the basic requirements for future fusion reactors. Long pulse high beta operation is one of important missions for ITER. The mission of QUEST is to develop the scientific basis for achieving a steady state condition at sufficiently high beta (~20%), with high confinement and low collisionality. QUEST is a Sperical tokamaks(ST) which has the possibility to realize cost-effective fusion power plants because of High beta is the indispensable target. The mission of the EAST project is to study the physical issues involved in steady state advanced tokamak devices. Long pulse operation is directly related to ITER technology and operation. ITER-like divertor geometry and target structure has adopted to minimize the leakage of neutrals to the main chamber. Joint study long pulse high beta discharges in SSO plasma research field on QUEST and EAST is strongly supporting ITER experiment from both experience and theory. In addition, turbulence driven transport plays an important role in long pulse high beta plasma with SSO. In QUEST, the combination diagnostics of radial probe (Langmuir probe in mid-plane), divertor probes and fast camera is a powerful tool to study the edge turbulence (blobs, filaments) transport. In EAST, type I and type III ELMs and filaments has been observed in H-mode long pulse discharges. So joint study of transport on QUEST and EAST will provide some key understandings for SSO. And also, there are many other correlated branches of long pulse high beta SSO on QUEST and EAST, exploration study on new effective diagnostics and related confinement and transport issues with SSO is also meaningful.

The major motivation of this project is to realize SSO plasma, based on QUEST and EAST device. In 2015, this subtheme pursued in long pulse high beta discharges and related egde turbulence transport in SSO plasma on QUEST and EAST. Comparsion and

combination study of the results were done on both devices. The edge turbulence transport by blobs, filaments and ELMs has been observed in QUEST and EAST. To study the edge turbulence transport mechanism and how to control and suppress them is a crucial issue for long pulse high beta plasma in SSO on QUEST and EAST. Some results will be combined with previously experimental results in QUEST and then compared with new ELMy filaments results in long pulse high beta discharges of EAST tokamak. According to Prof. Hanada and Prof. Gao's discussions and ideas, based on Mr.Hamada's research work on QUEST, a new subproject, calorimetric measurement of heat load in EAST and QUEST, has been done and had a big progress in 2015. To achieve steady-state or long-pulse operation, it's important to investigate the power balance. Measurement of heat load and researching of power balance in EAST and QUEST will provide crucial support for ITER experiments. This subproject is also partly supported by the National Magnetic Confinement Fusion Program of China with Contract No. 2014GB106000 (Prof. Gao). To explorate joint study on new diagnostics and related plasma physics issues were also done in process of this EAST and QUEST collaboration subject. Due to the abundant progress and requirement of future research of this project, this joint research is hence advised to divide into two joint study subject in next year: (1) Joint study of high beta discharges and power balance in steady state operation (SSO) plasmas on QUEST and EAST; (2) Joint study of effective diagnostics and confinement and transport in steady state operation (SSO) plasmas on QUEST and EAST.

Recently experimental progress in QUEST and EAST

As well known, ITER 'hybird' need external no inductive current, to prepare favourable q profile; to sustain q profile on timescale required. Location must be compatible with current and pressure profiles, i.e. off-axis CD required. In EAST, LHCD is one of key tools. Of course, NBI, ICRF, New ECRH are also strong tools for new plasma scenario development on EAST. A fully non-inductive scenario had been demonstrated on DIII-D for EAST, as shown in Fig.1. In 2015 EAST experimental campaign, the operation regime

was extended with 4.6GHz LHW+NBI, as shown in Fig. 2.. The new 4.6GHz LHW show its higher capability on H&CD than 2.45GHz. Higher betaN with a broader current profile is reached under NB H&CD.

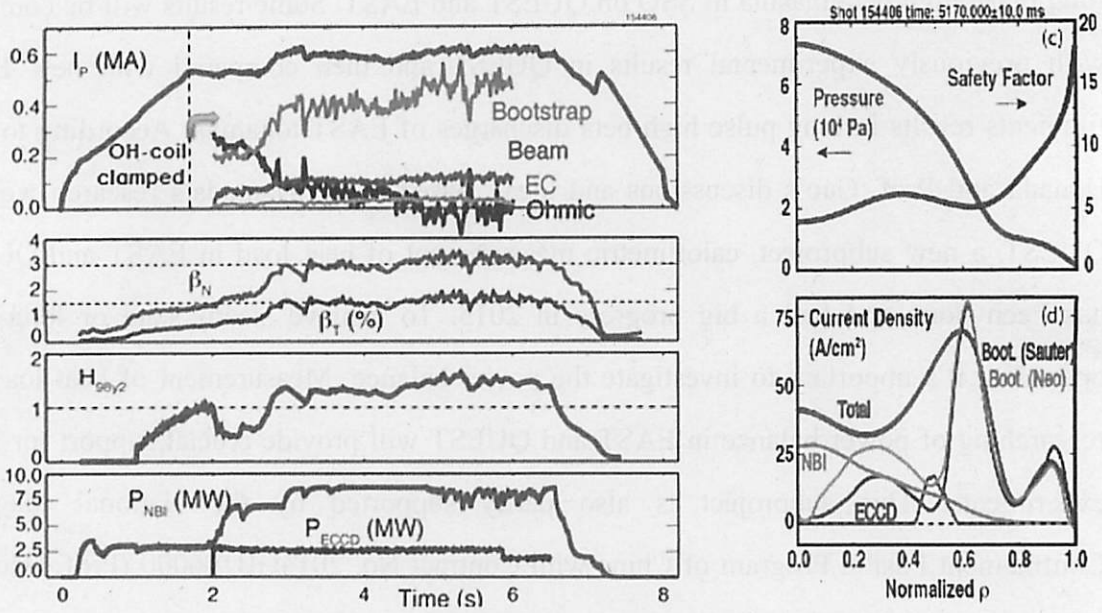

Figure 1 A fully non-inductive scenario had been demonstrated on DIII-D for EAST (Dr. Qian's presentation for discussions during this visit).

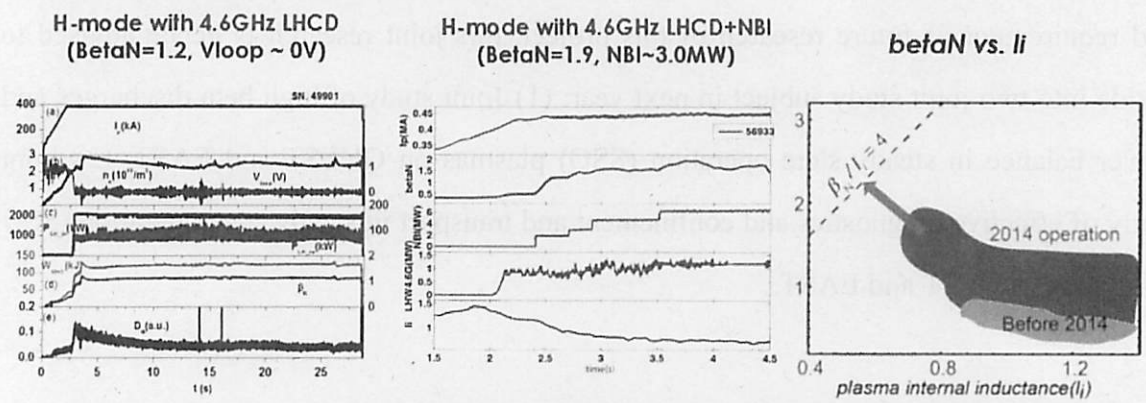

Figure 2 Extension of plasma operation regime with 4.6GHz LHW +NBI (Dr. Qian's presentation for discussions during this visit).

In QUEST, Fully Non-inductive current drive experiments using 28GHz and 8.2GHz electron cyclotron waves had been developed successfully. As shown in Fig. 3., 54kA plasma sustainment in low aspect ratio configuration by 28GHz injection was achieved. Plasma current of 54 KA was non- inductively sustained for 0.9 sec by only 28 GHz injection.The plasma shaping was almost kept for 1.3s. Non-inductive high current plasma

start-up by 2nd ECH/ECCD has been demonstrated. Spontaneous density jump across the cutoff density was observed in superposed 28 and 8.2 GHz injections. Ha intensity was kept, magnetic axis Rax and minor radius a were slightly decreased in the density jump case. Plasma current Ip was once decreased, but was recovered after the plasma shaping became more stable, as shown in Fig.4..

Different configurations, limiter, IBNULL, divertor, have been achieved in the steady state operation. Simplified QUEST-wall model can reconstruct the particle flux dependence for 400s long pulse discharges. For future plan, QUEST will be performed under hot wall to improve the controllability of Hydrogen recycling during long pulse plasma discharges (1000s). Detailed discussions with Prof. hanada allowed us to gather more information regarding the long pulse discharge activities and compared with the conditions on EAST.

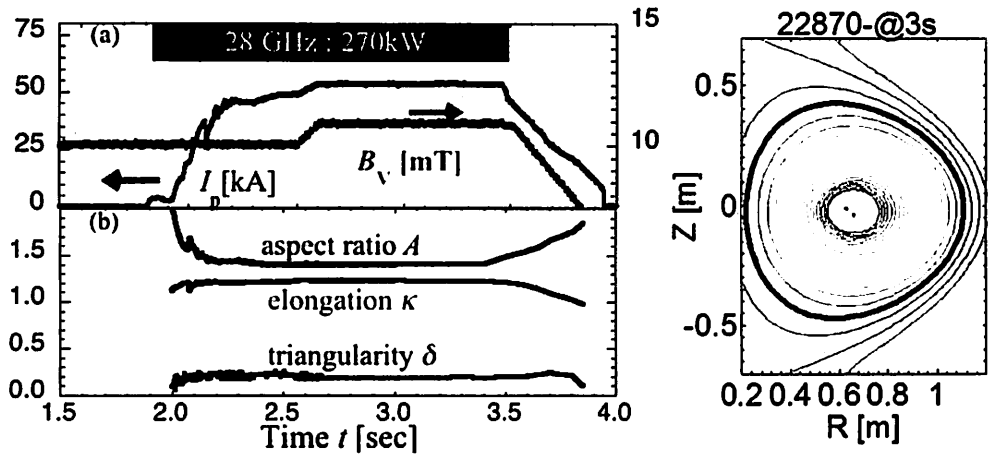

Figure 3 54 kA Plasma Sustainment in Low Aspect Ratio Configuration by 28GHz Injection (Prof. Hanada's presentation for discussions during this visit).

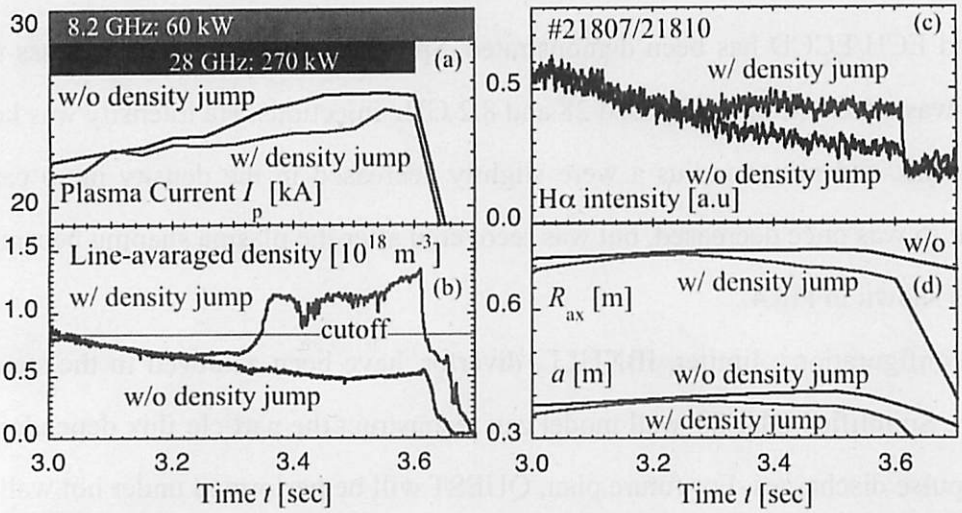

Figure 4 Over Dense Plasma Sustainment by 28 /8.2 GHz Injections after Spontaneous Density Jump (Prof. Hanada's presentation for discussions during this visit).

Plasma activities associated with current density profile and electron density profile, the current density profile is key parameter for real-time plasma control (q profile and current density relaxation) for long-pulse discharges: connect plasma (diagnostics) – PCS - actuators (ICRH,LHCD) - plasma response and extend high-performance plasma regimes to long-pulse in preparation for ITER. Current profile optimization or control is one of the key issue for advanced scenario development. 4.6GHz LHW phase scan and earlier H-modes show the capability to broaden current profile. The Polarimeter-interferometer(POINT) diagnostic has been installed on EAST for current profile measurement. Initial results of current profile from EFIT with Faraday rotation measurements was obtained, as shown in figure 5. The temporal resolution is up to 1us, the angle resolution ~ 0.1°, the the density resolution $1x10^{16}m^{-3}$. The POINT is the powerful tool for the real-time plasma control to get long pulse high beta discharges on EAST in future. Also the 11 Ch.s POINT data show effective diagnostics for LHCD phase control for scenario development on EAST, as shown in Fig. 6..

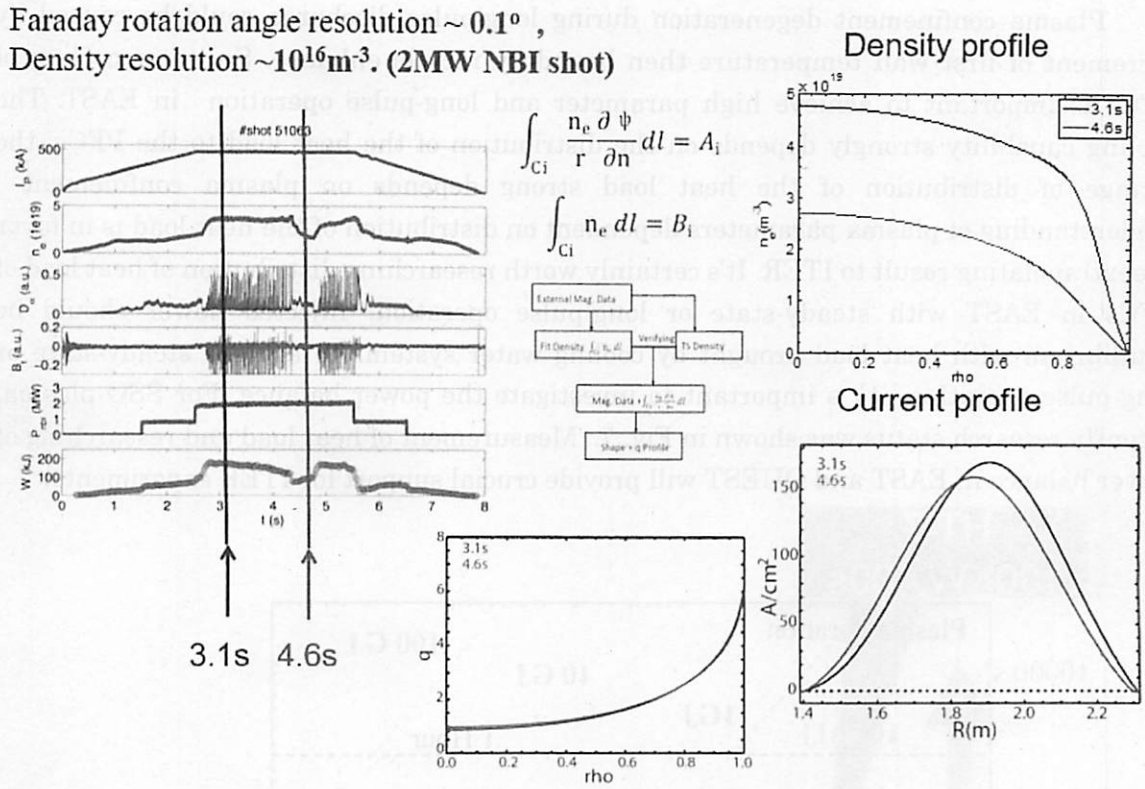

Figure 5 Initial results for current profile by POINT (Dr. Liu's presentation in QUEST building during this visit).

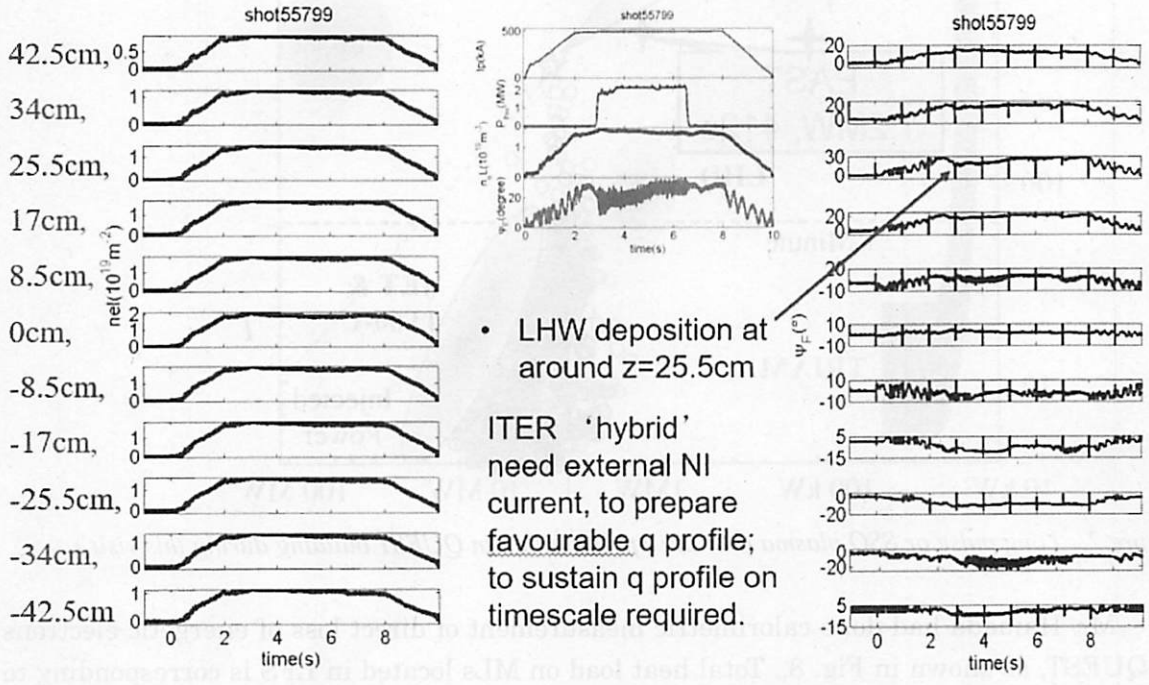

Figure 6 11 Ch.s neL and ψ_F with LHCD phase control (Dr. Liu's presentation in QUEST building during this visit).

Plasma confinement degeneration during long-pulse discharge could be caused by increment of first wall temperature then boundary recycle enhance. So water cooling of PFCs is important to achieve high parameter and long-pulse operation in EAST. The cooling capability strongly depends on the distribution of the heat load to the PFCs, the change of distribution of the heat load strong depends on plasma confinement . Understanding of plasma parameters dependent on distribution of the heat load is in favor of eextrapolating result to ITER. It's certainly worth researching distribution of heat load of PFCs in EAST with steady-state or long-pulse operation. Injected power should be equilibrium with heat load brought by cooling water system. To achieve steady-state or long-pulse operation, it' s important to investigate the power balance. For SSO plasma, recently research status was shown in Fig. 7.. Measurement of heat load and researching of power balance in EAST and QUEST will provide crucial support for ITER experiments.

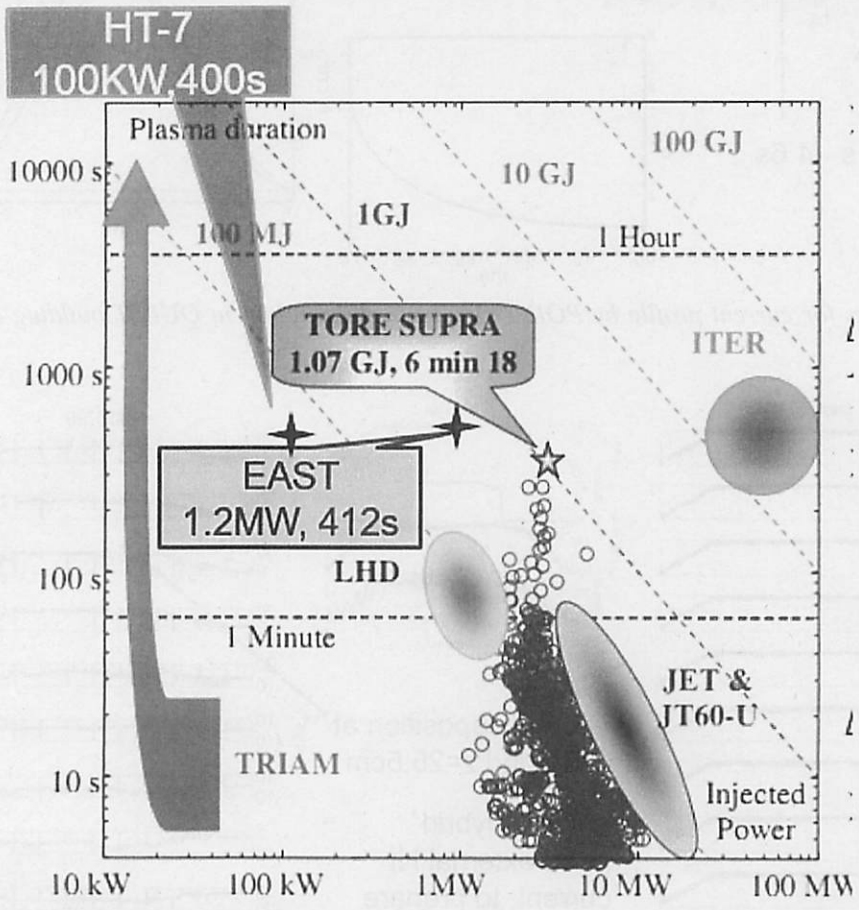

Figure 7 Long pulse or SSO plasma (Mr. Liu's presentation in QUEST building during this visit).

Mr. Hamada had done calorimetric measurement of direct loss of energetic electrons on QUEST, as shown in Fig. 8.. Total heat load on MLs located in LFS is corresponding to 10% (5kW) of the inject RF power (50kW) and approximately constant, selectively heat flows into MLs that is locally protruding plasma side. Additionally, heat load of the MLs is due to the plasma which is strongly dependent on the magnetic field lines structure. Heat load on MLs is not due to the bulk plasma as a result from that the distance between the position of outermost magnetic surface and MLs, greatly accelerated energetic electrons at

the resonant layer by RF injected hits the MLs directly. And visit EAST twice in this year, to study the calorimetric measurement on EAST. After analysis EAST data,as shown in Fig.9, Mr. Hamada think it is impossible to derive an absolute quantity of heat load result from the wall temperature, so it is most important to inquire the Water-Cooling System(control system of the flow rate and water temperature) on EAST. If design and install thermoelectric couple and flowmeter on the water cooling tube, it is possible to measure the Heat Load on EAST. That leads to understand the power balance on EAST eventually. So an initial design was done for EAST, as shown in Fig. 10..

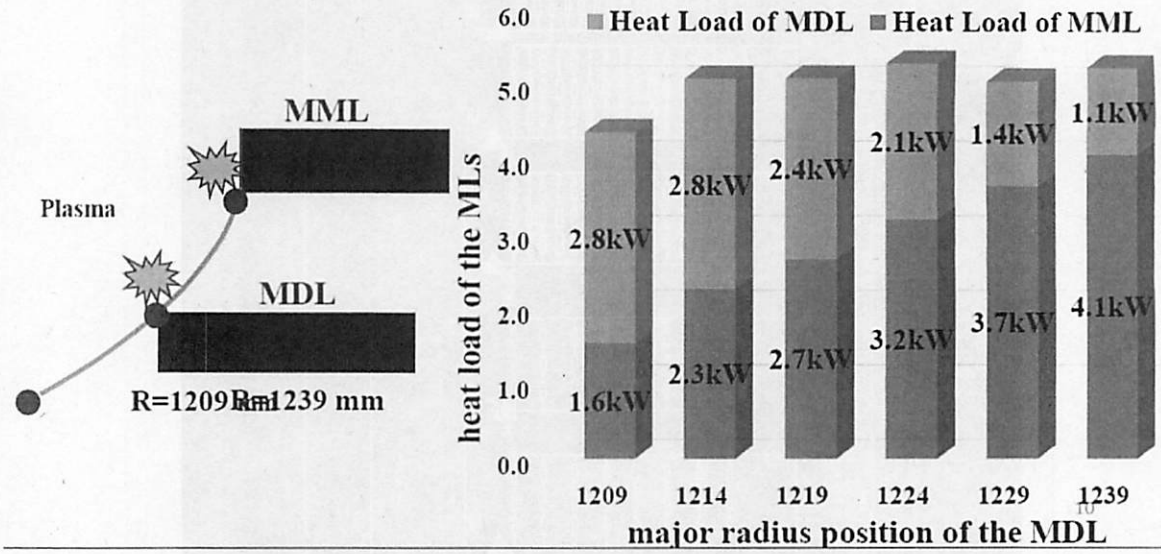

Figure 8 Long pulse or SSO plasma (Mr. Hamada's presentation when he visited in ASIPP).

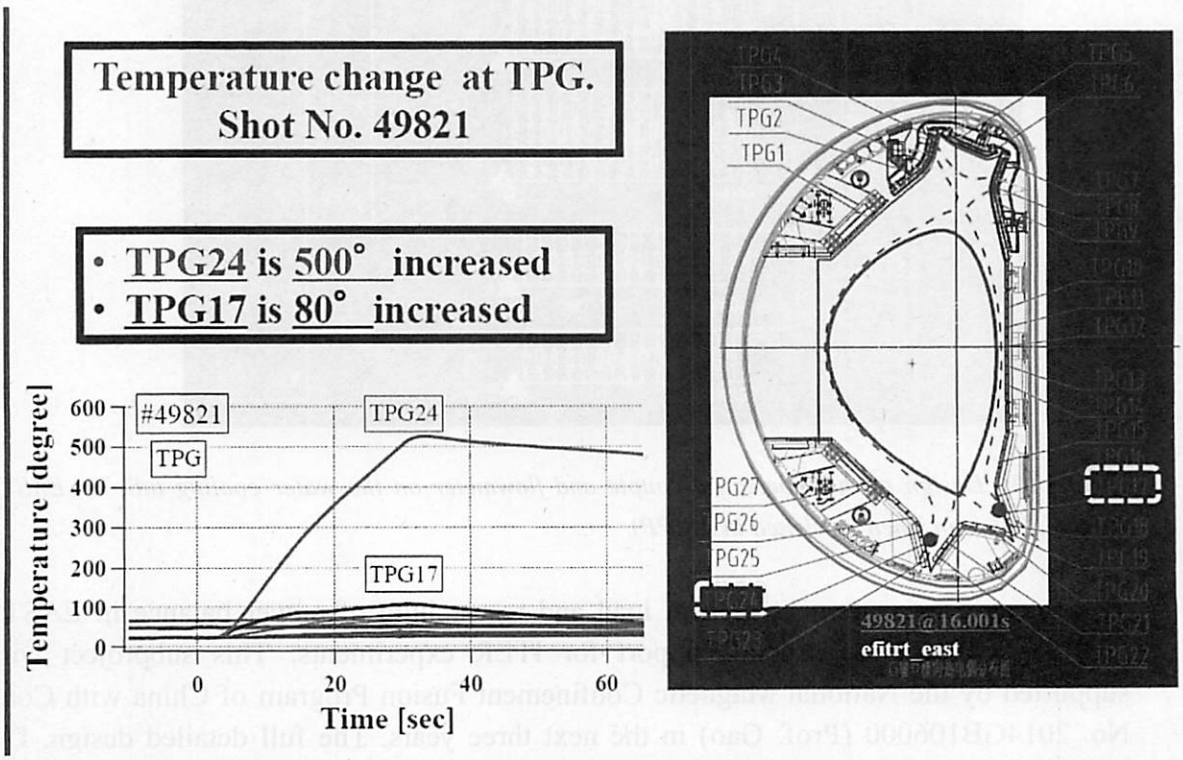

Figure 9 EAST calorimetric measurement data analysis (Mr. Hamada's analysis results when he visited

in ASIPP).

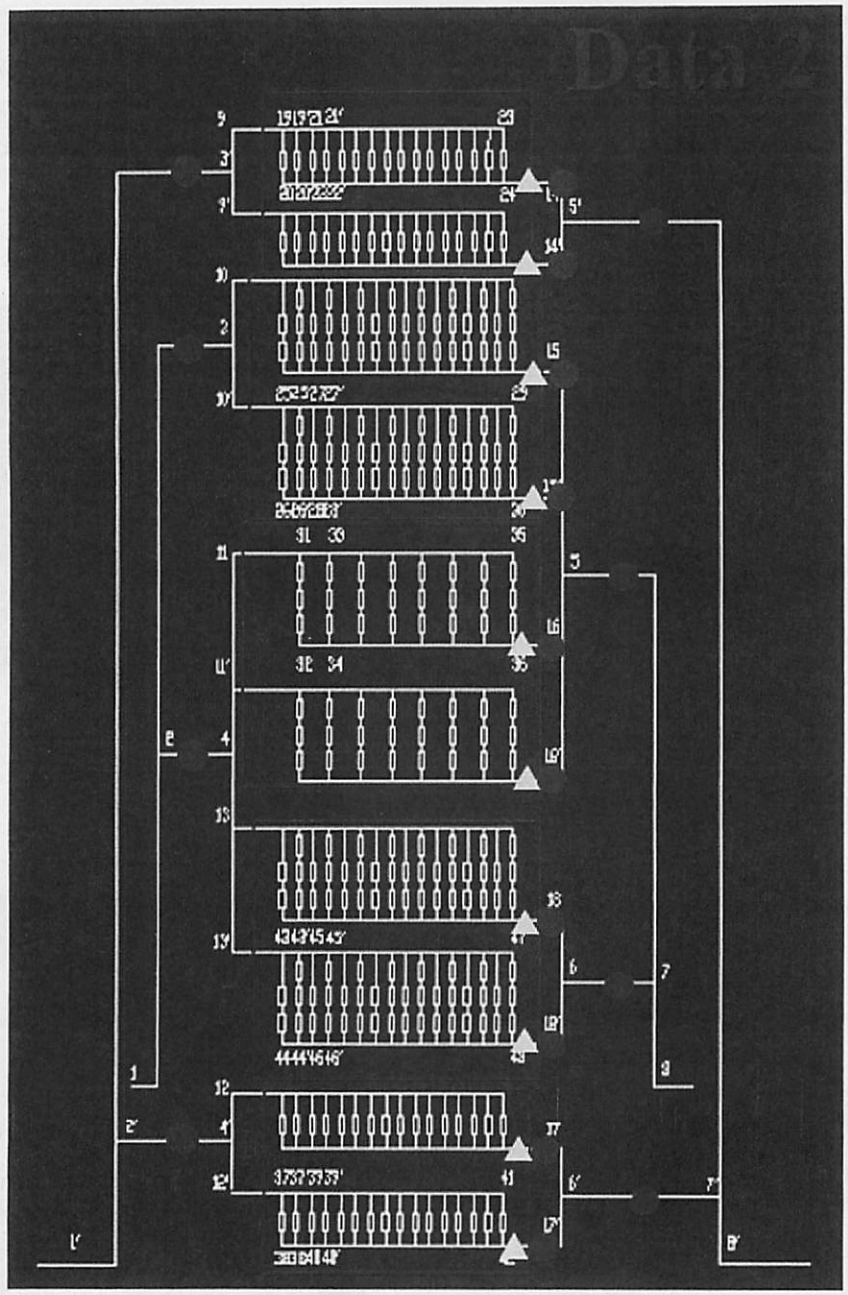

Figure 10 Design of thermoelectric couple and flowmeter on the water cooling tube on EAST (Mr. Hamada's design when he visited in ASIPP).

Because measurement of heat load and researching of power balance in EAST and QUEST will provide crucial support for ITER experiments. This subproject will be supported by the National Magnetic Confinement Fusion Program of China with Contract No. 2014GB106000 (Prof. Gao) in the next three years. The full detailed design, D part construction and installation are being done by Mr. Liu. The research work is going well, as

shown in Figure 11, 12. The joint study of QUEST and EAST will push this subproject forward in the next collaboration.

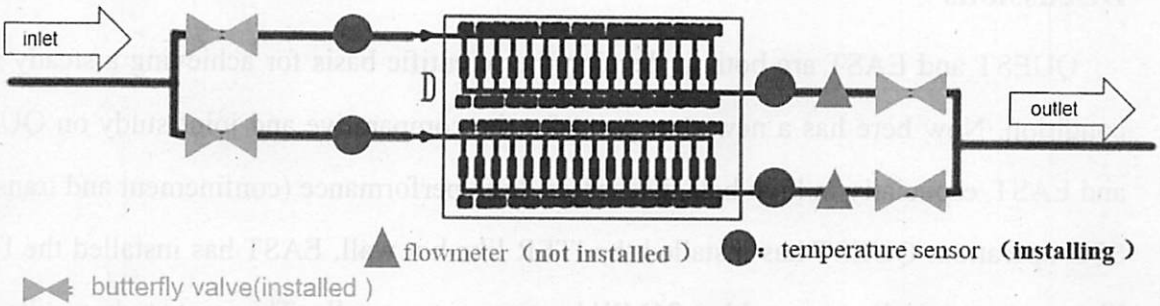

Response time and precision of Platinum resistance(pt100) and thermocouple is different. So install both of them in metallic bellows with experimental form.

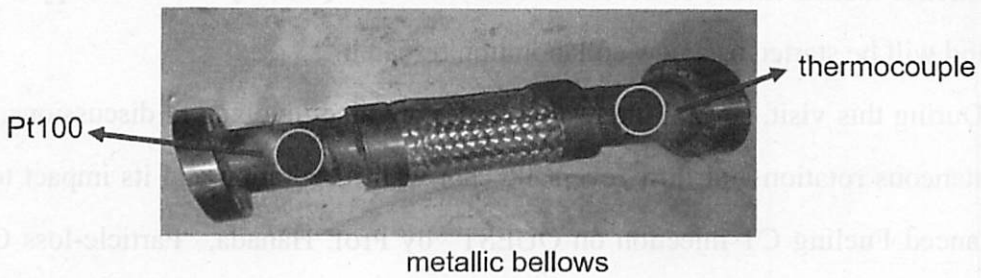

Figure 11 D part detailed design and construction (Mr. Liu's presentation in QUEST building during this visit).

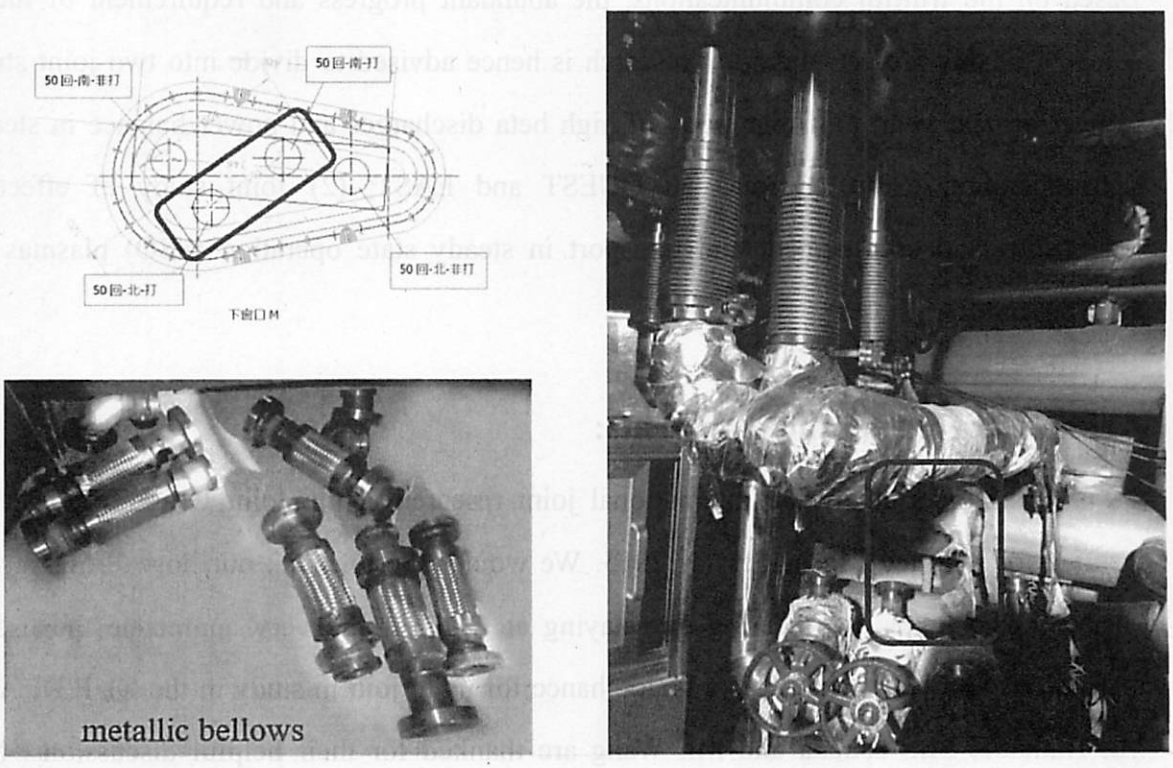

Figure 12 D part construction (Mr. Liu's presentation in QUEST building during this visit).

Discussions

QUEST and EAST are both to develop the scientific basis for achieving a steady state condition. Now here has a new start point for the comparative and joint study on QUEST and EAST, especially in high beta discharges, high performance (confinement and transport) SSO operation. QUEST has installed the ITER like hot wall. EAST has installed the ITER like tungsten top divertor and has 26MW heating power totally. The joint study results now and in future may shed light on the ITER SSO scenario. Also the new joint subproject, calorimetric measurement of heat load in EAST and QUEST, has been supported by two part and will be started as a new collaboration research.

During this visit, several interesting topics are also involved in discussions. Those are "spontaneous rotation and flow reversal", "hot wall installation and its impact to plasma", "Advanced Fueling CT injection on QUEST" by Prof. Hanada, "Particle-loss Control for Making RF-induced Breakdown in QUEST" by Mr. Yoneda, "The study of the colorimetry to measure the deposition thickness on the plasma-facing wall in QUEST" by Mr. Wang. Based on the fruitful communications, the abundant progress and requirement of future research of this project, this joint research is hence advised to divide into two joint study subject in next year: (1) Joint study of high beta discharges and power balance in steady state operation (SSO) plasmas on QUEST and EAST; (2) Joint study of effective diagnostics and confinement and transport in steady state operation (SSO) plasmas on QUEST and EAST.

Acknowledgement and comments:

Work supported by the international joint research at the Joint Usage of Research Centers for Applied Mechanics for 2015. We would like to thank our host, Professor K. Hanada, who helps a lot during our staying at QUEST and very appreciate the useful discussions and comments. It is a good chance for us to join in study in the QUEST. Also Mr. Hamada, Mr. Yoneda and Mr. Wang are thanked for their helpful discussions. Ms.

Funaki, Ms. Kono and Ms. Yamakuchi are thanked for their helps for this visit. We hope that the international joint research at the Joint Usage of Research Centers for Applied Mechanics could continue to enhance China-Japan cooperation on fusion plasma research in the future.

(Signature)_____

(Name in print) Xiang Gao, Yinxian Jie, Haiqing Liu, Yukai Liu

国際化推進共同研究概要

No.7

タイトル: Develop and improve EFIT code of tha plasma equilibrium reconstruction for SSO operation and advanced physical study on QUEST

研究代表者: QIAN, Jinping

所内世話人: 花田 和明

実施期間: 2015 年 11 月 5 日 ～ 11 月 11 日

概要:

国際標準のプラズマ平衡解析コードEFITを用いて、28GHz+8.2GHz の同時入射中に出現する20－30Hzのゆっくりとした振動現象の解析を行った。この解析の結果、振動現象ではプラズマ電流やプラズマ中心の大半径方向位置等の情報を得ることができた。

この放電に関しては、軟X線やQUEST独自のプラズマ平衡解析で 8.2 GHzの基本波共鳴層と最外殻磁気面の位置関係が振動の原因のひとつと考えられており、最外殻磁気面位置の確認が複数の計算コードで確認できたことの意義は大きい。

RESEARCH REPORT

Date Nov. 20 2015

Visiting scientist: (name) Jinping Qian

(position) Associate Professor

(university / institute) Institute of Plasma Physics,
Chinese Academy of Sciences

Host scientist: (name) K. Hanada

(position) Professor

(university / institute) Kyushu University

Research period: (from) Nov. 5, 2015 (to) Nov. 11, 2015

Research subject: **Develop and improve EFIT code of the plasma equilibrium reconstruction for SSO operation and advanced physical study on QUEST**

The visiting started on 6th November 2015, when Mr. Liu gave a presentation to introduce the design, construction and installation of the thermoelectric couple and flowmeter on the EAST water cooling tube. This collaboration is on going well and further experiments will be done on the EAST next campaign, when Hamada san will visit ASIPP for one and a half months.

On the second day, Professor Hanada introduced "the recent progress on non-inductive current drive and particle balance control towards steady-state operation on QUEST". One of the interesting observation is there is the slow oscillation with 20-30Hz in plasma current in 28GHz + 8.2GHz non-inductive plasmas (shown in figure 1). This oscillation can be detected by SXR measurement and is localized around the core plasma. And also this oscillation was observed in the line-integrated density. Then, Prof. Hanada suggested us do the equilibrium analysis on this discharge.

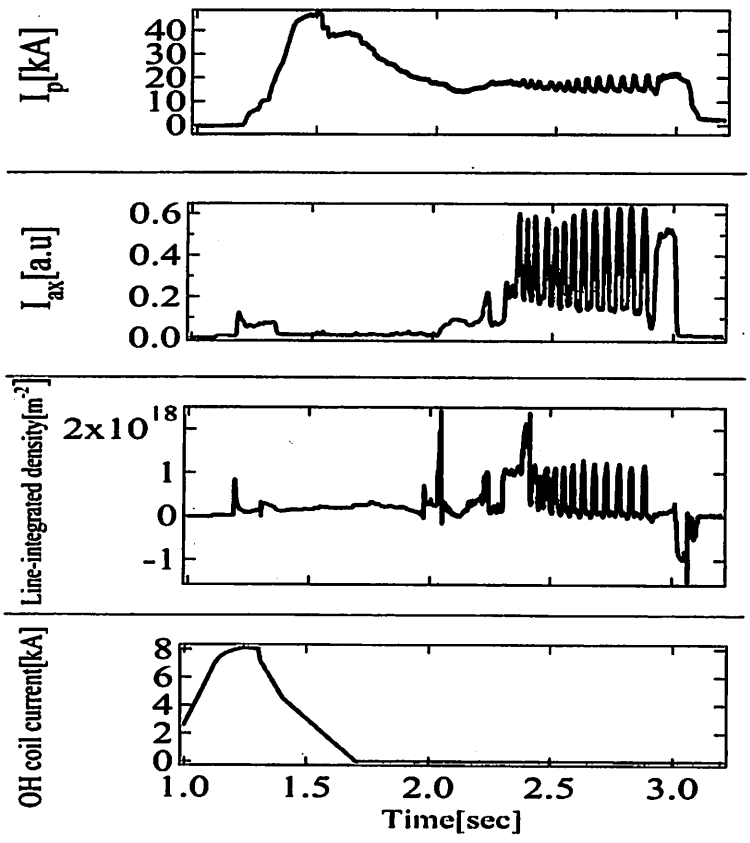

Figure 1 typical waveforms of a slow oscillation from 20~30Hz

After discussion, Mishra and I were heavily involved on the equilibrium analysis of this discharge 22069. Firstly, Mishra helped download all magnetic data which were required by EFIT. Then, at the very beginning, we checked all flux measurements with the vacuum shots to get the error bars. Next, the statistic error bars were used as the inputs for EFIT shown as the fitting weights. Finally, we optimized the flux loop data by switching on and off signal in the input file. The time evolution of plasma current, R &Z position is given in figure 2.

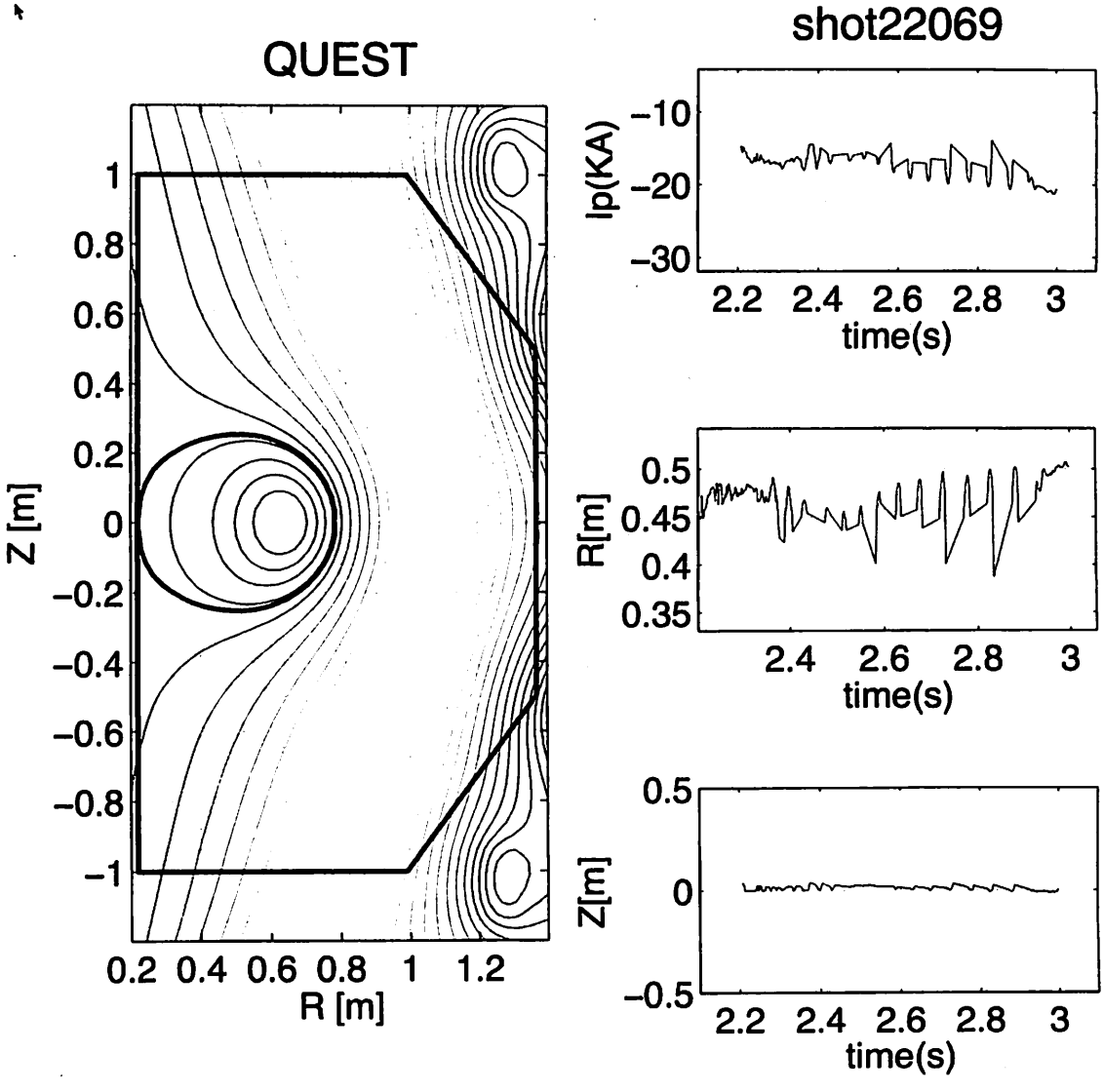

Figure 2 time of evolution of discharge 22069

Obviously, there is oscillation on the plasma current and the R position. The biggest R oscillation is up to10cm, around 30% of the minor radius. Anyway, this looks in agreement with the detection from other diagnostics. Note that more slices, like 5ms, should be done for the further comparison. And the most important thing is, following the different collection of power supply, the mutual inductance prepared by EFUND should be updated. In addition, an interesting thing is, Mishra, as a start began to compile EFIT on another PC. And we discussed a lot how to compile the EFIT for QUEST.

During our stay, Dr. Liu and I gave two presentations, one is initial result of EAST POINT diagnostic and another is scenario development for steady state long pulse operation on EAST. More discussions about further cooperation between EAST and QUEST were hot up.

As a conclusion to this visit, we of the EAST experiment team warmly thank professor Hanada for welcoming us and showing us QUEST activities and very appreciate the useful discussion and comments between EAST and QUEST.

(Signature) J. Qian

(Name in print) Jinping Qian

国際化推進共同研究概要

No.8

タイトル: Investigation of lidar backscattering properties of cirrus clouds for the retrieval of microphysics

研究代表者: BOROVOY, ANATOLY, GEORGIEVICH

所内世話人: 岡本 創

実施期間: 2015年11月13日 ～ 11月23日

概要:
様々な巻雲の氷粒子の形状と衛星ライダの観測条件を考慮して、巻雲のライダ後方散乱光を計算した。物理光学に基づく独自によって、向いあう粒子の面が互いに平行でない場合に対しても散乱計算を実施した結果、通常の六角柱形状の粒子とは異なる散乱特性を得た。
そのため、衛星搭載ライダの解析にも、これらの形状を考慮する必要がある事がわかった。

No. 8. Investigation of lidar backscattering properties of cirrus clouds for the retrieval of microphysics

Institute of Atmospheric Optics, Rus.Acad. Sci., Prof. A.G. Borovoy

Aim:

Aim of the project is to modify and check jointly the algorithms for retrieval of microphysical properties of cirrus clouds based on the synergy use of CPR, lidar ATLID, and multi-spectral radiometer of EarthCARE. These algorithms have been developed by the RIAM team (Okamoto et al., 2010, Sato and Okamoto 2011) where radar signals were calculated by the reliable numerical methods (DDA, FTDT). However, there were no reliable methods to calculate light backscatter by ice crystals of cirrus clouds. Last years the IAO team has just developed such a method called the physical-optics approximation. The numerical results obtained for the lidar ATLID should be included in the retrieval algorithms.

The heads of the teams Prof. H. Okamoto and Prof. A. Borovoi began their joint development of this scientific direction when Prof. A. Borovoi was a visiting researcher in RIAM for 3 months in 2011.

Method:

The problem of light scattering by such large particles as ice crystals of cirrus clouds is a vibrant problem of the atmospheric optics that is just under developing. Here the standard methods for solutions to the exact Maxwell equations prove to be computationally expensive for the ice crystals of cirrus clouds. Some new methods such as Pseudo-spectral time-domain method (PSTD) (Ping Yang at al., 2013) and Invariant embedding T-matrix method (Bi et al., 2014) were suggested but these methods prove to be capable to solve the problem for the ice crystal of sizes up to 20 micrometers for the visible yet while the ice crystal sizes range from a few micron up to millimeter. In particular, in two recent papers 1) Chen Zhou and Ping Yang, "Backscattering peak of ice cloud particles," Opt. Exp. v.23, 11995, 2015 and 2) Jiachen Ding, Ping Yang, Robert E. Holz, Steven Platnick, Kerry G. Meyer, Mark A. Vaughan, Yongxiang Hu, and Michael D. King, "Ice cloud backscatter study and comparison with CALIPSO and MODIS satellite data," Opt. Exp. v. 24, 620, 2016, these leading scientists confirmed that their algorithms are not capable to calculate the light backscattering from cirrus clouds and they needed to use some artificial procedures to guess the backscatter used for interpretation of lidar signals.

The main obstacle for the abovementioned calculations was the large magnitude of the ratio of (particle size/wavelength) that resulted in computationally expensive calculations. However, there is a method that is practically independent of this ratio. This is the physical-optics method. It was begun by Borovoi et al. in 2003 and then it had been improving for last years. In particular, the algorithms of the geometric-optics and physical-optics methods have been opened for free access and the approximations have been discussed in details in three recent papers of 2015: 1) A.V. Konoshonkin, N.V. Kustova, A.G. Borovoi, "Beam-splitting code for light scattering by ice crystal particles within geometric-optics approximation," Journal of Quantitative Spectroscopy & Radiative Transfer v.164, 175–183, 2015; 2) A.V. Konoshonkin, N.V. Kustova, A.G. Borovoi, "Beam splitting algorithm for light scattering by atmospheric ice crystals. Part 1. Theory, " Optika atmosphery i okeana v. 28, 324-330, 2015 (in Russian); 3) A.V. Konoshonkin, N.V. Kustova, A.G. Borovoi, "Beam splitting algorithm for light scattering by atmospheric ice crystals. Part 2. Comparison with the ray tracing algorithm," Optika atmosphery i okeana v. 28, 331-337, 2015 (in Russian).

Simulations in 2015:

The RIAM team developed the lidar-radar algorithm that was applied to both CALIPSO lidar and CloudSat data to retrieve ice microphysics. The algorithm can treat both the nadir pointing CALIPSO period and the 3-degree-off-nadir pointing one. The scattering data bank based on the physical optics methods and calculated by the IOA team was used and the look-up tables for CALIPSO lidar for quasi-horizontally oriented ice plates (Q2D-plate) were created for nadir- and off-nadir lidar pointing periods. However there were several uncertainties in the retrieved ice microphysics. Major source was related to the treatment of ice particle orientation and shape. The sensitivity studies in the retrievals were performed. The optical properties of the quasi-horizontally oriented ice plates (Q2D-plate) calculated by the IOA team for nadir- and off-nadir lidar pointing periods were added to the optical properties of randomly oriented crystals. Though the inclusion of the quasi-horizontally oriented hexagonal ice plates improved the retrieved microphysics of cirrus clouds, some uncertainties still took place.

To overcome this discrepancy, the IOA team has calculated the optical properties of the randomly oriented ice crystals of irregular shapes where the pristine crystal shapes had been distorted. It was shown that this distortion could drastically change the backscatter characteristics like the depolarization ratio, color ratio, and lidar ratio widely used for interpretation of lidar signals. The preliminary results are published in the paper: A. Borovoi, N. Kustova, and A. Konoshonkin, "Interference phenomena at backscattering by ice crystals of cirrus clouds," Opt. Exp. v.23, 24557, 2015.

Results:

We conclude that there is a new important characteristics of the cloud microphysics called the shape imperfectness degree that should be taken into account both in theory and observation data.

During the visit, Prof. A. Borovoi delivered two lectures at the RIAM seminars: "Light scattering by nonspherical particles and its application to atmospheric phenomena" and "Backscatter ratios for ice crystals of cirrus clouds."

Joint publications:

1. Okamoto H., Sato K., Hagihara Y., Ishimoto H., Borovoi A., Konoshonkin A., Kustova N. Evaluation of retrieval algorithms for ice microphysics using CALIPSO /CLOUDSAT and EARTHCARE // 27th International Laser Radar Conference, New York, USA, 5-10 July, 2015.
2. Konoshonkin A.V., Kustova N.V., Borovoi A.G., Ishimoto H., Masuda K., Okamoto H. "Comparison of the physical optics code with the GOIE method and the direct solution of Maxwell equations obtained by FDTD," Proceedings of SPIE. v.9680. CID: 9680 2M. [9680-6], 2015.
3. Konoshonkin A.V., Kustova N.V., Borovoi A.G., Okamoto H. "Coherent and incoherent additions of light beams at solutions of the light scattering problem by use the beam tracing method within the framework of physical optics," Proceedings of SPIE v.9680, CID: 9680 2X. [9680-33], 2015.
4. Konoshonkin A.V., Kustova N.V., Borovoi A.G., Okamoto H., Ishimoto H., Masuda K. "Comparison of the backscattering matrices calculated by the physical-optics method with the exact solution to the Maxwell equations by FDTD method," Izvestija vuzov. Fizika v.58, № 8/2, 184-186, 2015 (in Russian).
5. Konoshonkin A.V., Kustova N.V., Osipov V.A., Borovoi A.G., Masuda K., Ishimoto H., Okamoto H. "The physical-optics method for solving the problem of light scattering by ice crystal particles: comparison of diffraction equations," Optika atmosphery i okeana v.28, 830-843, 2015 (in Russian).

国際化推進共同研究概要

No.9

タイトル: Japan-Korea Oceanography Seminar on Regional Oceanography and Atmospheric Sciences

研究代表者: Shin, Hong-Ryeol

所内世話人: 広瀬 直毅

実施期間: 2016年2月2日 ～ 2月3日

概要:

日韓の領域的な海洋学が進展し、さらに環境問題や大気海洋相互作用まで多岐にわたる研究内容について活発に議論した。

本共同研究の代表者である申教授(公州大学校)と所内世話人である広瀬教授(九大応力研)がコンビーナーとなり、2016年2月2～3日に佐賀県武雄市のホテル春慶屋にて、日韓海洋研究セミナー

“ The 14th Japan-Korea Joint Seminar on Regional Oceanography” を開催した。

Report of the Japan-Korea Joint Seminar on Regional Oceanography

Shin, Hong-Ryeol (Kongjyu National University, Korea)
Hirose, Naoki (RIAM, Kyushu University, Japan)

Aim of this seminar

CREAMS プロジェクトに代表されるように、応用力学研究所は長年、東アジア縁辺海の海洋研究をリードしている。しかし近年、日本海（韓国名：東海）の呼称問題等の政治的影響からか、日韓の共同研究が縮小傾向にあり、特に若手の miscommunication が懸念される。日韓それぞれの海洋学会間においても、呼称問題が足枷となり、協力関係を構築するのが困難な状況である。

そこで東アジア海洋の研究を活発に行っており、地理的にも日韓の接点となる九州大学応用力学研究所が、いわば「日韓海洋学会」の 中核を担うことが期待される。特に対馬海峡の観測データや東アジア縁辺海データ同化モデルの解析値を活用することによって、日韓の領域的な海洋学の発展が望まれ、さらには環境問題や大気海洋相互作用まで波及効果が期待される。

九州大学付近に日本と韓国の海洋学者と若い学生が集い、東アジア縁辺海の研究成果をワークショップで発表することで研究内容の意見交換及び国際交流を増進させることができる。特に若い大学院生を育てる良い機会で、大学院の学生が英語で発表及び質疑応答をすることで国際的な感覚を身に付けることも出来る。

Results

本共同研究の代表者である申教授（公州大学校）と所内世話人である広瀬教授（九大応力研）がコンビーナーとなり、2016 年 2 月 2～3 日に佐賀県武雄市のホテル春慶屋にて、日韓海洋研究セミナー “The 14th Japan-Korea Joint Seminar on Regional Oceanography” を開催した。

全 17 件の講演を、年齢の若い順に発表してもらった。発表リストと発表資料（抜粋）は、添付の通りである。全講演を通じて活発に質疑応答が交わされた。学生の拙い発表の後に、博士研究員や教員がお手本を見せる意図で年齢順にしたが、コンビーナーの狙いとは逆に、発表自体は学生の方が発表練習も積んで英語も流暢という印象を受けた。トップバッターの Ms. Yeonju CHOI（修士課程）からして、堂々たるプレゼンだった。海洋表層混合層の厚さは、その定義方法によって定量的に大きく異なるので、今後は適切な定義方法を探るとのことである。ただし、若者ほど質疑応答には戸惑う傾向にあり、学生（および若手研究者）の英語コミュニケーションの経験機会を提供する当セミナーの存在意義は相変わらずであ

る。

2日目後半には、研究発表を元に、今後の共同研究に関する討議、特にアイデア交換を行った。例えば、Prof. Jae-Hun PARK らによるルソン海峡内部波の非構造格子モデリングは、日本海に通じる三海峡にも応用できる可能性がある。

尹教授と承教授の協力で始まった日韓セミナーも既に 14 回目を迎えたが、相変わらず活気にあふれている。特に今回は韓国側からの参加者が多く、世代交代が進んでいる印象を受けた。残念ながら日本側は学期末で修士論文発表などが控えている時期であり、学生数の低迷も相まって発表者が少なかった。せめてあと 1〜2 週間ほど開催日を遅らせるべきだったかもしれない。

List of the presentation

Yeonju CHOI, Hyejin OK, Yign NOH (Yonsei Univ.)
The Relation between the Subgrid-Scale Variability of Density Profiles and the Mixed Layer Depth

Seongpil GANG, Hong-Ryeol SHIN (Kongju Univ.), Cheol-Ho KIM(KIOST), Naoki HIROSE (Kyushu Univ.)
Effects of surface heat flux over the circulation of the East/Japan Sea

Daehyuk KIM, Hong-Ryeol SHIN (Kongju Univ.)
Long Term Variation of Ocean Heat Content in the East/Japan Sea and the Pacific

Jihoon LEE, Hong-Ryeol SHIN (Kongju Univ.), Tetsutaro TAKIKAWA (National Fisheries Univ.), Naoki HIROSE (RIAM, Kyushu University)
Volume Transport through the Korea Straits Estimated from Seas Level Difference and Current Data

Haejin KIM, Naoki HIROSE, Katsumi TAKAYAMA
Simulation of DO using a physical-biological coupled model

Sang Yeob KIM, Ho Jin LEE, Jae-Hun PARK, Yign NOH and Y. H. KIM
Effect of horizontal resolution on simulation the Subtropical mode water in the North Pacific

Hyejin OK, Yign NOH
How is the OGCM affected by the sensitivity to stratification in the ocean mixed layer model?

Tianran LIU, Bin WANG, Naoki HIROSE
High Resolution Modelling of Kuroshio across the Tokara Strait

Bin WANG, Naoki HIROSE, Dongliang YUAN and Jae-Hong MOON

Effects of tides on the cross-isobath movement of the low-salinity plume in the western Yellow and East China Seas in winter

Eisuke TSUTSUMI, Takeshi MATSUNO (RIAM)

Observations of internal tides and turbulent mixing in a shallow estuary, Ariake Sea

Satoshi NAKADA, Soto SUZUKI, Mitsuru HAYASHI, Shunichi KOSHIMURA, Ei-ichi KOBAYASHI

Simulation of marine sediment resuspension and transport induced by a giant tsunami in Osaka Bay

Tetsutaro TAKIKAWA (National Fisheries Univ.), Akihiko MORIMOTO, Moeto KYUSHIMA, Kaoru ICHIKAWA, Masashi ITO, Kei YUFU

Fortnightly variation of the Tsushima Warm Current on the continental shelf of the southwestern Japan Sea associated with internal tide.

Jae-Hun PARK, Chanhyung JEON and David FARMER

Observation of nonlinear internal waves in the South China Sea using a 2-D array of PIES

Il-Ju MOON, Joon Ho LEE, Ig-Chan PANG

On physical factors that controlled the massive green tide occurrence along the southern coast of the Shandong Peninsula in 2008: A numerical study using a particle-tracking experiment

Chul-hoon HONG, Akira MASUDA, and Naoki HIROSE

Upper Ocean Response to Typhoon, Focusing on "Rightward Bias" Using an Ideal 3D Primitive Equation Numerical Model

Young-Ho SEUNG, S. J. KIM, H. S. KIM, and Y. C. PARK

Some features shown by long-lived surface drifters traveling through the East/Japan Sea and the Northwest Pacific

Tetsuo YANAGI

Development of Coastal Management Method to Realize the Sustainable Coastal Sea

国際化推進共同研究概要

No.10

タイトル: International research collaboration on next generation thermo-electric and high frequency power devices developments

研究代表者: REYNOLDS JR, William, Thomas (Virginia Tech, USA)

所内世話人: 寒川 義裕

実施期間: 2015年 11 月 7 日 ～ 11 月 14 日

概要:

窒化物半導体電子デバイス材料の開発動向を調査し、関連研究成果の発表を行った。以下に概略を述べる。(詳細は別紙参照)本発表では、MOCVD(有機金属気相成長)法により作製した As(ヒ素)添加 GaN(窒化ガリウム)の電子物性について紹介する。まず、これまでに行ってきた P(リン)、In(インジウム)、Al(アルミニウム)添加GaNの電子物性について概観し、As添加GaNとの比較を行う。試料は、GaN低温(550 °C)成長層の上に高温(1030 °C)成長したGaNであり、膜厚は1～4 μm である。成長中の AsH_3 分圧は、全圧100 torrの制限の下で可変とした。As共添加n-GaNのホール測定により電子移動度は最大200～2350 cm^2/Vs と見積もられた。測定温度100～175 Kより高温では電子移動度が低下する傾向が見られた。また、格子欠陥による黄色発光(2.15 eV)の強度が共添加により減少することがわかった。更に、AsとMgの共添加の結果についても報告した。

Electronic properties of GaN doped with arsenic via MOCVD

Louis J. Guido
ECE and MSE Departments, 213 Holden Hall, Virginia Tech, Blacksburg, VA 24061
Email: louis.guido@vt.edu

Group III nitrides can be viewed as "defect semiconductors" in the sense that concentrations of native point defects, residual impurities, and threading dislocations often approach those of intentional dopants. This talk explores the extent to which isovalent doping can mitigate the impact of such defects on the electronic properties of GaN. Previous work on GaN thin films doped with P [1], As [2], In [3] or Al [4] will be reviewed briefly in order to place into context findings reported herein on As-doped GaN. Samples were prepared by OMVPE using TMGa, NH_3, AsH_3, SiH_4 and Cp_2Mg as precursors, and H_2 as the carrier gas. A 25 nm GaN nucleation layer was deposited at 550 °C followed by 1 to 4 μm of uniformly doped GaN grown at 1030 °C. The AsH_3 pressure was varied over a wide range with the reactor pressure held constant at 100 torr. In n-type GaN co-doped with As, Hall measurements suggest a reduction in electronic compensation with the addition of AsH_3 to the growth ambient. Peak electron moblility increases from 200 to 2350 cm^2/Vs and the temperature at which the mobility reaches its maximum value decreases from 175 to 100 K (see Fig. 1). In addition, the defect-mediated yellow-band (2.15 eV) transition increases with Si doping; however, co-doping with Si plus As causes a precipitous drop in its integrated intensity. In the case of Mg-doped GaN, the most interesting trend with the addition of AsH_3 to the growth ambient is a coupling between Mg concentration and As solubility. At the highest Mg doping level, the As content is 100x larger than that found in material grown without Cp_2Mg at the same AsH_3 pressure. Theoretical work suggests that As incorporates on Ga sites in p-type GaN forming double-donor antisite defects thereby making it difficult to synthesize p-type material [5]. Notwithstanding this prediction, Hall measurements on GaN:Mg+As yield hole density and mobility values comparable to those found in conventional GaN:Mg (see Fig. 2). These experimental findings will be discussed within the context of different physical models with particular consideration given to the possibility that arsenic influences the native defect chemistry of gallium nitride.

[1] T. Ogino and M. Aoki, Jpn. J. Appl. Phys. **18**, 1049 (1979).
[2] L. J. Guido, P. Mitev, M. Gherasimova, and B. Gaffey, Appl. Phys. Lett. **72**, 2005 (1998).
[3] S. Yamaguchi, M. Kariya, S. Nitta, H. Amano, and I. Akasaki, Appl. Phys. Lett. **75**, 4106 (1999).
[4] J-K. Jeong, J-H. Choi, C-S. Hwang, H-J. Kim, and J-H. Lee, Appl. Phys. Lett. **84**, 2575 (2004).
[5] C. G. Van de Walle and J. Neugebauer, Appl. Phys. Lett. **76**, 1009 (2000).

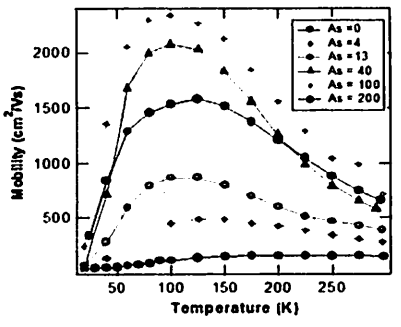

Fig. 1. Variable-temperature Hall data for n-type GaN doped with arsenic. Inset: AsH_3 flows in sccm.

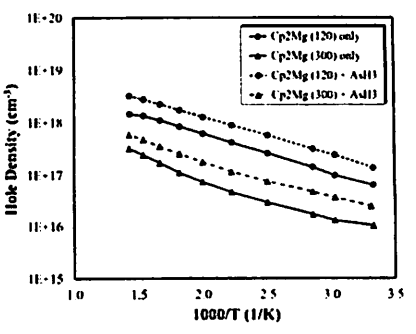

Fig. 2. Variable-temperature Hall data for p-type GaN films doped with Mg or Mg+As. Inset: Cp_2Mg and AsH_3 flows in sccm.

国際化推進共同研究概要

No.11

タ イ ト ル: CFD Prediction of unsteady aerodynamic and hydrodynamic performances of floating offshore wind turbine

研究代表者: WAN, Decheng

所内世話人: 胡 長洪

実 施 期 間: 2015 年 11 月 29 日 ～ 12 月 9 日

概要:

今年度の国際化推進共同研究「CFD prediction of unsteady aerodynamic and hydrodynamic performances of floating offshore wind turbine」に関して，共同研究・研究集会とも予定通り実施した。共同研究成果について，2 編の国際学会論文を投稿し採択された。研究集会について，世話人が担当した特定研究の研究集会と共同開催で，外国から9名，日本から約30 名の参加者があり，海洋再生可能エネルギー開発に関する有意義な国際研究集会となった。

Report for 2015 RIAM International Joint Research Project

CFD prediction of unsteady aerodynamic and hydrodynamic performances of floating offshore wind turbine

Purpose

The project aims to integrate the work already carried out at SJTU in the field of CFD simulation of offshore floating wind turbine flows with the work performed at RIAM in the area of offshore renewable energy. The successful complement of this project will provide (a) a useful database to other relevant people in the field of offshore floating wind turbine for calibrations, validations & comparisons; (b) an integrated simulation with experimental tool to better understand the hydrodynamic and aerodynamic behavior of offshore floating wind turbine. The joint research will further this state-of-the-art scientific knowledge in a broad range of offshore engineering application. In addition the project contributes to the technical training of graduate students and prepares them to be active participants in the multi/inter-disciplinary workforce of the future.

Research Plan

(1) Carry out collaborative research between SJTU and RIAM, in the area of advanced modeling of unsteady hydrodynamic and aerodynamic forces interacting on offshore floating wind turbine, to provide a benchmark for validation and comparison of various analytical, simulation and experimental models on the study of the floating offshore wind turbine problem.

(2) Evaluate the system's responses of 6DOF motions, which are excited by both wave and wind under various conditions as well as the rotation of blades.

The members involved in this collaborative research are shown in the following table.

Researcher's Name	Name of University or Institute	Present Status or Grade (graduate students)	Researcher role
Decheng Wan	SJTU	Professor	Representative person (CFD)
Ping Cheng	SJTU	PhD student	Co-researcher (CFD)
Jianhua Wang	SJTU	PhD student	Co-researcher (CFD)
Pengfei Li	SJTU	Master student	Co-researcher (CFD)
Makoto Sueyoshi	RIAM	Assistant professor	Co-researcher (experiment)
Cheng Liu	RIAM	Posdoc	Co-researcher (CFD)
Changhong Hu	RIAM	Professor	RIAM Attendant
Decheng Wan	SJTU	Professor	Representative person (CFD)

Summary of Collaboration Research

In 2015, an unsteady actuator line model (UALM) has been developed and applied to a 5MW floating offshore wind turbine (FOWT). This model is implemented into two-phase fluid CFD solver, naoeFOAMSJTU. The goal of this study is to investigate the interaction of the aerodynamic loads and the platform motion within acceptable time cost. A semi-submerged floating platform conceptualized in the Offshore Code Comparison Collaboration (OC4) has been considered. Two kinds of full-system simulations with different complexity have been performed. First, the wind forces are simplified into a constant thrust; second, the fully coupled dynamic analysis with wind and wave excitation is conducted by utilizing the UALM. The UALM was verified first by comparison with previous study. Based on the results, the aerodynamic loads and coupled responses for cases of different complexity have been discussed.

Publications related to this joint research project are as follows.

1) Ping Cheng, Decheng Wan and Changhong Hu, Unsteady Aerodynamic Simulations of Floating Offshore Wind Turbines with Overset Grid Technology, Submitted to Twenty-sixth (2016) International Offshore and Polar Engineering Conference, Rhodes(Rodos), Greece, June 26–July 2, 2016. (Accepted)

2) Pengfei Li, Decheng Wan and Changhong Hu, Fully Coupled Dynamic Response of a Semi-submerged Floating Wind Turbine System in Wind and Waves, Submitted to Twenty-sixth (2016) International Offshore and Polar Engineering Conference, Rhodes(Rodos), Greece, June 26–July 2, 2016. (Accepted)

As an important event of this international joint research project, a workshop was held on December 7-8, 2015. The work shop, 'International RIAM Symposium on Ocean Renewable Energy Technologies and Related Fluid Dynamics Researches', was co-organized by another RIAM joint research project, 'RIAM Research Workshop of Designated Joint Research Project on Development of Floating Marine Renewable Energy Systems'.

The research budget provided for this international joint research has been used to support travel expenses of the following 3 scholars to the workshop.

1. Decheng Wan, Professor of Shanghai Jiao Tong University, China
2. Zhiqiang Hu, Associate Professor of Shanghai Jiao Tong University, China
3. Kangping Liao, Associate Professor of Harbin Engineering University, China

On the workshop, these invited scholars have presented their recent researches on ocean renewable energy development, and have discussed with participates from Japan and other countries. The program of the workshop is as follows.

PROGRAM

Date: December 7-8, 2015
Place: W601, RIAM, Kyushu University

7 December (Monday)

13:00 - 13:10	*Opening Address*
	Changhong Hu (RIAM, Kyushu University)
13:10 - 13:50	*Keynote Lecture*
	Observation and Experiment of Bio-Fouling Effects on Tidal Power Generators
	Yusaku Kyozuka (Kyushu University)
13:50 - 14:20	*Invited Lecture*
	Tidal Stream Measurements for the Water off the Cape Fuguei for a Potential Power Generation Site
	Cheng-Han Tsai (National Taiwan Ocean University, Taiwan, R.O.C.)
14:20 - 14:50	*Invited Lecture*
	Duct Application to Tidal Current Energy Power Convertor
	Chul H. Jo (Inha University, Korea)
14:50 - 15:00	Coffee break
15:00 - 15:30	**Numerical Investigation of Coupled Floating Offshore Wind Turbine System in Wind and Waves**
	Decheng Wan (Shanghai Jiao Tong University, China)
15:30 - 16:00	**Model Test Research on Spar-Type Floating Wind Turbine**
	Zhiqiang Hu (Shanghai Jiao Tong University, China)
16:00 - 16:30	**Hydrodynamic Performance of the FOWT-WEC Coupling System**
	Kangping Liao (Harbin Engineering University, China)
16:30 - 17:00	**CFD Simulation of a Tidal Current Farm**
	Cheng Liu, Changhong Hu (Kyushu University)
17:00 - 17:30	**Time-Domain Calculation of Hydrodynamic Forces on a Floating Platform of Complex Geometry for Renewable Energy Utilization**
	Yuichi Ashida, Masashi Kashiwagi (Osaka University)
17:30 - 18:00	**Utilization of Hydrofoil to Improve Propulsive and Seakeeping Performance of a Ship**
	Hiroshi Isshiki (Inst. of Mathematical Analysis)

8 December (Tuesday)

9:30 - 10:00	*Invited Lecture*
	Development of Wind Energy Systems and Future Trends
	Peter Jamieson (University of Strathclyde, UK)
10:00 - 10:30	*Invited Lecture*
	Retrospect and Development of Classical Rotor Theories in Context of Making Torque from Wind
	Valery Okulov (Technical University of Denmark, DK)
10:30 - 11:00	**Power Augmentation Methods for the Wind Solar Tower**
	Tomo Nagai (Kyushu University)
11:00 - 11:30	**Performance of Clustered Diffuser Augmented Wind Turbines**
	Uli Goeltenbott (Kyushu University)
11:30 - 13:00	Lunch
13:00 - 13:30	**Development of an Ocean-Current Turbine at OIST**
	Katsutoshi Shirasawa, Junichiro Minami,Tsumoru Shintake (Okinawa Institute of Science and Technology), Hidetsugu Iwashita (Hiroshima University)
13:30 - 14:00	**Hydro-VENUS: Pendulum-Based Tidal Energy Converter**
	Shinji Hiejima (Okayama University)
14:00 - 14:30	**Observation and Numerical Simulation of Tidal Current around Amami-Oshima in Relation to Tidal Power Generation**
	Ritsuki Kunisato (Sanyo Techno Marine), Tohru Yamashiro (Kagoshima University)
14:30 - 15:00	**Currect Influence on Hydrodynamics and Motions of FOWT in Waves**
	Yasushi Higo, Hidetsugu Iwashita, Kyohei Kajino, Akihide Koya (Hiroshima University)
15:00 - 15:30	**Research on Structural Analysis of a Floating Structure Equipped with Wind-Lens Turbines using Shell Element**
	Yoshikazu Tanaka (Hiroshima University)
15:30 - 16:00	**Initial Structural Design of a Triangular Floating Structure with Three Wind-Lens Turbines**
	Yukitaka Yasuzawa, Shunsuke Otsubo (Kyushu University)
16:00 - 16:10	*Closing Remarks*
	Hidetsugu Iwashita (Hiroshima University)

国際化推進共同研究概要

No.12

タ イ ト ル: Cold Crucible Czochralski(3CZ)

研究代表者: ZAIDAT, Kader

所内世話人: 柿本 浩一

実 施 期 間: 2015 年 10 月 23 日 ～ 10 月 29 日

概要:

シリコンの結晶の純度向上のために、フランス SIMP・グルノーブル大学の Kader 先生との共同研究を開始した。実際には、結晶成長の一種であるスカルメルテイング法を用いて、高純度結晶を成長させる予定であるが、融液の対流の不安定性が結晶成長に悪影響を与える可能性がある。この悪影響を除去するために、九大は結晶成長中の炉内の気相中の不純物濃度を低減させることを提言している。今後この方法の発展のために共同研究を推進する。

Proposal title : Cold Crucible Czochralski

Acronym: 3CZ

Scientific partners: SiMaP France/ RIAM Japan

Context

High added value and innovative semiconductors and oxides are elaborated from methods like Czochralski, Bridgman or floating zone. These techniques are widespread for silicon or sapphire crystallization for instance but they generally suffer from the very same disadvantage: the presence of a hot and consumable crucible. In order to improve and optimize industrial processes, weaknesses of using disposable containers should be addressed:

□ Economic impact: high purity silica crucible used for silicon crystallization. As silica containers can only be used once, due to irreversible damages associated to cristobalite (□α to β) phase change transitions, they severely impact the cost of the devices and equipment derived from the crystals, such as PV cells, scintillators, lasers, etc.. Likewise noble and refractory metal containers used for oxide processing have a strong impact not only on the final cost but also on the reliability of the process.

□ Contamination effect: a contamination of Si by iron, aluminum, oxygen, nitrogen and/or carbon, of sapphire by Mo or C, that are major constituents of the crucible and of the coating is unavoidable with today crystallization techniques. Often these impurities precipitate and destroy the single crystallinity and the electrical properties in the Si case of the final product.

□ Environmental and cycle of life issues: contaminated parts of ingots - besides the cost of the raw material - should be discarded to fulfill industrial requirements. Recycling this type of polluted materials can be tricky and costly. Most often recycling consists in using them in lower value applications, which is detrimental for the financial yield. Furthermore, the matter coming from used crucible can hardly be recycled.

Expected benefits

Regarding C, contamination will also come from the furnace parts, since it is widely used for resistors, susceptors and insulating graphite felts. The content of light elements in Si is determined by exchanges between these components and Si either by direct contact or through the furnace atmosphere. Precipitates of SiC or Si_3N_4 in the liquid or at the crystallization interface can occur. Depending on their size and concentration such precipitates can cause problems during the wafering step, induce a degraded crystallization microstructure, or constitute electrical shunts at the p-n junction of PV cells. In the case of oxygen it is even necessary to avoid the formation of the "boron- oxygen" (BO) complexes which are responsible for the light-induced degradation (LID) of the carrier lifetime and the solar cell efficiency[1]. For a given doping level, reducing oxygen contamination is currently the best way to control this type of degradation especially that the achieved record cell efficiency (> 22%) are mainly accomplished using oxygen free Fz wafers. In addition, in microelectronics, oxygen raises structural problems with oxygen induced stacking faults and the precipitation at vacancies defects. Oxygen contamination appears as a strong limitation of silicon wafers performance. Although ultra-pure silicon and gases are employed, the silica crucible remains a permanent

source of oxygen that cannot be avoided with theses classical processes and should be mastered in order to allow a major breakthrough in silicon wafers performance.

Likewise, sapphire ingots face problems due to the presence of molybdenum or tungsten: in presence of oxygen traces, metallic crucibles enhance carbon transport and thus pollution of the alumina bath (micro bubbles). Platinum acts as a detrimental substitutive element for superconducting oxides[2]. Conductive and optical properties are dramatically decreased due to non- controlled contaminations. Quite often pulling oxide single crystal from the melt under stationary stable regime remains complex. Attempts have been made to scale up the Czochralski and Bridgman processes to grow large boules but the inherent properties of oxide crystals make them difficult to produce with a high enough defect-free optical quality. Hot crucible is possible to be damaged during the process. So by using cold crucible (3Cz), it is a good way for charge container security. The main challenge in this project is in the improvement of large size and controlled high quality crystals by improving the crystal growth process through the usage of re_usable cold crucible in order to reduce the defects density.

3CZ ambition

Replacing hot and polluting containers by cold crucibles provides a major breakthrough in the processing of advanced materials. Intrinsic assets of cold crucible are of first interest to crystallize single crystals: as the crucible wall remains at a temperature close to room temperature very little contamination can be expected from the container. Eventually a solid skull will be formed between the molten material and the wall providing an efficient diffusion barrier. As a consequence contamination of the melt from the crucible can be dramatically reduced, ensuring an efficient way to produce very pure crystals with a high material throughput and good mechanical properties. Given a proper maintenance a cold crucible can be re-usable on a very long term, providing both reliability and significantly reduced waste matter for crucibles.

In current hot crucibles, even under induction heating the electromagnetic stirring is generally weak due to the screening effect. Homogeneity of the molten bath can hardly be enhanced, which is detrimental for doping homogeneity of pulled crystals. In contrast, with cold crucibles, the composition homogeneity of the molten bath should benefits from the efficient and adjustable electromagnetic stirring due to induction coupling, even in the case of oxides that are electric conductors in the liquid state. Thanks to the stirring, lower grade materials should eventually be employed to grow crystals, addressing cheaper and less restrictive raw materials. As doping level is of prime importance for electrical and optical properties, doping homogeneity is a strong requirement, yet tough to fulfill, playing on the mater throughput of a process. 3CZ method is a particular asset for high efficiency n-type silicon crystallization and has a strong potential for high material productivity.

3CZ scientific and technological challenges

Very interesting scientific and technological challenges rise from the use of cold crucibles in the purpose to grow single crystals, especially to tune electromagnetic system for crystal pulling: temperature gradients, stirring, and shape of the interface have to be controlled while ensuring stability. So far, single crystal pulling from a cold crucible appears to have been poorly investigated. Only very little literature[1], mainly addressed to silicon crystallization[3-4], is dedicated to this particular growth process. However the feasibility of pulling a dislocation free single crystal was demonstrated, though on a small laboratory scale (60g of molten silicon, 15mm in diameter for the grown ingot). To go further, in this project:

□ Advanced numerical modeling will be used to investigate temperature gradients, interface shape and doping homogeneity and eventually growth instabilities; □

□ Crystallization of selected model materials (silicon, sapphire) is planned to be investigated from an experimental point of view with a strong coupling with structural characterizations and numerical modeling; □

□ From a technical point of view the low electrical conductivity for oxides and semiconductors at room temperature generally deprives from direct coupling. Alternative ways of pre- heating have to be implemented (frequency adaptation, pre-heater...) in order to achieve the melting; □

□ Industrialization is planned to be addressed by evaluating the capacity of adaptation of several industrial solutions for this purpose, as well as cost evaluation and an anticipation of industrial needs or requirements. Comparison between regularly grown CZ crystals with cold crucible grown crystals is eventually planned to assess the quality of the processed ingots and feasibility of using lower grade raw material will also be evaluated.The processing of high performance materials needed for semiconductors, photovoltaic and optics suffers from a chronic disadvantage due to the presence of polluting, costly and hardly recycled containers. Suppressing this major drawback should allow providing better material at constant cost or, based on lower grade raw materials, cheaper material with equivalent quality. From this point of view implementing cold crucibles in such processes should provide industrial levers to dramatically reduce downgraded or discarded raw materials suppress wastes due to partial crucible recycling and improve final performance as well as process reliability. Particular concerns rose recently from civil society about improving and strengthening industrial competitiveness while lowering environmental impact of industrial processes, especially for raw materials wasting and energy consumption. Suppressing costly consumables not only is an efficient way to optimize processes but to dramatically improve the competitiveness. This is a relevant way to give back a powerful lever to industry in the field of advanced materials for electronics, photovoltaics and optics. □

3CZ scientific consortium

The ambition of the project 3CZ is to join the efforts of two groups acting in the field of materials science from liquid phase, in order to address and solve both scientific and technical issues raised by□single crystal growth from a cold crucible. Expertise in electromagnetic processes and numerical modeling are provided by SIMaP. Expertise in silicon single crystal growth and numerical modeling are provided by RIAM. The complementarity of the gathered competences between these two partners is a strong asset to conduct successfully the 3CZ project.

References:

[1] Schutz-Kuchly, T.; Veirman, J.; Dubois, S.; Heslinga, D. R., Light-Induced-Degradation effects in boron–phosphorus compensated n-type Czochralski silicon, Applied Physics Letters, vol.96, no.9, pp.093505,093505-3, Mar 2010□

[2] Bletskan, Determining residual impurities in sapphire by means of electron paramagnetic resonance and nuclear activation analysis, Technical Physics Letters 34(7),612-614, 2008 □

[3] Ciszek, Some applications of cold crucible technology for silicon photovoltaic material preparation, Journal of the Electrochemical Society 132(4), 963-968, 1985

[4] Ciszek, Growth and Properties of (100) and (111) dislocation free silicon crystals from a cold crucible, Journal of Crystal Growth 70, 324-329, 1984 □

国際化推進共同研究概要

No.13

タ イ ト ル: Thermodynamics and crystal growth of GaN

研究代表者: GRZEGORY, IZABELLA, ALICJA
(Institute of High Pressure Physics of the Polish Academy of Sciences, Poland)

所内世話人: 寒川 義裕

実 施 期 間: 2015 年 10 月 31 日 ～ 11 月 20 日

概要:
窒化物半導体バルク成長および窒化物半導体光学素子の開発動向について調査し、関連研究成果の発表を行った。本発表では、窒化物半導体のバルク成長に関する研究動向および窒化物半導体の短周期超格子の物理と成長に関する報告を行った。バルク成長に関しては、HVPE 法による GaN の高指数ファセット面成長について報告した。光学素子開発に関しては、バンドギャップ・エンジニアリングにおいて興味深い材料構造である *m*InN/*n*GaN、*m*GaN/*n*AlGaN、*n*GaN/*m*AlInN(*m*、*n* は原子層数 数層)を例に最近の研究動向を報告した。(詳細は別添え資料参照)本材料では、ピエゾ分極などにより導入される電場を利用してバンドギャプエネルギーを制御可能である。発表の前半では、内部電場などが波動関数の混成に与える影響を紹介した。後半では、GaN/AlGaN および GaN/AlInN などの短周期超格子の成長について紹介した。TEM などによる構造解析の結果、InN/GaN 超格子は、実際には $In_xGa_{1-x}N$/GaN($0.2 < x < 0.33$)となっていることがわかった。これは InN と GaN の大きな格子不整合に起因する。最後に、In 組成を増加させるアイデアについて提言した。

Short Period Superlattices of Nitride Semiconductors. Interesting physics, difficult realization

Tadek Suski

Institute of High Pressures Physics, UNIPRESS, 01-142 Warsaw, Poland

Fabrication of short-period *m*InN/*n*GaN, *m*GaN/*n*AlGaN, and *n*GaN/*m*AlInN superlattices (SPSLs) consisting of small numbers of monolayers (MLs) *m* and *n*, is one possible way to perform *band gap engineering* in the wide range of spectrum, from deep ultraviolet to infrared. Beside of various potential applications an interesting physics motivated many groups to calculate electronic structure of such compounds. Presence of built-in electric field due to spontaneous and piezoelectric polarizations make possible to tune significantly band gap of the considered structures inducing even the band gap closing. In the first part of the seminar I will concentrate on illustration of these effects taking into account hybridization of the wave functions of the quantum wells and barriers, built-in electric field and lattice mismatch. Bond length modifications, asymmetry of charge distribution and magnitude of internal electric field obtained from *ab-initio* calculations will be presented.

In the second part of the Seminar, I will concentrate on epitaxial attempts to grow these short period superlattices. In case of GaN/AlGaN, and GaN/AlInN SPSLs theoretical predictions of band gaps and optical studies of luminescence seem to agree. Whereas large discrepancies between theoretical calculations and experiment have been reported for *m*InN/*n*GaN. Important difficulties in obtaining *m*InN/*n*GaN were pointed out two years ago. Detailed transmission electric microscopy studies have revealed that instead of structures consisting of InN/GaN superlattices the $In_xGa_{1-x}N$/GaN ones (with x between 0.2 and 0.33) have been achieved. It is very likely that large lattice mismatch and differences in decomposition temperatures of GaN and InN are responsible for the observed effects. Ideas applied to make an increase of the In amount in InGaN/GaN SPSLs will be discussed in the final part of the seminar.

国際化推進共同研究概要

No.14

タイトル: Mechanical properties of laminated CFRP composites under and after impact loadings

研究代表者: CHEN, Dingding

所内世話人: 新川 和夫

実施期間: 2015 年 12 月 14 日 ～ 12 月 18 日

概要:
今年度の共同研究では衝撃を受けた複合材料の力学特性評価を行った。種々の異なる積層構成の複合材料の実験をホプキンソン棒試験および衝撃引張り試験により強度評価を行い、実験結果より、耐衝撃性の高い積層構成を提案した。

World Academy of Science, Engineering and Technology
International Journal of Chemical, Molecular, Nuclear, Materials and Metallurgical Engineering Vol:9, No:9, 2015

Novel CFRP Adhesive Joints and Structures for Offshore Application

M. R. Abusrea, Shiyi Jiang, Dingding Chen, Kazuo Arakawa

Abstract—Novel wind-lens turbine designs can augment power output. Vacuum-Assisted Resin Transfer Molding (VARTM) is used to form large and complex structures from a Carbon Fiber Reinforced Polymer (CFRP) composite. Typically, wind-lens turbine structures are fabricated in segments, and then bonded to form the final structure. This paper introduces five new adhesive joints, divided into two groups: one is constructed between dry carbon and CFRP fabrics, and the other is constructed with two dry carbon fibers. All joints and CFRP fabrics were made in our laboratory using VARTM manufacturing techniques. Specimens were prepared for tensile testing to measure joint performance. The results showed that the second group of joints achieved a higher tensile strength than the first group. On the other hand, the tensile fracture behavior of the two groups showed the same pattern of crack originating near the joint ends followed by crack propagation until fracture.

Keywords—Adhesive joints, CFRP, VARTM, resin transfer molding.

I. Introduction

COMPOSITE materials have high stiffness-to-weight and strength-to-weight ratios, and have been used for many applications including aerospace, automotive, and wind turbine structures [1], [2]. The wind-lens, a curved ring around the turbine blades, is manufactured from six identical parts joined together to form the final structure. Consequently, its performance depends not only on material properties but also on the joining technique. As such, structural integrity depends critically on the efficiency of this technique. Composite structure connections depend on many factors such as size, design, available technology, and logistical limitations [3], [10]. Therefore, the performance and failure modes of different joint types, including composite-to-composite [4]–[6] and composite-to-other materials [7]–[9], have been extensively studied both numerically and experimentally.

Bonded joints have mechanical advantages over bolted joints because fibers are not cut, and stresses are transmitted more homogenously. However, the strength and durability of bonded joints strongly depend on various factors such as surface preparation, joint-end configuration, fiber angles, overlap length, and process parameters [10], [11]. Because the interface is usually, the weakest part of a structure, most reported methods have aimed to improve the strength of the adhesive or adhesive–composite interface. However, if the adhesive or adhesive–composite interface can be avoided altogether, the strength could be further improved.

This paper introduces various adhesive bonded joints, made of Carbon Fiber Reinforced Polymer (CFRP), for use in offshore wind-lens structures. The main objective of this work was to develop high-strength joint applicable to offshore wind-lens structures. The strengths of five joints were assessed. All joints and CFRP material tested in this study were made using a technique developed from the Vacuum-Assisted Resin Transfer Molding (VARTM) process.

Mahmoud Ramadan Abusrea is with the Kyushu University, Japan (e-mail: mahmoud.r.abusrea.127@s.kyushu-u.ac.jp).

II. Experimental Work

The composite material was CFRP, consisting of a carbon fabric hardened with a resin. All CFRP fabrics were produced using VARTM. The entire process comprised three steps: fabricating a vacuum package, infusing the resin and molding. The structure of the vacuum package used in the experiment is shown in Fig. 1 (a). A solid mold, covered with a piece of peel ply, was used. Four layers of stitched unidirectional carbon-fiber fabric (from Saertex GmbH & Co. KG, the carbon fiber is TENAX STS, the stitching material is PES) with 30 cm in length were laid on the peel ply and then covered by another piece of peel ply. The horizontal direction of Fig. 1 (a) was the fiber direction. A small piece of distribution medium, a kind of mesh, was placed on the peel ply to promote the flow of resin.

The inlet for infusion, which was composed of a rubber connecter and a segment of spiral tube, was positioned on the distribution medium. The vent for air and excess resin elimination was positioned on the other side of the inlet. Both inlet and vent were composed of a rubber connecter and a segment of spiral tube. Since inlet and vent considered very critical points in the entire process, they are tightly sealed by the sealant tape. Finally, the entire package was enclosed in a vacuum bag and sealed with tape. Fig. 1 (b) shows a picture of the adopted structure. After establishing a vacuum, degassed resin was infused from the inlet. After 40 min, the inlet was closed, and the vent was left open until the resin was cured. An epoxy resin that could be cured at room temperature (XNR/H 6815, supplied by Nagase & Co., Ltd.) was used in the experiment. The initial viscosity of the resin at 25°C was 260 MPa s. When the resin was cured completely (about 24 h later), the CFRP laminate was removed from the mold. The thickness of the plate was about 2 mm.

Joint strengths were evaluated via tensile testing using standardized test specimens [1]. Fig. 2 shows the dimensions of the specimens; the total length was 250 mm and the width was 10 mm. Pairs of GFRP tabs were used to reduce the stress when holding each specimen. All specimens are tested using SHIMADZU DSS-5000 universal testing machine. Fig. 3 shows the setup used for the current tensile test. The specimen was fixed between the machine's jaws, and the load-time data

was recorded through a load cell mounted on the upper jaw. A real time camera connected to PC was mounted to record the deformation of the specimen during the loading.

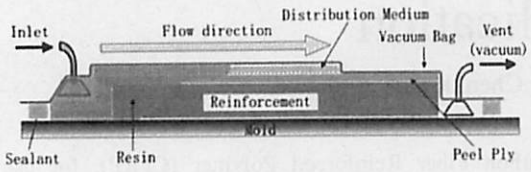

(a)

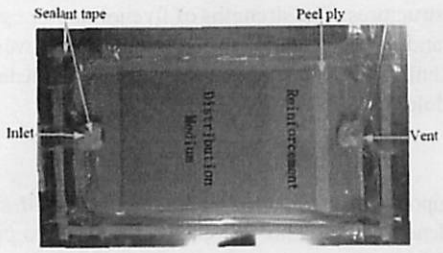

(b)

Fig. 1 (a) A schematic view of the VARTM process used in this work and (b) Picture of adopted VARTM process

The strength of the original CFRP was measured, and used as a reference for the strength of subsequent joints. Five joint types were tested, divided into two groups. One was constructed using dry carbon fabrics and CFRP. In this group, the CFRP half of the joint was manufactured first, and then re-molded again with dry carbon fabric. Fig. 4 shows types 1 and 2 of the first joint group. The left half of both joints was a stepped CFRP portion that had been molded, and the right side represents a dry carbon fabric. We used these to investigate the effects of the number of steps connected to dry carbon fabrics, and therefore the major difference between the two joints is the number of CFRP steps.

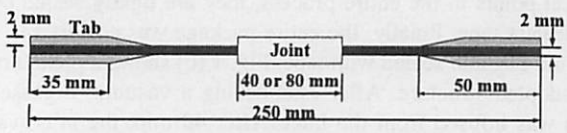

Fig. 2 The standard specimen dimensions used for tensile testing

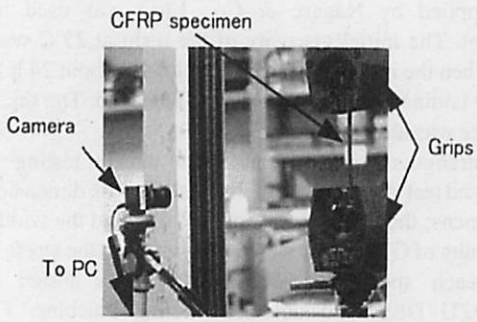

Fig. 3 Tensile test setup for the current work

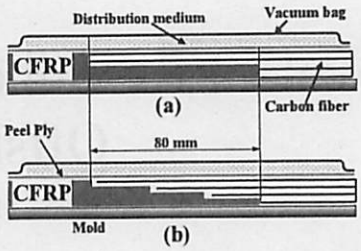

Fig. 4 Joint group 1: (a) staircase joint-1, and (b) staircase joint-2

The second group was constructed with two dry carbon fiber halves; thus, the whole joint was made in a single step. Fig. 5 shows types 3, 4, and 5 of the second joint group. These joints were named laminated joint-1, laminated joint-2, and multi-overlapped joint, respectively.

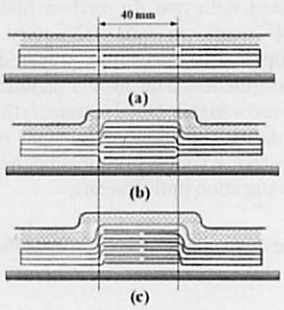

Fig. 5 Joint group 2: (a) laminated joint-1, (b) laminated joint-2, and (d) multi-overlapped joint

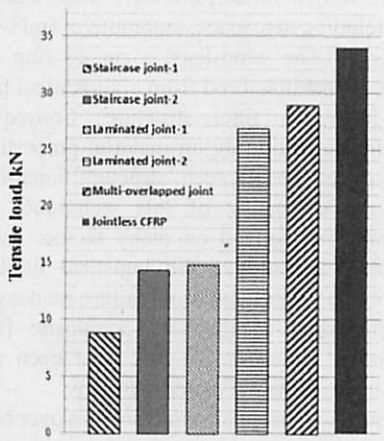

Fig. 6 Tensile strengths of the joints and the original CFRP material

III. Results and Discussions

Fig. 6 shows the tensile strengths of the five joints, and the original CFRP. A tensile load of 34 kN was recorded for the CFRP, indicating that the tensile strength along the fiber direction was 1.7 GPa.

The lowest joint tensile strength recorded was for staircase joint-1, with a measured strength of 8.8 kN (26% joining efficiency). However, the strength of the other staircase joint, staircase joint-2, was significantly higher (14.3 kN; 42% joining efficiency), and this is in agreement with previous

studies that have suggested that joining carbon fabrics and CFRP fabrics results in low strength [1]. This behavior can be attributed to two factors. First, resin residue on the CFRP surface before joining can act as an insulator. Second, the absence of overlap contact in these joints reduces the contact area, resulting in a weaker joint [10]. On the other hand, staircase joint-2 achieved a much higher strength than joint-1. This is attributed to the three fiber layers in that joint type that contact the CFRP part, three times more than the number of layers in joint-1. Hence, joining dry carbon fabrics together resulted in generally higher strengths. The laminated joint-1 had a tensile strength similar to that of staircase joint-2, with a measured strength of 14.7 kN. This can be attributed to the absence of overlap contact between the two halves in laminated joint-1, which reduces the strength and promotes crack propagation near the joint ends. The introduction of overlap areas not only increases the contact area, but also increases joint thickness. On the other hand, the remaining two joints were much stronger than the previous four joints. Laminated joint-2 and the multi-overlapped joint had tensile strengths of 26.8 kN (79%) and 28.8 kN (85%), respectively. These two joints performed similarly, with the major difference being the greater thickness of the multi-overlapped joint-2, which could be the reason for the higher observed strength. Löbel et al. [10] constructed CFRP joints based on stainless pins, which resulted in a high joining efficiency of 83%. However, the metal-to-carbon fiber contact caused galvanic corrosion of the carbon fabrics, weakening the structure over time [12].

Fig. 7 shows a typical tensile load-displacement diagram combined with images that show the deforming specimen of the staircase joint-1. In staircase joint-1, an initial crack occurred near the end of the joint, which reduced the gradient of the load-displacement curve. This resulted in a linear relationship between the tensile load and displacement. As the load increased, the crack size also increased until the specimen ultimately fractured. As noted, the initial cracking occurred at the end of the joint. This behavior can be explained as follows. In staircase joint-1, when joining the CFRP with carbon fabric, two separation lines were formed on both surface sides (Fig. 8). These two lines were filled with resin after joining, and the crack initiated at these lines at the beginning of the tensile test. As the tensile load increases, the shear stress in the contact area increases and this causes relative motion between the CFRP portions. This leads to the enlargement of both separation lines and hence crack propagation. The failure patterns were also investigated for other joint types. Fig. 9 shows a typical tensile load-displacement diagram for multi-overlapped joint-2. Two cracks appeared near the joint ends, due to the accumulation of stress in these zones, which apparently caused a gradient change. Then the cracks propagated until specimen fracture. Fig. 10 shows a schematic drawing of the multi-overlapped joint-2. The possible zones of fracture are near the joint ends, where there is an accumulation off stress.

There are seven failure modes, including but not limited to the separation of the interface between the adhesive and composite, de-lamination within the composite, and a mixture of these two modes [13]. Micromechanical investigations have revealed different dominant failure modes under tensile and shear loads [5]. In addition, the strength of the interface between the adhesive and composite at a joint is a key factor determining the failure mode and the strength of a structure. In the present study, both staircase joints 1 and 2 showed separation of the interface, whereas joint group 2 showed a mixture of failure modes.

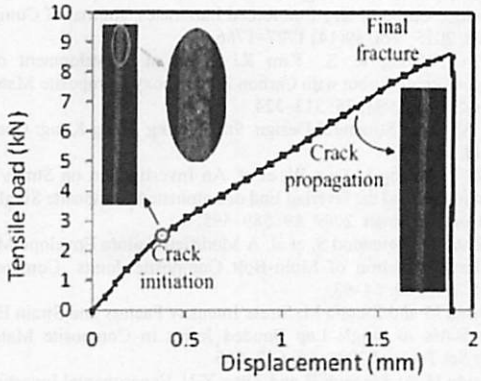

Fig. 7 A diagram of typical tensile load-displacement, with images for staircase joint-1

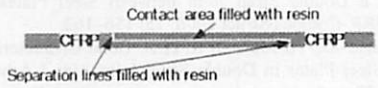

Fig. 8 Schematic drawing of a staircase joint after bonding

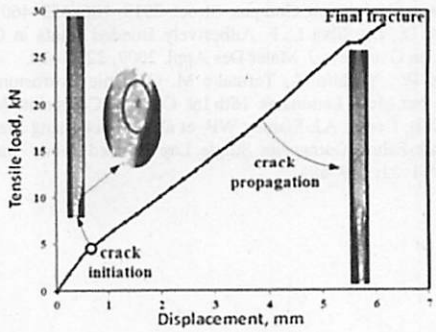

Fig. 9 Typical tensile load-displacement diagram with images for a multi-overlapped joint

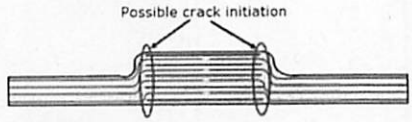

Fig. 10 Schematic drawing of a multi-overlapped joint with possible crack zones highlighted

IV. Conclusions

Five adhesive joints were designed using manufacturing process developed from the VARTM process. The tensile test results showed low strength when one-half of the joint is CFRP fabrics, which was the case for the first two developed joints. On the other hand, the last two joints, laminated joint-2 and

multi-overlapped joint, showed higher tensile strength. However, joining techniques that use dry carbon fibers are still limited for simple shapes, so there are some difficulties for applying these techniques for complex curved shapes like wind blades and lens as well.

REFERENCES

[1] Chen D.D., Arakawa K, Jiang S.Y. Novel Joints Developed from Partially Un-Moulded Carbon-Fibre-Reinforced Laminates. Journal of Composite Materials, 2015, Vol. 49(14) 1777–1786.
[2] Lee D. G., Jeong K. S., Kim K. S., et al. Development of the Anthropomorphic Robot with Carbon Fiber Epoxy Composite Materials. Compos. Struct. 1993; 25: 313–324.
[3] Niu M. Airframe Structural Design. 9th Printing. Hong Kong: Conmilit. Press Ltd.; 1997.
[4] Wang Z. Y., Wang L, Guo W, et al. An Investigation on Strain/Stress Distribution around the Overlap End of Laminated Composite Single-Lap Joints. Compos Struct. 2009; 89: 589–595. 3.
[5] Liu F, Zhao L, Mehmood S, et al. A Modified Failure Envelope Method for Failure Prediction of Multi-Bolt Composite Joints. Compos Sci. Technol. 2013; 83: 54–63.
[6] Quaresimin M and Ricotta M. Stress Intensity Factors and Strain Energy Release Rates in Single Lap Bonded Joints in Composite Materials. Compos Sci Technol 2006; 66: 647–656.
[7] Al-Zubaidy H, Al-Mahaidi R and Zhao X-L. Experimental Investigation of Bond Characteristics between CFRP Fabrics and Steel Plate Joints under Impact Tensile Loads. Compos Struct 2012; 94: 510-518.
[8] Fawzia S, Al-Mahaidi R and Zhao X-L. Experimental and Finite Element Analysis of a Double Strap Joint between Steel Plates and Normal Modulus CFRP. Compos Struct 2006; 75: 156–162.
[9] Fawzia S, Zhao XL, Al-Mahaidi R, et al. Bond Characteristics between CFRP and Steel Plates in Double Strap Joints. Int J Adv Steel Constr 2005; 1: 17–27.
[10] LÖbel T., Kolesnikov B, Scheffler S, et al. Enhanced Tensile Strength of Composite Joints by Using Staple-Like Pins: Working Principles and Experimental Validation. Compos. Struct. 2013; 106: 453–460.
[11] Banea M. D., Da Silva L. F. Adhesively Bonded Joints in Composite Material: an Overview. J. Mater Des Appl. 2009; 223:1–18.
[12] Wen-Xue W., Yoshiro T., Terutake M. Galvanic Corrosion-Resistant Carbon Fiber Metal Laminates. 16th Int. Conf. on Composite Materials.
[13] Katnam KB, Comer AJ, Stanley WF, et al. Characterising Pre-Preg and Non-Crimp-Fabric Composite Single Lap Bonded Joints. Int J Adhes Adhes 2011; 31: 679–686.

国際化推進共同研究概要

No.15

タ イ ト ル: Effects of compaction on interlaminar fracture toughness of laminated CFRP composites fabricated by vacuum-assisted resin-transfer molding

研究代表者: CHOI, Nak-Sam

所内世話人: 新川 和夫

実 施 期 間: 2016 年 1 月 13 日 ～ 1 月 16 日

概要:
真空樹脂含浸法により製作した炭素繊維強化複合材料(CFRP)に及ぼす圧縮力効果についてアコースティックエミッション(AE)法により調べた。そして圧縮力により CFRP の層間破壊強度が大きく変化することを明らかにした。

Effect of Compaction Treatment on Laminated CFRP Composites Fabricated by Vacuum-Assisted Resin-Transfer Molding

Sang-Jae Yoon,[1] Kazuo Arakawa,[1] Seung-Wook Han,[2] Dingding Chen,[3] Nak-Sam Choi[2]
[1]*Kyushu University*

[2]*Hanyang University*

[3]*National University of Defense Technology*

Carbon fiber-reinforced polymer (CFRP) composites were fabricated using ordinary and compaction setups (OS and CS, respectively) in the vacuum-assisted resin-transfer molding (VARTM) process. The mechanical properties and acoustic emission (AE) spectra of the CFRP composites were compared among fabricated samples. The CFRP plates with sequences of $[+30/-30]_6$ were sectioned to make specimens for Mode I interlaminar fracture tests and three-point bending tests. The difference between the material properties and AE characteristics of the OS and CS specimens were statistically compared using one-way analysis of variance. The OS specimens had a thicker resin layer, a higher resin fraction, larger average fracture toughness, and AE energy corresponding to the Mode I fracture, whereas the CS specimens had more macro-scale voids and higher bending strength. AE analysis showed that frequency bands in the interlaminar fracture tests corresponding to matrix-related fracture were dominant for the OS specimens, whereas those corresponding to the mixed fracture mode of the fiber and matrix fracture were dominant for the CS specimens. In the bending tests, mixed fiber-matrix fractures were dominant for the OS specimens, and fiber-related fractures were dominant for the CS specimens. In conclusion, the compaction treatment diminished interlaminar fracture toughness, due to the enhanced formation of macro-scale voids around the fiber bundles during the resin impregnation stage. However, the bending strength improved with an increased fiber volume fraction. POLYM. COMPOS., 00:000–000, 2015. © 2015 Society of Plastics Engineers

Correspondence to: Nak-Sam Choi; e-mail: nschoi@hanyang.ac.kr
Contract grant sponsor: Japan Society for the Promotion of Science; contract grant number: 26630496; contract grant sponsor: Collaborative Research Program of the Research Institute for Applied Mechanics, Kyushu University.
DOI 10.1002/pc.23578
Published online in Wiley Online Library (wileyonlinelibrary.com).

INTRODUCTION

Laminated composite materials have been used as structural elements in fields including aerospace, wind power plants, and automotive vehicles. Conventional composite parts may be manufactured using an autoclave method with a pre-preg process. However, because the autoclave uses facilities for high heat and large pressures in the curing stage, substantial installation costs are incurred with composite fabrication [1].Vacuum-assisted resin-transfer molding (VARTM) is a popular alternative method. VARTM is a composite fabrication process whereby the thermoset resin is injected into a mold through inlet ports, and the materials contained in the mold are infiltrated with the resin using the vacuum. This process has the advantages of cost efficiency, and fabrication and maintenance simplicity [2].

The VARTM process has three basic steps: fiber impregnation, consolidation (i.e., the application of pressure), and curing [3]. In this process, the quality of the contact between layers is influenced by several factors, including the mold temperature, fiber orientation, resin viscosity, and pressure in the mold [4–7]. However, significant defects may occur, depending on the local pressure gradient and permeability of the fabrics [8]; an inappropriate filling method may therefore lead to the formation of voids, as well as nonuniformity of the resin distribution, both of which can degrade the mechanical properties of the finished product. Composite products fabricated using a typical VARTM setup generally exhibit low compaction forces and a rough surface near the vacuum bag side. Therefore, various developed RTM processes have been adapted to improve dimensional tolerances and surface quality [9].

Here, we report the effects of an additional treatment, i.e., compacting the fiber fabrics using a rigid covering metal mold, in order to improve the properties of carbon

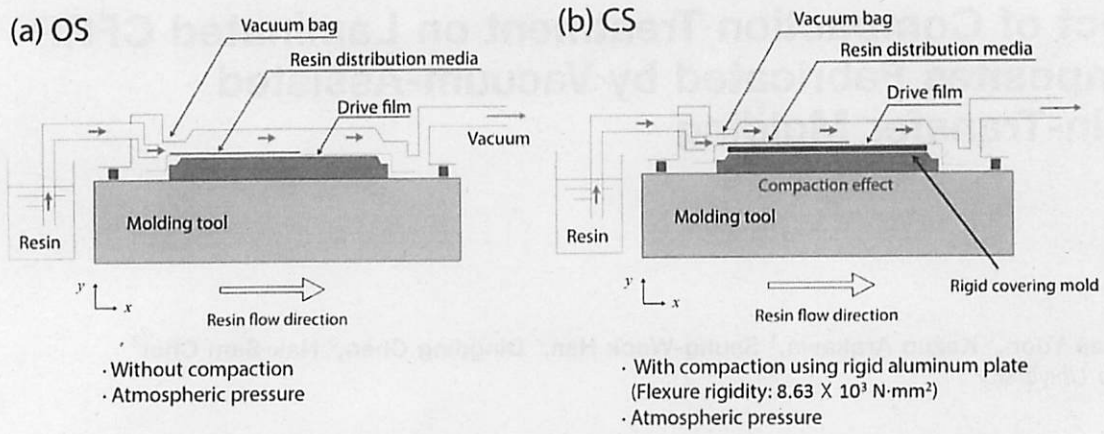

FIG. 1. Schematic diagram showing the VARTM process for specimen fabrication: (a) the ordinary setup (OS) and (b) the compaction setup (CS). [Color figure can be viewed in the online issue, which is available at wileyonlinelibrary.com.]

fiber-reinforced polymer (CFRP) composites fabricated using a VARTM process. Two types of CFRP plates were prepared using a VARTM setup: the first used the ordinary setup (OS) to fabricate samples, and the second used the compaction setup (CS). The effect of compaction on the mechanical properties was investigated using the Mode I interlaminar fracture and three-point bending tests. A new testing method was adopted for the interlaminar fracture test, which is described in our previous study [10]. To explore the fracture mechanism during the tests, the acoustic energy (AE) characteristics were monitored in real time. To examine the released energy as function of time and the total energy released during failure, we considered the amplitude distribution and the cumulative energy as the main AE parameters. In addition, since the frequency components of the AE signal describe the fracture mechanism, we also considered the peak frequency of the AE signal, which was obtained using a fast Fourier transform (FFT). The differences in the mechanical properties and the AE characteristics of the OS and CS specimens were statistically compared.

EXPERIMENTAL PROCEDURE

VARTM Process

Laminated CFRP composites were prepared using the OS and CS procedures, as illustrated with side views in Fig. 1a and b. Here, a resin distribution medium was used to achieve uniform and rapid resin dispersion. The OS procedure was an ordinary transverse flow VARTM setup that is commonly employed to fabricate large parts [1]. The CS procedure included a modified setup with an additional compaction treatment, whereby a 0.5-mm-thick, rigid, porous aluminum plate was placed on the fabric lay-up, and then pressed under atmospheric pressure. Although the carbon fabric of OS and CS preforms in a closed mold were equally compressed by atmospheric pressure, several effects were expected during plate compression, including enhanced resin flow and an acceleration in excess resin extrusion during the post-filling stage. The flexural rigidity and individual hole size diameter of the plate were 8.63×10^3 N·mm^2 and 1 mm, respectively. With the exception of the compaction, all of the fabrication conditions for OS and CS were the same. Stitched multidirectional carbon fiber fabrics [SAERTEX] were laid up on a mold with sequences of $[+30/-30]_6$. A 25-μm-thick Teflon film was inserted as a starter crack at the edge of the plate, as shown in Fig. 2a. The fabrics were sealed in a vacuum bag, followed by room temperature curing of an epoxy resin [Nagase ChemetX] impregnated into the fiber layers using a vacuum. The entire process was carried out at room temperature.

Specimen Preparation

The CFRP plates were sectioned to form specimens for Mode I fracture and three-point bending tests, with geometries as shown in Fig. 2b and c, respectively. Eight specimens were prepared for each condition.

For the Mode I fracture tests, a new design was used; pieces with an initial crack were packed between two rectangular epoxy plates to clamp the specimen to a testing machine [10]. Additionally, the specimen was adapted to AE measurement to substitute for DCB testing. The epoxy plates were attached to the CFRP piece using the same resin as was used for the VARTM process to improve adhesion among the pieces and epoxy and to reduce AE signal attenuation from the crack to the sensor. The two plates and the CFRP were directionally aligned using two frames to prevent dislocation of the specimens. The samples were sectioned for Mode I interlaminar fracture tests, resulting in specimens that were 3 mm in width and 20 mm in length, with a 5-mm-long starter crack. Two factors did not comply with the standard DCB test (ASTM 5528), as described below. (i) The standard recommends unidirectional $[0]_n$ laminates; however, we

DOI 10.1002/pc

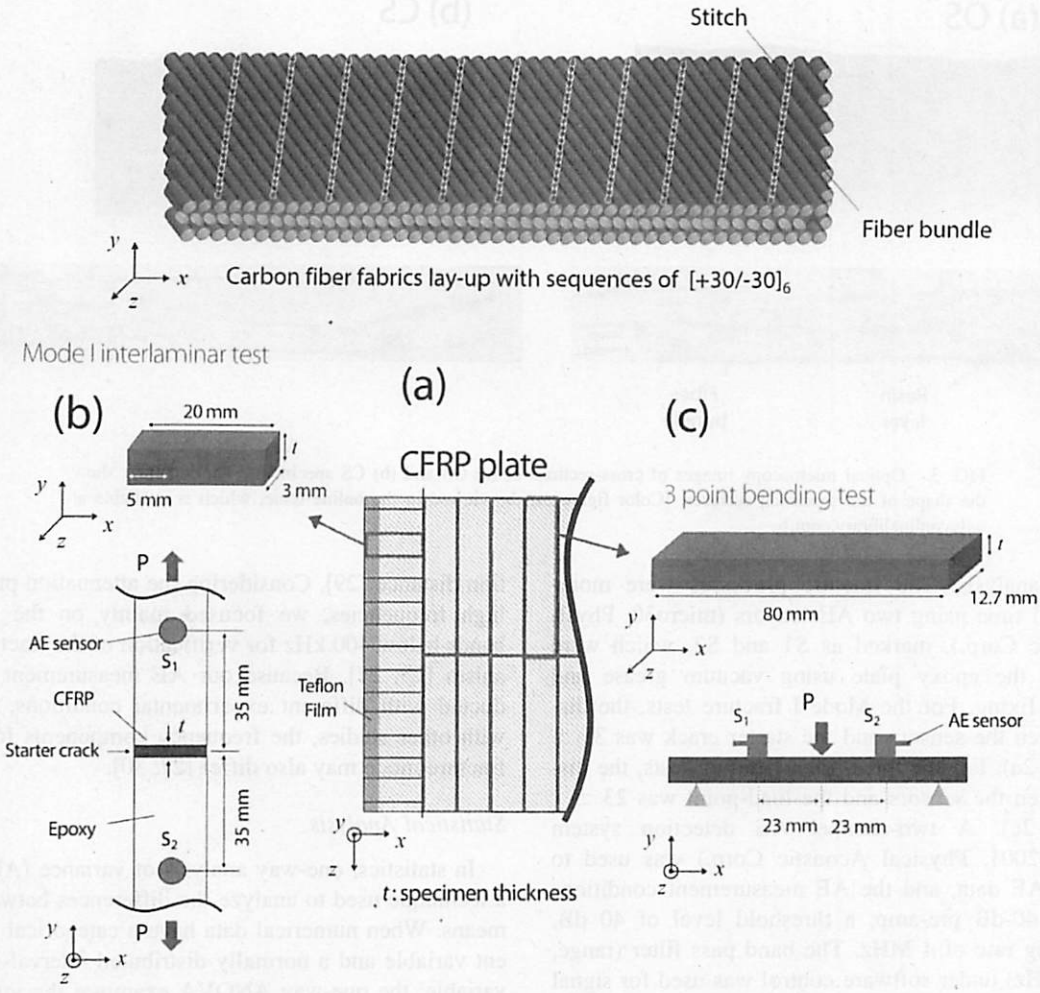

FIG. 2. Specimen preparation procedure. (a) The location of specimens taken from the CFRP plate. (b) An illustration of the specimen for the Mode I fracture test with AE monitoring. (c) An illustration of the specimen for the three-point bending test with AE monitoring. [Color figure can be viewed in the online issue, which is available at wileyonlinelibrary.com.]

preferred multidirectional $[+30/-30]_6$ for practical application. Various studies have conducted Mode I interlaminar fracture tests using multidirectional composite specimens, which were reportedly influenced by the lay-up angle, as opposed to the behavior of the unidirectional laminates [11–17]. For example, especially between $[0]_n$ and $[30/-30]_n$, Ozdil et al. analytically and experimentally compared the differences under DCB testing, specifically, the compliance values predicted by the elastic-foundation model, the fracture toughness, load–displacement curves, and fracture resistance [18]. (ii) Although the thickness of the starter film (25 μm) complied with JIS K7086 (no greater than 30 μm), it did not comply with the ASTM 5528 specifications (no greater than 13 μm) [19, 20]. Other studies reported that the film thickness is a function of the resin-rich zone in front of the film and the sharpness of the crack tip radius. When a crack, initiated from a starter crack, enters the laminate, the crack penetrates the pure resin region if the resin-rich zone is thick. With the crack tip assumed to be infinitely sharp in fracture mechanics, these two effects may lead to unexpected interlaminar fracture characteristics [21, 22]. Therefore, the fracture toughness of the Mode I fracture test in this study was likely to be affected. The specimens for the three-point bending tests were sections that were 10 mm in width and 80 mm in length according to ASTM D790.

Fracture Tests With AE Measurements

The Mode I fracture and three-point bending tests were carried out using a universal testing machine (Zwick 250, testXpert version 11.02) at room temperature, with a crosshead rate of 1 mm/min for the Mode I fracture tests and 3 mm/min for the three-point bending tests. Fractographic analysis was carried out on the fracture surface of the Mode I fracture test specimens using optical microscopy and scanning electron microscopy (SEM). The fractographic results were used for quantitative and

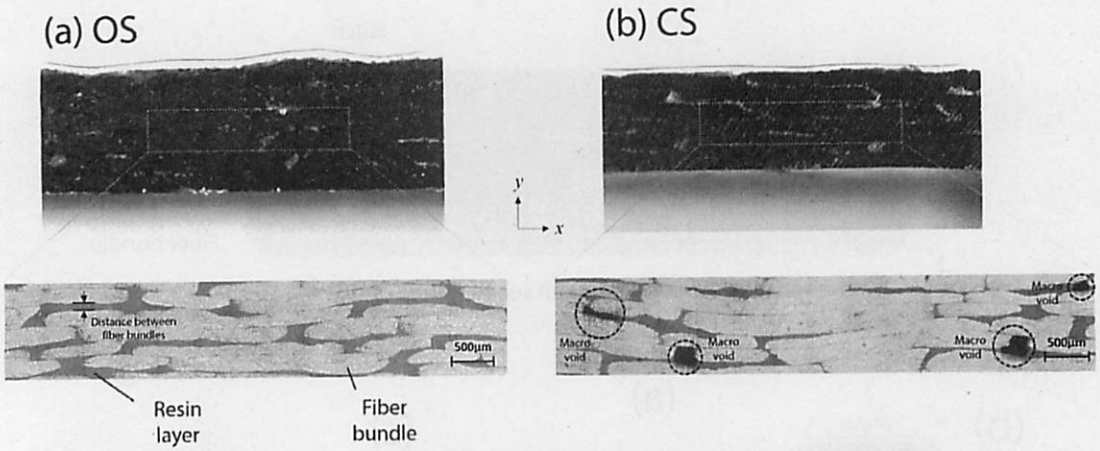

FIG. 3. Optical microscopy images of cross-sections of (a) OS and (b) CS specimens. The red lines show the shape of the specimen surfaces. [Color figure can be viewed in the online issue, which is available at wileyonlinelibrary.com.]

qualitative analysis. The fracture processes were monitored in real time using two AE sensors (micro30, Physical Acoustic Corp.), marked as S1 and S2, which were attached to the epoxy plate using vacuum grease and mechanical fixing. For the Mode I fracture tests, the distance between the sensors and the starter crack was 35 ± 1 mm (Fig. 2a). For the three-point bending tests, the distance between the sensors and the load-point was 23 ± 1 mm (Fig. 2c). A two-channel AE detection system (MSTRAS 2001, Physical Acoustic Corp.) was used to record the AE data, and the AE measurement conditions included a 40-dB pre-amp, a threshold level of 40 dB, and sampling rate of 4 MHz. The band pass filter (range, 1 kHz–1 MHz) under software control was used for signal gain for specific frequencies. The timing parameters of the signal measurement process, peak definition time (PDT), hit definition time (HDT), and hit lockout time (HLT), were determined following the manufacturer's recommended values for the composites. Three AE parameters were investigated: the amplitude, i.e., the maximum (positive or negative) AE signal excursion during an AE pulse; the energy, i.e., the integral of the rectified voltage signal over the duration of the AE pulse; and the frequency spectrum of the AE signal, which was obtained using an FFT. AE analysis provides the means to identify and differentiate fracture sources. However, because the AE signals are influenced by attenuation and dispersion [23–28], the stacking sequence, layer number, fracture mode, propagation distance from the source position, and the signal velocity dependence on the frequency components should also be considered. In this study, the OS and CS specimens were virgin, uncoated samples, with the same number of layers and stacking sequences. We assumed that the distance between the sensor and the crack was sufficient to measure the AE characteristics. The AE amplitude and energy were utilized for comparison between the OS and CS specimens, mainly because such factors attenuate significantly with respect to the propagation distance [29]. Considering the attenuation problems at high frequencies, we focused mainly on the frequency bands below 400 kHz for verification of the fracture mechanism [25, 27]. Because our AE measurement was conducted with different experimental conditions, compared with other studies, the frequency components for a given fracture mode may also differ [27, 30].

Statistical Analysis

In statistics, one-way analysis of variance (ANOVA) is a technique used to analyze the differences between group means. When numerical data have a categorical independent variable and a normally distributed interval-dependent variable, the one-way ANOVA examines the influence of one factor of the independent variable on a dependent variable. If there are differences among the group means, post hoc tests are used to explore specific information to identify those that are significantly different. In this study, the one-way ANOVA and Tukey's post hoc tests ($p = 0.05$) were used to determine the significance of differences among the mechanical properties and the cumulative AE energies of OS and CS specimens. Here, the null hypothesis of the one-way ANOVA corresponded to "no difference between the means of the variables". The significance probability value (p-value) is the probability that the null hypothesis is true. For example, a p-value less than the predetermined significance level (0.05 in this study) means that the null hypothesis can be rejected with 95% confidence.

RESULTS

Thickness and Smoothness of the CFRP Plates

Figure 3a and b show cross-sections of the OS and CS specimens. The qualitative observation of the cross-sections indicated that the OS specimens had rougher surfaces and thicker resin layers than the CS specimens. Interestingly, noticeable voids were observed in the CS

DOI 10.1002/pc

TABLE 1. Mean specimen thickness and fiber volume fraction for ordinary and compaction setup specimens.

	Specimen thickness (mm)	Distance between fiber bundles (mm)	Ratio of resin fraction
OS	3.0 (0.2)	0.125 (0.02)	18%
CS	2.5 (0.1)	0.085 (0.02)	12% porosity: 2 %

The values shown in parenthesis are the standard deviations.

specimens, which will be discussed later. The surface shape of composites fabricated using VARTM processes are typically determined by resin hardening. Wrinkle effects from the vacuum bag may have influenced the roughness of the OS specimens, whereas the rigid mold of the CS specimens resulted in smoother surfaces.The fiber volume fraction, f_{fiber}, is given by

$$f_{fiber}=\frac{n\cdot\rho^{s}_{fiber}}{\rho^{v}_{fiber}\cdot h}, \quad (1)$$

where n is the number of fabric layers, ρ^{s}_{fiber} is the areal density of the fabric, ρ^{v}_{fiber} is the volume density of the fabric, and h is the thickness of the specimen [31].

Table 1 lists the average thickness, as well as the fiber volume fraction, for both the OS and CS specimens. The average (visible) porous fraction was indicated for the CS specimen. Because this study mainly focused on the critical factors affecting CFRP properties, such as the large porosity and fiber volume fraction in previous studies [32], we placed more emphasis on the macro-scale voids as opposed to micro-scale voids. Thus, micro-scale voids between the interfaces of the fiber tows were not considered. To determine the porous fraction quantitatively, we recognized voids greater than 0.1 mm^2 as visible voids, and then calculated the proportion in cross-sectional images of each specimen. The OS specimens had higher thickness and lower fiber volume fraction than the CS specimens, and the porous fraction in the CS specimen was 1.45 ± 0.3%.

Mode I Interlaminar Fracture Tests

Figures 4 and 5 show typical tensile loads and the AE amplitude distribution as function of time for the OS and CS specimens, respectively. The specimens showed similar tensile loads and AE amplitude characteristics, regardless of whether the specimens were fabricated using the OS or CS procedures. Stage regimes marked in Figs. 4 and 5 will be explained later.

The fracture toughness of a specimen, K_I, is given by

$$K_I=\sigma\sqrt{\pi a}\,F(a/W), \quad (2)$$

where σ is the tensile stress, a is the crack length, and W is the width of the specimen. Expressing $a/W=\xi$, we can write the specimen geometric factor at the crack tip [33] as

$$F(\xi)\fallingdotseq 1.12-0.231\xi+10.55\xi^2-21.72\xi^3+30.39\xi^4. \quad (3)$$

Table 2 lists the mean K_I and cumulative AE energy values for the OS and CS specimens; both values were larger for the OS specimens than for the CS specimens (p for the K_I = 0.048 and p for the interlaminar AE energy = 0.000). Since K_I is a critical parameter describing the fracture toughness required to propagate the crack, and the AE energy represents the released fracture energy during crack propagation, these indicate that more energy was required for crack initiation and subsequently

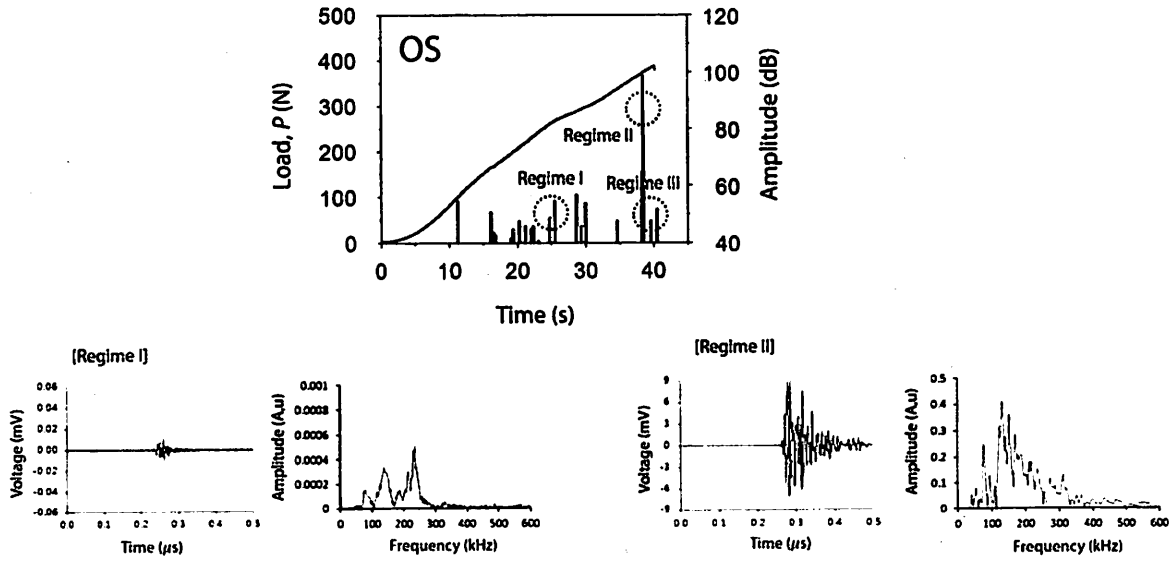

FIG. 4. Tensile load and the corresponding AE behavior as a function of time for the Mode I fracture test for OS specimens. [Color figure can be viewed in the online issue, which is available at wileyonlinelibrary.com.]

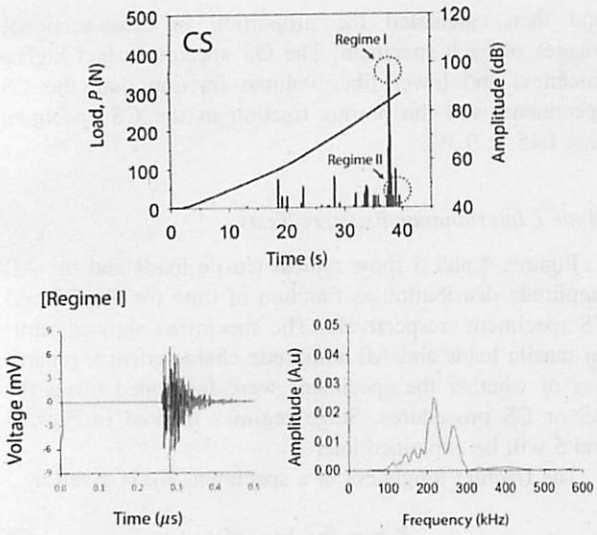

FIG. 5. Tensile load and the corresponding AE behavior as a function of time for the Mode I fracture test for OS specimens. [Color figure can be viewed in the online issue, which is available at wileyonlinelibrary.com.]

released during crack propagation for the OS specimens than for the CS specimens. Note that the compaction treatment caused a reduction in K_I. Although the thickness variation for the OS specimens was greater than that for the CS specimens due to the rougher surface (Table 1), the CS specimen showed higher standard deviations for K_I (Table 2). The macro-scale voids may more strongly affect K_I than the thickness variation; this will be discussed later.

Figures 6 and 7 show typical fracture surfaces of the Mode I fractures for the OS and CS specimens, respectively, taken using optical microscopy and SEM. The OS

TABLE 2. Mean fracture toughness K_I and cumulative AE energy for Mode I fracture test specimens fabricated using OS and CS procedures.

	Fracture toughness K_I
OS	35.47 (6.20)
CS	33.59 (7.64)

The values shown in parenthesis are the standard deviations.

and CS specimens showed qualitatively different fracture surfaces. The OS specimens exhibited three regimes: a slow crack (Stage I), single crack growth extending into the other layer (Stage II), and fast crack propagation without rerouting (Stage III). The fracture surface was relatively distinct. The CS specimens displayed two regimes: crack growth (Stage I), and fast crack propagation (Stage II). The fracture surface was more complicated with significant stitches and fiber pull-outs. This indicates that the crack propagated along the matrix layer with less fiber pull-out due to stronger adhesion between the matrix and fiber in the OS specimens, whereas fiber fracture and debonding of the matrix/fiber interface occurred with significant fiber pull-out in the CS specimens. In particular, coagulated voids were observed in the CS specimens (Fig. 7a).

To clarify the fracture behavior subjected to tensile loading, we classified the stage regimes of the AE signals with respect to the fracture mode obtained from fractography. First, we compiled amplitude and frequency values, and then explored the characteristics of the two factors: the boundary of sudden amplitude change and the frequency band of the AE signals. For example, the Stage I regime for the OS specimen occurred just before a sudden increase in the AE amplitude, corresponding to a frequency band ranging from 150–240 kHz. Here, to

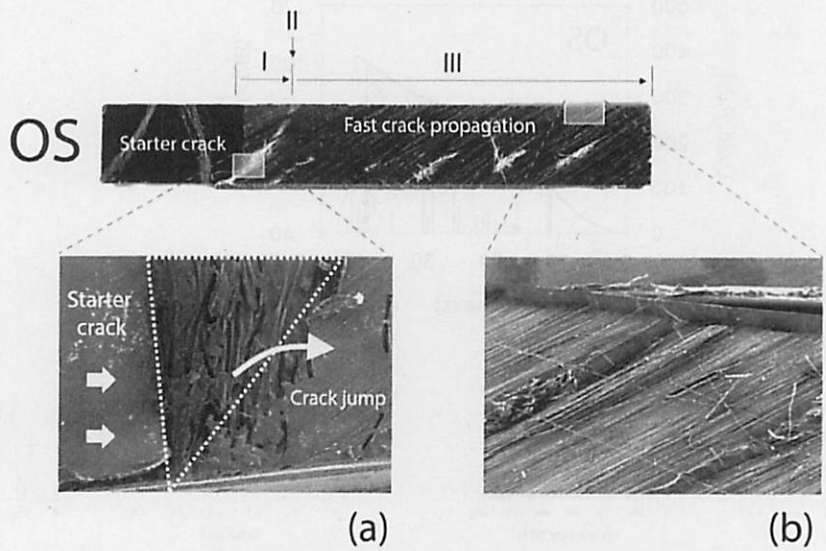

FIG. 6. Optical microscopy and SEM images of the fracture surfaces of OS specimens. [Color figure can be viewed in the online issue, which is available at wileyonlinelibrary.com.]

DOI 10.1002/pc

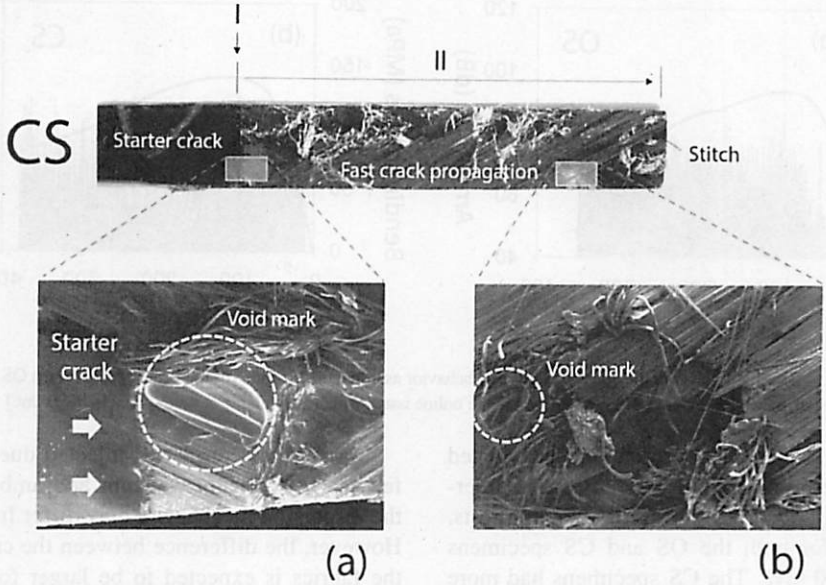

FIG. 7. Optical microscopy and SEM images of the fracture surfaces of CS specimens. [Color figure can be viewed in the online issue, which is available at wileyonlinelibrary.com.]

examine the fracture mechanism as a function of the AE frequency, we referred to previous studies that identified spectral features below 160 kHz corresponding to resin matrix fracture, spectral features in the range of 160–240 kHz that corresponded to matrix–fiber mixed fractures, and features above 240 kHz that were associated with fiber fracture [34, 35]. Because the matrix–fiber mixed fracture was observed from the slow crack area (Fig. 6a), we assumed that the AE signals in Stage I were recorded during slow crack formation. Using the procedure mentioned above, we indicated the stage regimes in Figs. 5 and 6 in addition to the fracture modes and corresponding frequency band for the OS and CS specimens (Table 3). In Figs. 5 and 6, because the Stage III regime of the OS specimen and Stage II regime of the CS specimen consisted of catastrophic fractures with fast crack propagation, the signals in this stage were not discussed in detail. Note that when the signals with high amplitudes occurred, the frequency bands for the two conditions were different: the OS specimens had a frequency below 160 kHz (representing matrix-related fracture), whereas the CS specimens had a frequency above 160 kHz (representing matrix–fiber mixed fracture). This indicates that, in the early stages of propagation, the cracks in the OS specimens grew and propagated along the resin layer with jumping, whereas crack propagation in the CS specimens involved mixed fracture. The differences in the fracture behavior of the OS and CS specimens are listed in terms of the ratio of the magnitude of the AE frequency components in Table 5. Here, we considered the three frequency bands described above, and collated the data as ratios for the Mode I fracture test. More matrix fractures occurred for the OS specimens, while more fiber-related fractures occurred for the CS specimens.

Bending Tests

Figure 8a and b show typical three-point bending stress and amplitude distributions of the AE signals as functions of time for the OS and CS specimens, respectively, and Table 4 lists the mean bending strength. The bending strength of a specimen, σ_b, is given by

$$\sigma_b = 3PL/2bd^2, \tag{4}$$

where P is the maximum load point on the load–deflection curve, L is the support span, b is the width of the specimen, and d is the thickness of the specimen. Although the bending load and AE energy for the OS specimens were larger than those for the CS specimens (p for the bending AE energy = 0.036), the CS specimens had greater strength (p = 0.002). This was due to the fact that the bending strength is determined mainly by the thickness (see *Eq. 4*); the CS specimens were ~17% thinner than OS specimens with the same total areal fiber weight. Note that the bending strength was mainly dependent on the fiber density, which means that we can expect improved bending strength for samples fabricated using the compaction method. Table 5 lists the ratio of

TABLE 3. Main fracture modes and corresponding frequency bands for Mode I fracture test specimens fabricated using OS and CS procedures.

	Bending strength (Mpa)	Cumulative AE energy
OS	132.13 (7.54)	187269.52 (83286.46)
CS	148.44 (7.47)	110374.22 (38166.13)

The values shown in parenthesis are the standard deviations.

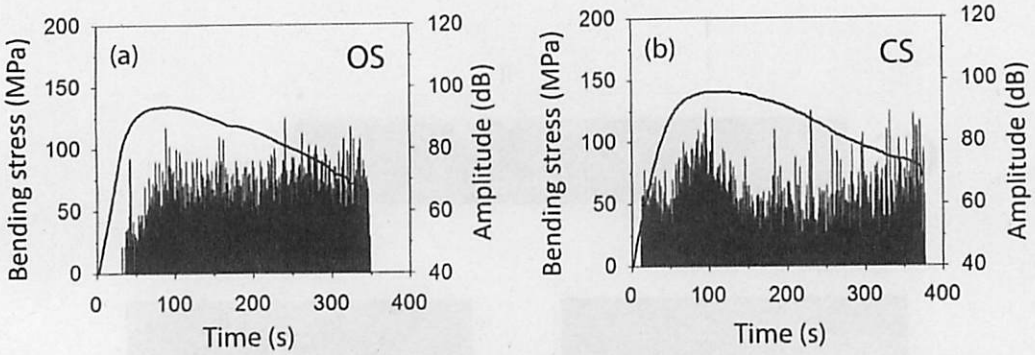

FIG. 8. Bending stress and the corresponding AE behavior as a function of time for the bending test for (a) OS and (b) CS specimens. [Color figure can be viewed in the online issue, which is available at wileyonlinelibrary.com.]

the magnitude of the AE frequency components collated as ratios for the three-point bending test. Because fiber-related fractures mainly occurred during the bending tests, the frequency bands for both the OS and CS specimens were mostly above 160 kHz. The CS specimens had more fiber fractures than the OS specimens did.

DISCUSSION

There have been a number of studies of the formation of voids in liquid composite molding processes, including resin-transfer molding (RTM) and the VARTM process. These studies have explored factors including injection pressure [36], resin viscous flow [37], wetting properties [38], and resin flow rate [39] to explain the mechanism of void formation and purging. However, the results of these depend on the materials. An explanation of the resin flow behavior is not straightforward, and many interdependent factors are involved.

Effects of Compaction on the Interior Structure of CFRP

Macro-Scale Void Formation With Lead-Lag Phenomena. Patel et al. reported a void formation mechanism due to trapped air, with a lead-lag phenomenon in unidirectional stitched fiber fabrics during liquid composite molding (LCM), whereby the liquid drives into stitched fiber fabrics during the liquid filling stage, the resin flow in the fiber bundles is affected by capillary pressure, and the resin flow in the gaps between the fiber bundles is affected by the hydrodynamic pressure acting on the liquid [37].

In our study, resin was injected due to the pressure difference between the vacuum and ambient pressure. Thus, the dispersion mechanism may differ from the above study. However, the difference between the capillary pressures of the fabrics is expected to be larger for the CS plate than the OS plate because of the compaction treatment. The hydrodynamic pressure acting on the resin was uniform for the two conditions at the same injection rate, with a pressure difference between the vacuum chamber and ambient of close to 1 atm. However, some residual air may have become trapped in the vacuum bag, leading to larger voids being trapped in the CS specimens. Here, the resin flow for the OS and CS plates (see Fig. 2) may have differed from the flow in the carbon fiber fabrics, where the fibers and stitches formed a rectangular structure.

Void Purge. Patel et al. also described a void purge mechanism during the resin bleeding process. When air is trapped, the hydrodynamic pressure of the trapped air (i.e., the voids) is stabilized by the capillary pressure. If the surrounding hydrodynamic pressure gradient overcomes the capillary pressure due to the resin flow, the trapped voids can be driven out during a bleeding stage [37]. In other words, even if the void becomes trapped due to lead-lag phenomena, it may be pushed out and purged. Therefore, we suppose that the voids in the OS

TABLE 4. Mean bending strength for bending test specimens fabricated using OS and CS procedures.

	Fracture mode	Frequency band (kHz)
OS	Slow crack (1)	150 - 240
	Crack growth with jumping (II)	90 - 160
	Fast crack propagation (III)	90 - 160
CS	Crack growth (1)	180 - 230
	Fast crack propagation (II)	140 - 250

TABLE 5. Fraction of the AE energy spectra that occurred in the various frequency bands described by Choi et al. and De Groot et al. for Mode I fracture, and bending test specimens fabricated using OS and CS procedures. Here, ≤ 160 kHz corresponds to resin matrix fracture, 160–240 kHz corresponds to matrix–fiber mixed fracture, and > 240 kHz corresponds to fiber fracture.

		Mode 1 fracture test	Bending test
OS	F≤ 160 kHz	0.738(0.173)	0.034(0.021)
	160 kHz <f ≤ 240 kHz	0.248(0.172)	0.760(0.124)
	f> 240 kHz	0.140(0.177)	0.207(0.123)
CS	F≤ 160 kHz	0.177(0.179)	0.003(0.003)
	160 kHz <f ≤ 240 kHz	0.779(0.070)	0.493(0.087)
	f > 240 kHz	0.203 (0.066)	0.504(0.086)

The values in parenthesis show the standard deviations of the data.

DOI 10.1002/pc

国際化推進共同研究概要

No.16

タイトル: Development of multi-rotor wind turbine system

研究代表者: JAMIESON, PETER

所内世話人: 大屋 裕二

実施期間: 2015年 月 日 ～ 月 日

概要:

風工学分野ではストラスクライド大学(グラスゴー、スコットランド)の Peter Jamieson 氏のグループとマルチレンズ風車の共同研究を行っている。単位電力の発電にかかるコストを下げるため近年まで世界の風車は大型の一途をたどっていた。しかし現在は次世代の技術革新がないこともあり大型化は行き詰り始めている。そんな中、これまで集風体付き風車の理論的研究でも実績のある Jamieson 氏のグループは複数の風車を同じ垂直平面上に並べ小型の風車の集合体で大きな定格発電量を実現する研究を始めていた。これは私たち風工学分野の志す「小は大を兼ねる」のコンセプトに合致するものであり、我々の数値計算および実験と Jamieson 氏のグループの理論的研究を融合し多角的な側面からマルチレンズ風車に関する共同研究を開始し、これまで多年度にわたり行っている。今年度の成果として 3kW レンズ風車を 3 基搭載した 10kW マルチレンズ風車の実証実験を開始した

Ducted Wind Turbines and Multi Rotor Systems

University of Strathclyde: Peter Jamieson (67 years, *male*)

Aim of the collaboration

The collaboration between Kyushu University RIAM and the University of Strathclyde (Glasgow, Scotland) was begun following an Invitation by Professor Yoshida to Peter Jamieson (PJ) to give a presentation (The Development of Wind Energy) at the 10th NCRS International Symposium. During the period around this symposium, in informal workshops hosted by professor Ohya, PJ also received presentations on wind turbine related work at Kyushu and presented work on ducted rotors and on multi rotor systems. The ducted rotor work was of direct relevance to Kyushu as professor Ohya's group had developed the Wind Lens ducted turbine and the multi rotor concept was also of interest because among other potential benefits it offered a means of upscaling net turbine capacity of the Wind Lens without some of the problems in constructing a single large ducted rotor. Thus a collaboration was established with the aims:

a) To exchange information regarding especially the experimental developments of the Wind Lens at Kuyshu related to analytical work on ducted rotors at Strathclyde
b) To jointly explore the multi rotor concept again involving interaction between small scale experiments at Kyushu with large scale system design and analysis work at Strathclyde associated with Innwind.EU, a European collaborative project.

Method

Following the initial meeting (November -December 2013) at the 10th NCRS International Symposium, Uli Göltenbott, a student at Kyushu with Prof. Ohya commenced a PhD study relating to Wind Lens in the context of multi rotor systems. Some experiments were completed within a few months of the initial contact in December 2013. Later in June 2014, Professor Ohya and Dr Nagai visited Strathclyde University (June13th 2014) when further presentations were exchanged and an agreement to collaborate was consolidated. Prof. Ohya had obtained funding to support a further visit to Kyushu by PJ and Scott McLaren-Gow, a PhD student at Strathclyde University working on ducted rotor design and this visit took place from 20th to 24th October 2014. Following this meeting specific information on the Wind Lens configuration was provided to Strathclyde University and on multi rotor systems to Kyushu. This was analysed and results of 2015 presented at RIAM in a further visit of P Jamieson.

Results and discussion

The findings of the University of Strathclyde are primarily reported here. It is expected that the related work at Kyushu RIAM will be further detailed in other reports. Work on multi-rotor systems within the Innwind project completed in September 2015 and a report has been produced although the final version is still to be uploaded on to the Innwind web site. In general the results of the Innwind project showed great promise for the multi rotor system (MRS) concept. Some specific highlights that connect to the experimental work of Uli Göltenbott include a detailed study of the aerodynamic interaction of closely spaced rotors both for a 7 rotor array and for the 45 rotor array design to produce a 20 MW system. CFD by the University of Athens (within the Innwind EU project in which PJ led a study of the multi rotor concept) has shown small power gains ~ 3% for a 7 rotor array (6 six rotor symmetrically disposed around a central rotor all at 5% diameter minimum distance apart). By power gain is meant more power from the 7 rotor array than 7 x power of a single rotor operating in isolation. Similar CFD analysis of a 45 rotor array showed an augmented power gain of ~ 8% (at 5% and 2.5% diameter minimum rotor spacings). Supplementary analyses showed that for bare rotors without ducts such power gains were substantially realised at closest possible spacings and that flow in the spaces between the rotors was important to achieve the power augmentation. These results were available in 2014 but further consolidated in 2015. In addition new work in the areas of structure and yaw system design (and also yaw control) indicated cost effective solutions even at very large scale showing that the MRS is an effective way to upscale wind turbine systems with many advantages compared to simply making larger single rotors. Strathclyde anticipate new student projects related to MRS and collaboration on data analysis and design development as data becomes available from the latest operational Wind Lens models. Although the design and cost of energy evaluation of the MRS concept within Innwind is complete, work continues on yaw system control both for the MRS on a fixed foundation and on a floating platform. Within the Innwind project the 20 MW MRS is evaluated to be advantageous in respect of O&M primarily because with smaller turbine components there is no need to involve very large jack-up vessels in maintenance. However the details of design for maintenance and operational logistics are going to be very important in order to preserve advantage in O&M for this concept.

The PhD of Scott McLaren-Gow at Strathclyde University in the Centre for Doctoral Training in Wind Energy will be concluded in 2016. It has a focus on getting a much deeper understanding of fundamentals of ducted rotor systems primarily based on inviscid flow modelling using well established panel methods in this case based on a vortex ring representation of the wake. This work is supervised jointly by PJ and Prof. Graham from Imperial College, London who is a world class expert with extensive experience in analysis and numerical modelling of fluids. There appear to be two classes of ducts; those which, loosely speaking, create smoothest flow conditions and may tend to maximise rotor loading at Ct =8/9 and those which induce the largest through flow and highest performance coefficient. Curiously although the detailed mechanisms must be quite different, considering the strong vortex shedding in the CFD modelling at RIAM, the inviscid analyses suggests a broadly similar shape to Wind Lens as optimum. This was s confirmed by more extensive analyses in 2015

Acknowledgement

This work was supported in part by the Collaborative Research Program of Research Institute for Applied Mechanics, Kyushu University.